MASTER THESIS

Modeling of a multi-PMT optical sensor for IceCube-Gen2 in GEANT4 and Monte Carlo studies to optimize its sensitivity

A thesis submitted in fulfilment of the requirements for the degree of

Master of Science *at* Westfälische Wilhelms-Universität Münster

and

Máster Interuniversitario en Física Nuclear *at* Universidad de Sevilla

by

Daniel Suárez García

Supervisors

Prof. Dr. Alexander Kappes

Prof. Dr. Carlos Guerrero Sánchez

"Y pa' enamorarla
Se necesita
Más de una cita
Y pa' enamorarla
Se necesita, ey
Más de una cita, ey."

– Bad Bunny, April 2020

"The man who insists upon seeing with perfect clearness before he decides, never decides."

– Henry F. Amiel

Contents

1 Introduction and motivation 1

2 Neutrinos 3

2.1 Standard Model . . . 3
2.2 Cosmic rays and neutrino generation . . . 5
2.3 Neutrino detection . . . 8

3 The IceCube neutrino observatory 11

3.1 From IceCube to IceCube-Gen2 . . . 14
3.2 The multi-photomultiplier digital optical module . . . 17
3.3 Photomultiplier tube . . . 18
3.4 LOM: An optical module for IceCube-Gen2 . . . 19
3.4.1 Model with reflectors . . . 21
3.4.2 Gel pads model . . . 22

4 LOM geometry and simulations with Geant4 25

4.1 General geometry . . . 25
4.2 Reflective components modeling . . . 28
4.2.1 Conical reflectors . . . 28
4.2.2 Ellipsoidal reflectors . . . 29
4.3 LOM with holding structure and reflectors . . . 29
4.4 LOM with gel pads . . . 30
4.5 Physics and primary particles . . . 33
4.6 Simulation tools . . . 34

5 Reflective components for single PMT 37

5.1 Setup of the simulations . . . 37
5.2 Conical reflective structures for a single PMT . . . 38
5.3 Ellipsoidal reflective structures for a single PMT . . . 40

6 Optimization of the reflective components 43

6.1 Setup of the simulations 43

6.2 mDOM cross-check 44

6.3 Conical reflective structures 45

6.4 Ellipsoidal reflective structures 53

7 Summary and outlook 65

Appendix A Distribution of the PMTs 69

Appendix B Extra plots 71

List of Figures 74

List of Tables 79

References 80

Acknowledgements 86

1 Introduction and motivation

Since the beginning of time, humankind has been enthusiastic for knowing how the universe works. Understanding the interaction mechanisms of the matter and the laws which govern its movement have been one of the greatest dreams of the human being. Although the curiosity of people covers several areas of knowledge, astronomy has always spearheaded this constant pursuit. The deep space and all its elements have inspired thousands of questions many of which are still unanswered.

Hundreds of people have devoted their lives to try to shed some light on the space mysteries over several hundred years. From Descartes and Newton attempting to understand the movement of the planets to Einstein and the discovery of the gravitational waves.

Along this path, in 1956 the neutrino was detected for the first times. Decades later this particle has proven to be extremely useful for astrophysics, being an ideal messenger of information about what is going on in areas of the universe inaccessible via other particles.

The neutrino interaction cross-section is very low and this makes that they can travel vast distances through space without deviating and interacting with anything. This also makes its detection an incredible challenge. Nevertheless, many detectors have been built around the world using different mechanisms to tackle this problem.

Among them, The IceCube Neutrino Observatory is the largest detector in the world and it is placed at the South Pole. IceCube consists of several strings under the ice with digital optical modules (DOM) deployed along them. The purpose of these modules is to detect the Cherenkov radiation emitted by charged particles which are products of the interaction between neutrinos and ice.

Two extensions of the detector are planned for the following years. First, the IceCube Upgrade will implement seven new strings close to the center of the IceCube and it aims to detect low energy neutrinos which allow to study neutrino oscillations among others. Also, it has the goal of understanding better the sensor performance and ice optical properties.

The another project to extend the current detector is IceCube-Gen2. I will contain 120 new strings which aim to increase the energy range and the statistics of the events.

In this context, a new digital optical module so-called mDOM was developed to try to improve the features existing IceCube module. This module will be used (400 out of 700 modules) for the IceCube Upgrade but for economic reasons, it will not be implemented in the IceCube-Gen2. Regard this problem, the Long Optical Module (LOM) is being developed and this module is currently chosen as the baseline model for IceCube-Gen2. The LOM intends to follow the segmentation idea of the multi-PMT optical module designed for mDOM but reducing its diameter and thus its deployment cost. The final design for the LOM has still not been decided and this work aims to test these designs using simulations in order to characterize their detection capabilities.

2 Neutrinos

In 1899, after the discovery of radioactivity[1], Ernest Rutherford separated radioactive emissions into two types based on its capacity to penetrate on the matter: alpha (α) and beta (β).

It was not until 1914 that James Chadwick using a Geiger counter, measured the beta emission spectrum. This spectrum opened many questions for scientists around the world [1]. If only one electron is emitted in a beta decay, that electron must have its energy well defined, and its energy plus the recoil energy of the atom should be equal to the initial energy, in order to fulfill the law of energy conservation. This means that if the beta decay is a two particles process, such as the alpha decay, its spectrum should be a very well defined energy line. However, Chadwick got a continuous spectrum, which showed that the emitted electron lost energy during the decay.

In 1930, Wolfgang Pauli sent a letter to the Physical Institute of the the ETH Zürich to try to resolve this problem [2]. In this letter, he suggested that besides electron, another particle was emitted during beta decay but this particle was very difficult to detect. He called it “neutron”.

One year later, Enric Fermi renamed the Pauli’s neutron to “neutrino” and in 1933, published his theory for decay beta. He applied the theory of quantum mechanics to matter particles, supposing that they can be created and annihilated. In this way, neutrinos (and electrons) are created in the beta-decay process, rather than contained in the nucleus[2] [3].

Neutrinos were finally detected by Clyde Cowan and Frederick Reines in 1956 [4]. The properties associated with these particles resulted be very close to what Pauli and Fermi predicted a few years earlier.

Throughout this chapter, the neutrinos and their main features are presented in the context of the Standard Model. Also, the neutrinos sources are discussed along with the fundamentals to detecting them.

2.1 Standard Model

From atoms to the heaviest stars of the universe, all known matter is composed of elementary particles. These are described by the Standard Model of physics, and are depicted in Figure 2.1.

These elementary particles can be divided into some groups. First, there are six

---

[1] Radioactivity was discovered by Henri Becquerel in 1896.

[2] Although alpha decay was already known, in this case, alpha particle already existed inside the nucleus. Thereby, the fact that electrons and neutrinos were created during the process, was a very novel idea.

quarks (purple particles in Figure 2.1) which join to form hadrons, such as protons and neutrons. Next, there is the lepton family, marked with green, formed by electron, muon, tau and their respective neutrinos. These neutrinos can have three different flavors, one for each of their lepton counterpart: Electron neutrino ν_e, Muon neutrino ν_μ and Tau neutrino ν_τ. For each quark and lepton, there is also its corresponding antiparticle, which has identical mass but its electrical charge is opposite (antiparticles do not appear in the figure).

Besides these, there are gauge bosons, marked with orange in Figure 2.1. These particles describe the four fundamental interactions: the photon is associated with electromagnetic interaction, gluons for the strong interaction, and Z and W bosons correspond to the weak force (orange particles). Finally, the Higgs boson, marked with yellow, relates to the mass of the rest of the elementary particles via the Higgs mechanism.

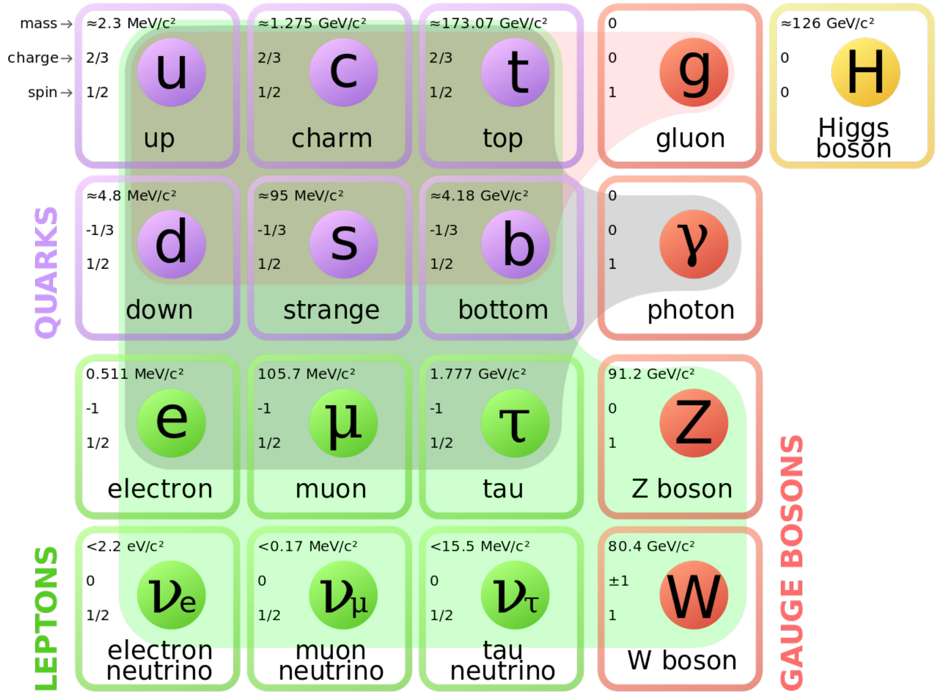

Figure 2.1. Elementary particles of the Standard Model. Colored backgrounds provide information about which particles can be affected by each interaction. Green shade relates the week interactions (from Z boson and W boson), purple shade relates to the electromagnetic interaction (from photon) and the red shade relates to the string interaction. Taken from [5]

Quarks and leptons are joined with Z and W bosons because all of them are subject to the weak interaction. In the same way, all charged particles are associated with photons, that is to say, with electromagnetic interaction. And finally, strong force only affects quarks [6].

2.2 Cosmic rays and neutrino generation

While you read this line, millions and millions of neutrinos are passing through you without interacting with your body or leaving any trace behind. They are particles with no electrical charge and are part of the lepton family, so they also do not “feel” the strong interaction. But you may wonder, where are all those neutrinos coming from? Neutrinos originate from a wide sources and many are not clear yet. An overview of some sources is shown in Figure 2.2.

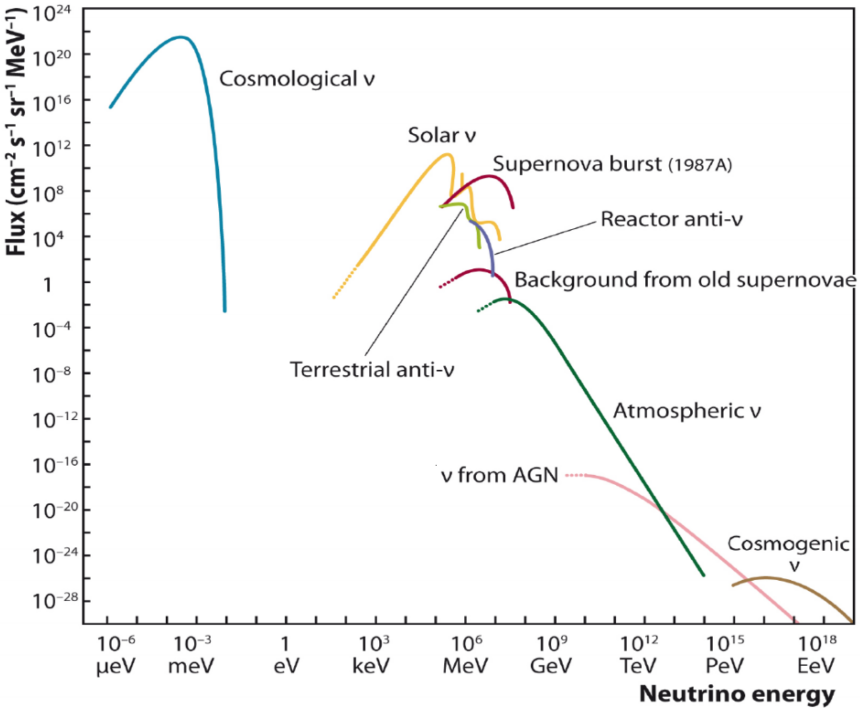

Figure 2.2. Neutrino fluxes for different sources like the cosmological background radiation, the sun, supernovae and the Earth atmosphere. Taken from [7].

The interest of this thesis lies in the high energy neutrinos and to produce these particles, in most cases, the so-called cosmic rays are necessary. In this section, these rays, their origin, and the different mechanisms to generate high energy neutrinos are discussed.

Approximately 1000 cosmic rays particles hit the Earth per square meter and per second. They are mainly ionized nuclei and its composition is known in great detail [8].

- 90 % → Protons
- 9 % → Alpha particles
- 1 % → Heavier nuclei such as Iron, Nickle, etc [9]

What distinguishes the cosmic rays from the rest of the background radiation is their high energies, which can reach over 10^{20} eV [8]. This means they are relativistic

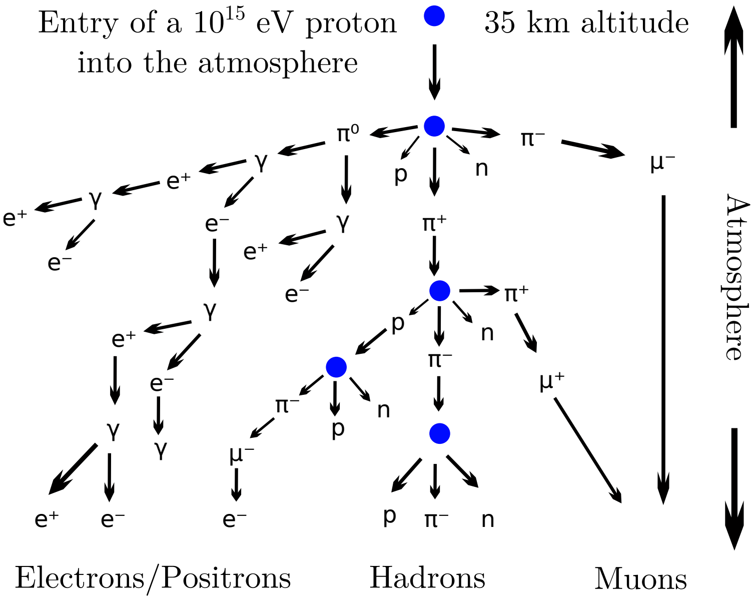

Figure 2.3. Air shower produced when cosmic rays enter the Earth atmosphere. Taken from [12].

particles, as their energies are greater than their masses. However, although their composition is known, their origin and the nature of their extremely high energies are not clear yet.

There are two different scenarios to explain the particle acceleration. First, the top-down models, where it is assumed that the cosmic rays are products of decay of a heavier nucleus corresponding to the early universe. This idea was strongly rejected by the first generation of neutrino telescopes [10] and results obtained from large area surface arrays [11].

Secondly, the bottom-up scenario states that the cosmic rays are accelerated by different objects in the universe (active galaxy nuclei, supernova remnants, pulsars, etc.) gaining the levels of the observed high energies. This concept is currently the best accepted idea but has still been unproven.

Different ways to produce high energy neutrinos from the cosmic rays are presented below.

As previously stated, cosmic rays are in 90 % protons. When these protons interact with the photons of the cosmic microwaves background, several exotic particles can be produced. Among these particles, there are Δ^+ and this resonances decays into nucleons and pions which later decay into neutrinos and gamma photons [13].

- $\Delta^+ \rightarrow p + \pi^0 \quad \longrightarrow \quad \pi^0 \rightarrow \gamma + \gamma$
- $\Delta^+ \rightarrow n + \pi^+ \quad \longrightarrow \quad \pi^+ \rightarrow \mu^+ + \nu_\mu \quad \longrightarrow \quad \mu^+ \rightarrow e^+ + \nu_e + \bar{\nu}_\mu$

If this interaction takes place when protons are far away from their source, the so-called GZK neutrinos are produced[3] and they have energies from 10^{16} eV to 10^{18} eV [15]. These are called "cosmogenic ν " and the neutrino spectrum is depicted in Figure 2.2.

Besides the cosmic rays that interact with the microwaves cosmic background, some others reach the Earth atmosphere. When an air molecule is hit by a cosmic ray particle, the so-called air showers are produced. These are successive interactions in the upper atmosphere and where a huge number of particles are generated as a result of strong, electromagnetic, and weak interactions.

During these showers, neutrinos are formed in the decays of unstable intermediate particles[4]. These neutrinos are called atmospheric neutrinos. Figure 2.3 depicts a sketch of this process.

Another mechanism for the production of high energy neutrinos is by means of massive and powerful objects in the universe, such as active galactic nuclei (AGN). AGNs are super-massive black holes in the center of a galaxy. Black holes have the capacity of attracting all matter residing nearby due to their huge gravity and this generates an accretion disc around the black hole and a dust torus. Perpendicular to the disc, two relativistic particles jets are emitted by the two poles and here, the particles are accelerated. Neutrinos are formed as results of different reaction inside these jets [16]. A sketch of this process is shown in Figure 2.4.

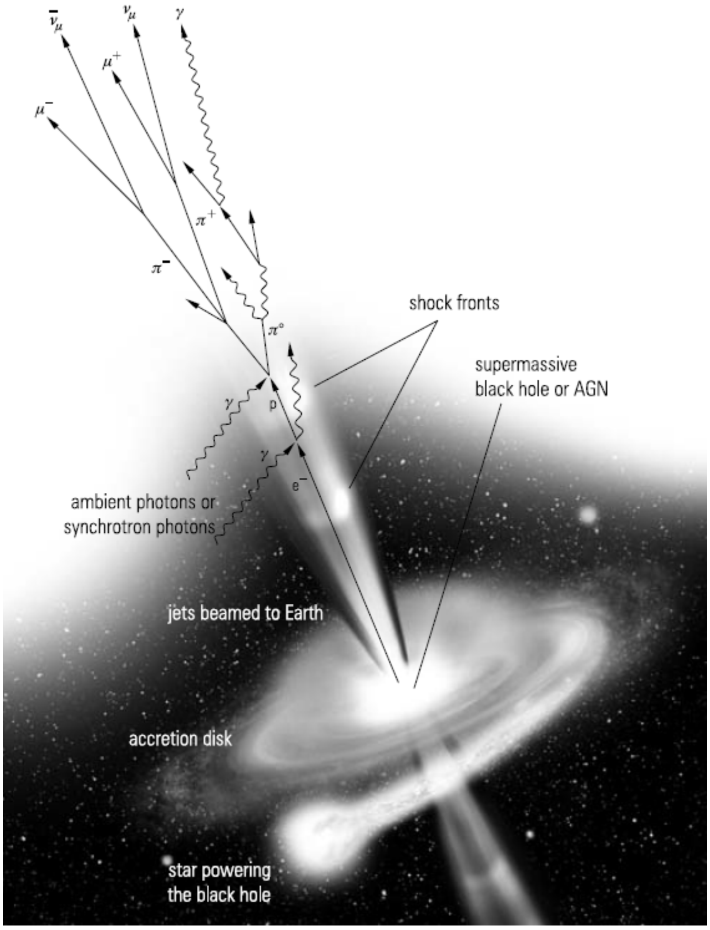

Figure 2.4. A sketch of an active galactic nuclei (AGN) accelerating particles and producing high energy neutrinos. Taken from [16].

The mechanism to accel-

---

[3] The name GZK come from K. Greisen, G. T. Zatsepin, and V. A. Kuzmin. They were who first predicted the phenomena [14].

[4] The main reaction which produces neutrinos are the pion decays (and to a lesser extent, decay of kaons).

erate the particles is the so-called first order Fermi acceleration [17]. This mechanism is based on the transfer of kinetic energy from a shock wave to the charged particles. If a charged particle encounters a shock wavefront, it is reflected without loss of energy due to magnetic field inhomogeneities in areas close to the wavefront. Also, the wavefront act as a magnetic mirror, and thus the charged particles can pass through this process several times, gaining more and more energy[5]. This idea can be extended to other celestial bodies as pulsars, Supernova remnants, micro-quasars, etc [18].

Currently, there are no evidences to confirm that protons are accelerated in these celestial bodies by Fermi acceleration. In order to figure out how these acceleration mechanisms work and know the sources of cosmic rays, high energy neutrinos produced in these phenomena are very useful. Hence the importance of neutrino observatories, whose detection mechanisms are going to be topic of the next section Section 2.3.

2.3 Neutrino detection

Neutrinos are quasi-massless [6], do not possess electrical charge and being leptons, they do not undergo strong interactions, hence they only interact via the weak interaction. This means that these particles interact very weakly with matter, and can travel almost freely throughout the universe. This is a great advantage since they can provide much information about phenomena produced light-years away from the Earth. However, it also makes their detection a big challenge.

It is not possible to detect neutrinos directly, so the charged particles which they produce during their interactions with the matter should be detected. At high energies (> 10 GeV), the interactions are dominated by the deep inelastic scattering at nucleons in matter or at their quarks [19]. In this context, the neutrinos can interact by means of the charged current (CC) when it exchanges a W^+ or W^- boson or in the neutral current (NC) when it exchanges a Z^0 boson [19]. These are described by

$$\nu_l + N \xrightarrow{\mathrm{W}^\pm} \nu_l + X \quad (NC), \qquad\qquad l + N \xrightarrow{\mathrm{Z}^0}, \nu_l + X \quad (NC) \tag{2.1}$$

where ν_l is a neutrino with the lepton flavor l, N is a nucleon, l is the lepton and X is the additional products of the interaction.

Depending on the neutrino energy range, there are several methods to detect them

---

[5] It is named first order Fermi acceleration because the relative transferred energy is directly proportional to the shock wave speed (relative to the light speed),

$$\frac{\Delta E}{E} \propto \frac{v}{c}.$$

[6] The neutrino mass is not exactly known, they are so light that the gravitational force can be neglected in their interactions.

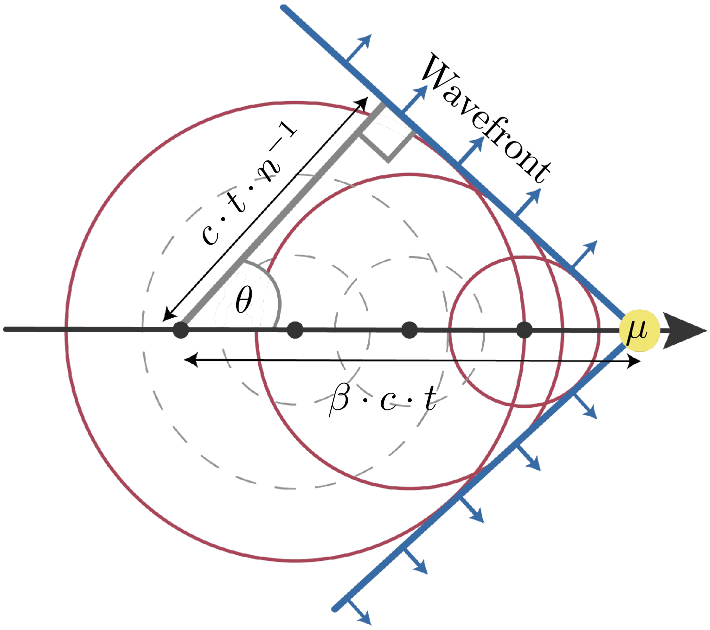

Figure 2.5. Sketch of Cherenkov radiation. In this picture, the charged particle is a muon. β is the speed of the particle relative to the vacuum speed of light, n is the refractive index of the medium, t is the time and c is the vacuum speed of light. Taken from [6].

such as radio-chemical methods, tracking calorimeters, radio detectors, etc. One of the most known mechanism for their detection is based on Cherenkov radiation and many detectors around the world were built with this principle.

BDUNT[7] [20] and ANTARES[8] [21] are both neutrino detectors which use water as material medium to carry out the detections. ANTARES for example is situated in the Mediterranean sea and it consists of 12 strings anchored about 2500 meters under water. BDUNT has a similar configuration and it is located in Lake Baikal, in Russia.

Another important detectors are IceCube [22] and KM3NeT [23]. Based on the knowledge provided by ANTARES, KM3NeT is a new detector that is currently in construction phase. It will use water like material medium and it will be in the Mediterranean sea too. The IceCube detector is going to be discussed in detail more ahead in Chapter 3.

When a charged particle travel through a dielectric medium, this particle polarizes the nearby atoms. This means electrons of the medium are excited and later, they de-excite losing energy in form of radiation. If the velocity of the particle is lower than the velocity of the light in this medium, this radiation interferes destructively. However, if the velocity of the particle is higher than the velocity of the light in this medium, the radiation interferes constructively. In this case, a wavefront of photons is produced [24].

This radiation is emitted in a conical shape and the cone opening angle can be obtained looking Figure 2.5. It only depends on the velocity of the charged particle

---

[7] Its name comes from Baikal Deep Underwater Neutrino Telescope.

[8] Called ANTARES by Astronomy with a Neutrino Telescope and Abyss environmental RESearch project.

and the refractive index of the dielectric medium,

$$\cos(\theta) = \frac{\cancel{c} \cdot \cancel{t} \cdot n^{-1}}{\beta \cdot \cancel{c} \cdot \cancel{t}} = \frac{1}{\beta \cdot n}, \tag{2.2}$$

where β is the speed of the particle relative to the vacuum speed of light, n is the refractive index of the medium, t is the time and c is the vacuum speed of light [24].

Also, the kinetic energy of the charged particle is known

$$E_{\text{kin}} = m_0 c^2 \left(\frac{1}{\sqrt{1-\beta^2}} - 1 \right), \tag{2.3}$$

where m_0 is its rest mass. Hereby, using the conditions required for producing Cherenkov radiation (which may be expressed as $\beta > n^{-1}$), the minimum kinetic energy which should have the charged particle can be obtained as

$$E_{\text{thr}} = m_0 c^2 \left(\frac{1}{\sqrt{1-n^{-2}}} - 1 \right). \tag{2.4}$$

Detecting this Cherenkov radiation produced, it is possible to get information about the primary neutrino and it is the mechanism used by the IceCube neutrino observatory. Since this thesis focus on the next generations of the IceCube detector, this will be described in the next chapter.

3 The IceCube neutrino observatory

Cherenkov-based neutrino detectors need certain conditions to be able to efficiently detect neutrinos:

- A huge transparent medium to balance the low interaction probability of neutrinos and to allow photons to propagate through it
- A shield or veto region to filter out all other non desired particles.

One of the most abundant medium that fulfills these requirements is ice and and it is what IceCube Neutrino Observatory uses [22].

IceCube Neutrino Observatory is a neutrino detector located in the South Pole. It has 1 km^3 detector volume and consists of 86 strings located below the ice surface and distributed along these string, there are 5160 Digital Optical Modules (DOMs). The main goal of IceCube is to detect high energy neutrinos and thus, to discover their sources and identify them scanning the sky. In fact, one of the most important results obtained with IceCube is the neutrino emission from the direction of the blazar TXS 0506+056 [25]. However, it was not built exclusively for this goal, but it has the capability of detecting neutrinos from a wide energy range which allows researches and possible discoveries relate to the neutrino physics [22].

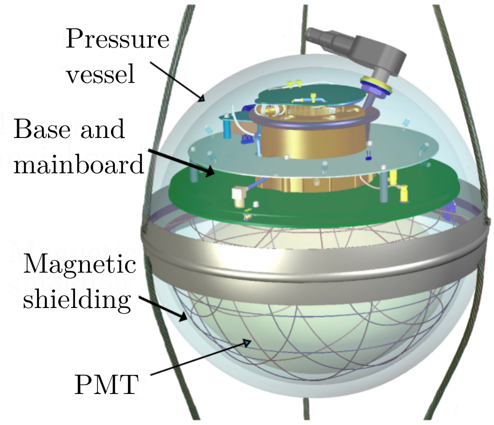

Figure 3.1. Digital optical module implemented currently in IceCube. Figure courtesy of the IceCube Collaboration.

The main array of the detector is formed by 78 strings which are almost 2500 meters long. Each string has 60 digital optical modules separated by 17 meters, starting at 1450 to 2500 meters depth. Also, the horizontal distance between the strings is 125 meters. This configuration allows to study neutrinos with an energy range between 100 GeV and $\mathcal{O}$(PeV). The digital optical modules (DOM) implemented have a 10-inch diameter photomultiplier (PMT) facing down along and some electronics elements inside of a pressure vessel. A representation of the DOM is illustrated in Figure 3.1.

Besides these strings, IceCube has 8 more strings situated at the center of the detector volume. Along theses strings, the inter-module spacing is only 7 meters and

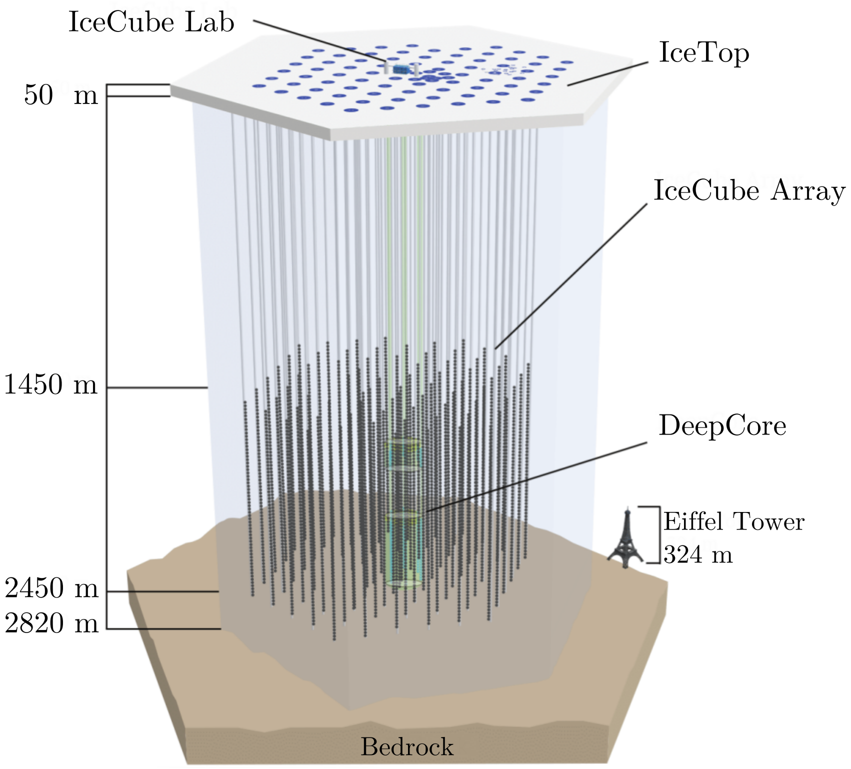

Figure 3.2. Sketch of IceCube Neutrino Observatory. Figure courtesy of the IceCube Collaboration.

they are deployed between 2100 and 2450 meters deep. In the region between 2000 and 2100 meters deep, significant scattering and absorption of light occurs therefore no DOMs were implemented in this region. Instead, above this layer were implemented the remaining 10 DOMs for each string, with a spacing of 10 meters [26].

The horizontal distance between the strings is 72 meters and, therefore, the system is prepared to detect neutrinos of energies in the order of tens of GeV. This form a more densely instrumented configuration inside of IceCube called *DeepCore*.

Finally, there is a further sub-experiment called IceTop which consists of 81 water tanks placed at the surface of the ice. These tanks are approximately over each the strings of IceCube and each one has 2 digital optical modules inside. The idea with this experiment is to detect high cosmic ray events and also, at the same time, work as a veto against the atmospheric neutrinos. This system can detect cosmic rays with an energy ranging from 100 TeV to 1 EeV [27].

A general sketch of the IceCube neutrino observatory with the different mentioned parts is shown in Figure 3.2.

All photomultipliers of IceCube are prepared to detect photons produced by Cherenkov radiation and from them, getting information about the neutrinos. For this, it is important to know that, depending on several factors, neutrinos of different flavors can produce different signatures in the detector.

If the neutrinos interact by means of the neutral current (exchanging boson Z°), the signatures are similar between them. However, if the neutrinos engage the charge current, it is easier distinguish them. The different signatures left by neutrinos interacting by the charged current are shown in Figure 3.3.

When a muon passes through the detector, it travels a very long distance (the order of km)[9]. This produces a long signature through the detector. This type of signal is called *Track* and it reflects the presence of a muon neutrino. With these events, it is possible to get a precise directional reconstruction with very good angular resolution. This is useful for the research of point sources since muons do not deviate much from the initial direction of the incident muon neutrino. However, the reconstruction of the energy of the neutrino is difficult to achieve with *Tracks* because the events generally start and finish out of the boundaries the detector. Also, the contamination of atmospheric neutrinos is larger for the muon neutrinos than the remaining of the flavors neutrinos which also makes more complicated its reconstruction in energy [28]. This signature is represented in Figure 3.3(a).

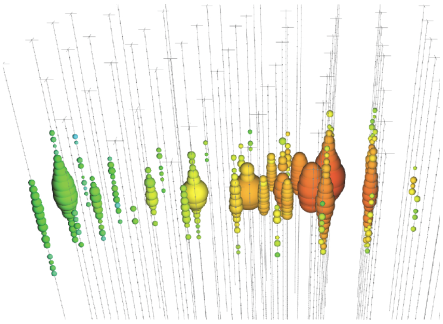

(a) Light deposition signature of a *Track*.

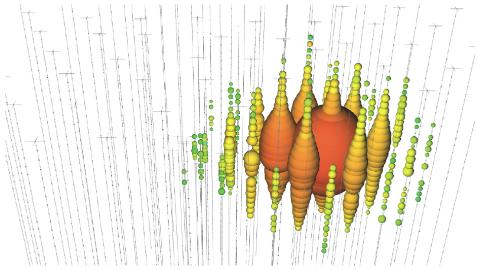

(b) Light deposition signature of a *Shower*.

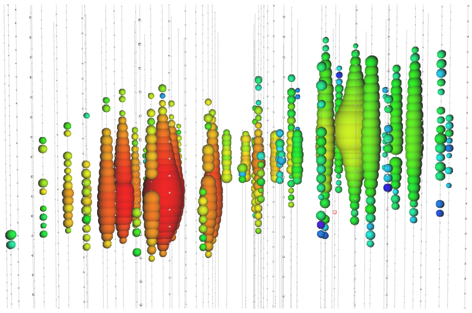

(c) Light deposition signature of a *Double Bang* event.

Figure 3.3. Signatures left at the detector by the different flavor neutrinos when they interacts by means of the charged current. Digital optical modules are represented as black dots along the strings. . The dot size represents the amount of light that has been detected and the color gives us information about the arrival time of photons to this DOM, going from red (early) to blue (later).

Another type of signal that can appear are the so-called *Showers* and a sketch of it is shown in Figure 3.3(b). In this case, a large number of photons are emitted in a relatively small volume, and this leaves a spherical mark in the detector. The

---

[9] This is true in general but it depends on its energy so it is not always the case.

reconstruction of the angular direction of the particle is very poor because all the energy has been deposited in this small volume. However, this also means that the energy of the particle can be obtained without much difficulty and with quite good accuracy. Two different processes can produce a *shower*:

- **Electromagnetic case:** Electrons or positrons deposit all its energy quickly due to its large interaction cross-section. This particle travels very short distances as a result of scattering in the medium, Bremsstrahlung, and pair production.

- **Hadronic cascade:** Also, all neutrinos flavours are able to produce a hadronic cascade, which can give rise to *shower* signatures in the detector.

Tau neutrinos can also leave a characteristic signal in the detector. The incoming tau neutrino produces a tauon in the detector volume and this tauon after a short distance traveling, can decay in two possible ways. Either it decays into a muon or electron (or positron), or it decays into various combinations of neutral and charged pions[10]. The signal of these processes is called *Double Bang* because it looks like two *showers* spatially separated as result of the two decays produced. This is depicted in Figure 3.3(c).

Actually, it is not easy to distinguish a *Shower* signature and a *Double Bang* signature because the neutrino should have a very high energy to leave a signature where one can observe well both "*Showers*" so usually, these signatures are confused with one another. Also, if the neutrinos engage the charged current, all flavors can leave a *Shower* signature hence it is not easy to distinguish the different flavors.

3.1 From IceCube to IceCube-Gen2

The devices deployed currently in the IceCube have already been presented. Besides these, two extensions so-called IceCube Upgrade and IceCube-Gen2 are being developed.

On the one hand, IceCube Upgrade will start its construction in summer 2022/2023, but may be delayed due to the Corona pandemic. It consists of 7 new strings situated at the center of the current arrays. With this upgrade, a better performance of IceCube at low energy will be achieved, as a result of the closer proximity of modules. The horizontal distance is 20 meters and the inter module distance along one string is 2.4 meters [29]. These distances are smaller even than DeepCore and the distribution of the strings is shown in Figure 3.5.

---

[10] Muon/electron/positron are emitted accompanied by its corresponding neutrinos and antineutrinos, and neutral and the charged pions together with a tau neutrino.

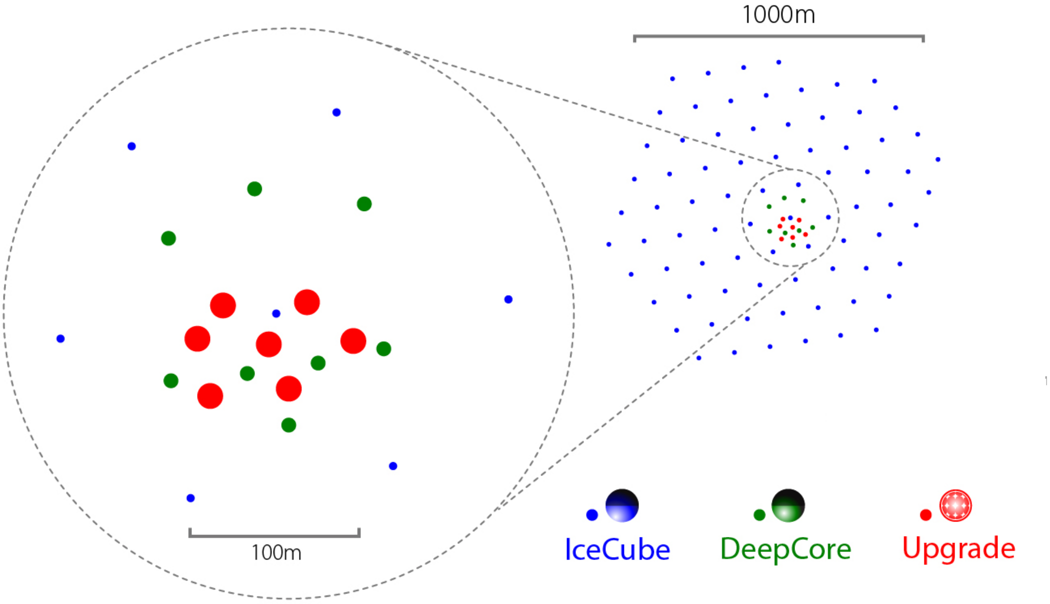

Figure 3.5. Sketch of the IceCube Upgrade viewed from above. Courtesy of the IceCube Collaboration. Modified.

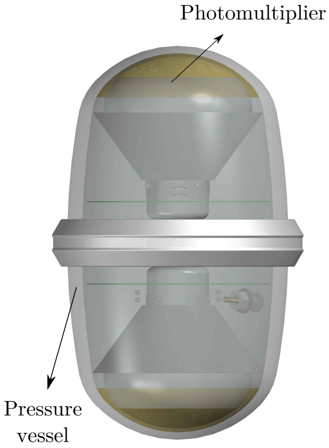

Figure 3.4. Dual optical sensor in an Ellipsoid Glass for Gen2 (D-Egg). A digital optical module designed for IceCube Upgrade. Courtesy of the IceCube Collaboration.

Also, IceCube Upgrade will deploy new digital optical modules. These new modules will be more sophisticated and will have some advantages over their predecessor. There are two main ideas that are being studied in terms of the design of the new DOMs. First, the segmentation of the effective area of the modules using several PMTs instead of only one. This allow to improve the reconstruction of the angular direction of the particle. And the second idea is the use of wavelength shift and light-guiding techniques to increase sensitivity to UV photons[11].

According to these main goals, several designs have been developed and two of the most important ones are: *Dual optical sensors in an Ellipsoid Glass for Gen2 (D-Egg)* [30] and *Multi-photomultiplier Digital optical Module (mDOM)* [31].

The idea of mDOM is to implemented more PMTs to increase the effective area. This will be explained in detail in Section 3.2.

The D-Egg consists of two eight-inch photomultipliers oriented back-to-back along

---

[11] UV sensitivity is not important in cases of the water neutrino telescopes because water acts as a threshold in this range of energy. However, ice does not behave the same way and for this, it would be good having a DOM with UV sensitivity.

the vertical axis. The main goal of this design is to get an increase in the sensitive area for each module. The thickness of the glass pressure vessel helps to optimize the sensitive area in such a way as the thickness is shorter in the photocathode zone and it reaches its larger value in the equatorial zone [32]. In Figure 3.4 there is a sketch of the D-Egg.

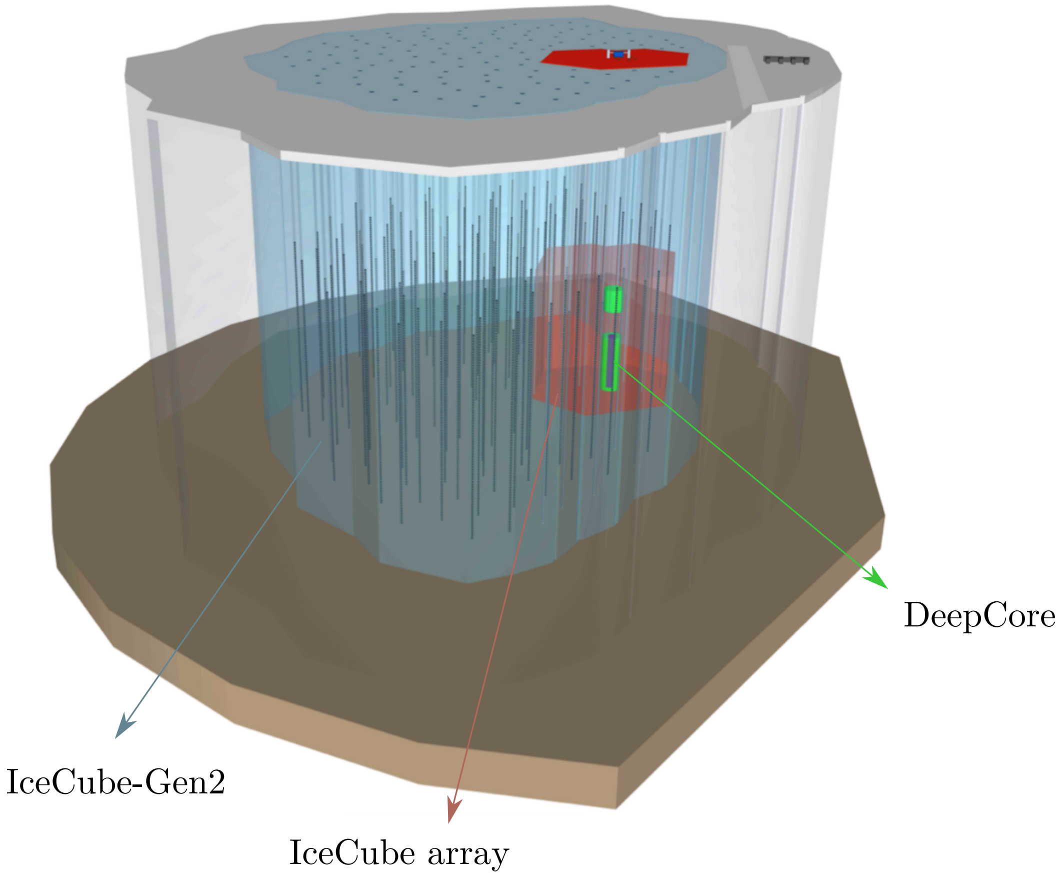

Figure 3.6. Sketch of IceCube-Gen2. Green color corresponds to the DeepCore[12], red color represents the IceCube array, it means, the current configuration deployed at the South pole, and blue color show the extension of the future IceCube-Gen2 and its strings. Figure courtesy of the IceCube Collaboration.

On the other hand, IceCube-Gen2 will allow an increase of the detection rate of the high energy neutrinos, rising the detector volume by a factor of up to ten. This is shown in Figure 3.6. It consists of 120 new strings which will have 125 new digital optical modules each one. Nowadays, more information about the optical properties of the glacial ices is known in comparison with when the current IceCube was built [33]. The absorption length of the Cherenkov photons in the ice is larger than initially

---

[12] This sketch shows DeepCore are divided in "two parts", avoiding the region where scattering and absorption appear. It was commented in the page 12.

expected[13], and for this reason, the horizontal distance between the new strings will be larger too. It is considered a distance of approximately 240 meters. As a result of increasing the space between them, the minimum energy that neutrinos should have to be detected is also increased up to 50 TeV [33].

3.2 The Multi-photomultiplier Digital Optical Module

The design of mDOM is based on the optical module of KM3NeT and its innovative arrangement of the elements. They were pioneers by introducing the “multi-PMT” concept in the form of a integrated module comprising 31 three-inch PMT inside a one pressure vessel [23, 34].

This “multi-PMT” idea presents several advantages which deserve to be studied. In the first place, the angular acceptance is better because a higher percentage of the surface is covered by photocathode.

Another important advantage is the intrinsic directional sensitivity, i.e it is possible getting information on the incoming photon position through the detections in the different PMTs of the module.

Taking these into account, the multi-photomultiplier digital optical module (mDOM) has also been designed with the same idea of “multi-PMT”. The mDOM is a new optical module formed by 24 3-inch PMT facing multiple directions. These PMTs are held in place by a holding structure 3D-printed which has several slots where they are fitted. In addition, there is a mainboard with electronic elements used to digitize the signal, and an active base at the end of each PMT for high voltage generation.

All this system is placed inside a pressure vessel of glass which protects the module against external conditions. Between the glass of this pressure vessel and the surface of the holding structure, there is a layer of gel. This aims to decrease the light reflections due to the difference in the refractive index between glass and gel. Also the gel also provides stability inside the module.

With the goal of increasing the effective area of the module, the mDOM has reflectors surrounding each photomultipliers. They are coated aluminium sheets in which photons are reflected. Figure 3.7 shows an sketch of this module and its size.

The area obtained summing ten 3-inch PMT corresponds approximately the photocathode area of only one 10-inch PMT. This means that if ten or more PMTs are included in the design, the total photocathode area of the module is increased. More PMTs covering the surface of the module means more percentile of area cover for photocathode, hence the angular acceptance is homogeneously covering the entire solid

---

[13] Today, it is known that the absorption length exceeds 100-200 meters.

angle. Furthermore, there is an improvement of the photon counting, since the detected photons are spread over several PMTs instead of one single multi-photoelectron waveform.

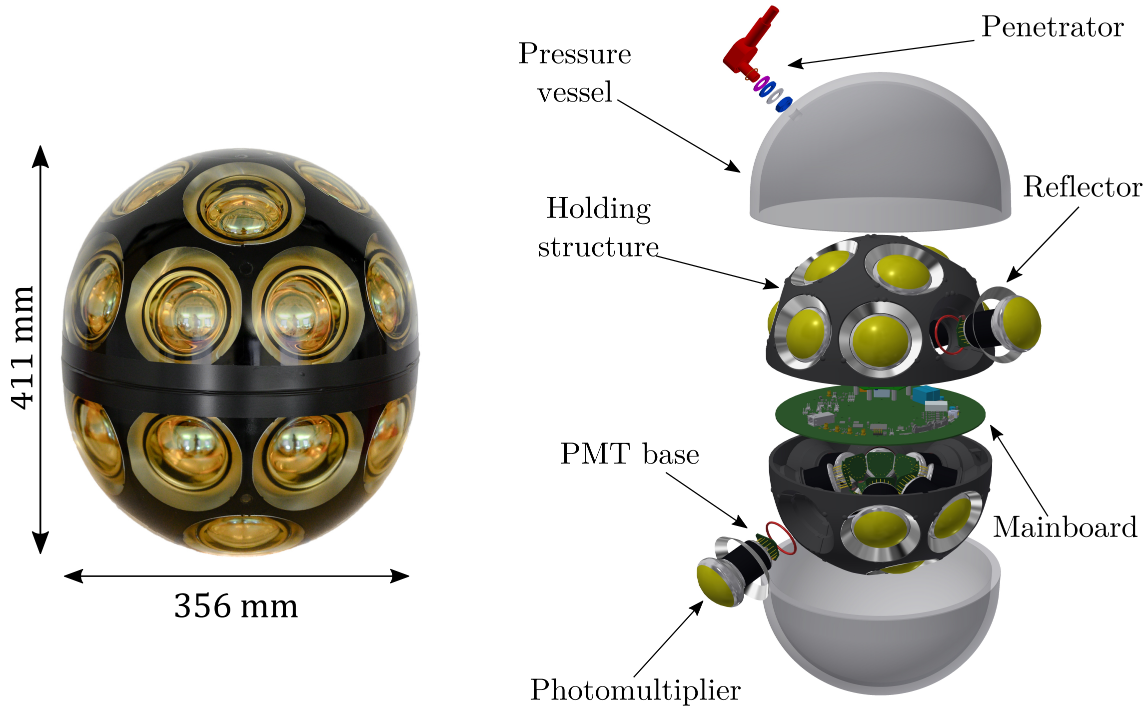

(a) Closed mDOM with its dimensions.

(b) Exploded view of the mDOM.

Figure 3.7. Sketch with the size, the design, and the components which form the Multi-photomultiplier Digital Optical Module (mDOM). Pictures courtesy of the IceCube Collaboration.

3.3 Photomultiplier tube

All types of digital optical modules contains one or several photomultiplier tubes. These are the main component of its functionality. A sketch of a photomultiplier tube is shown in Figure 3.8.

The photocathode is a thin layer of photosensitive material that when it receives a photon, this can be absorbed and an electron is emitted via the photoelectric effect. This photoelectron is accelerated by means of a potential difference and led toward a series of dynodes [35].

When the photoelectron reaches the dynodes, it releases several secondary electrons which are guided again toward the next dynode. Thus, electrons are multiplied by each step. This process is shown in Figure 3.8. Finally, electrons are led to the anode, where they are collected [35].

In order for this to work, a high voltage is applied between the photocathode, the dynodes, and the anode by a voltage divider. The voltage increases across the dynode system and electrons are led toward the next stage.

An important parameter of the photomultiplier tube is its quantum efficiency (QE). The quantum efficiency is the number of electrons emitted from the photocathode divided by the number of incident photons. In other words, it is a measurement of, how many photons are really detected compared to the incident photons. This parameter depends mainly on the wavelength of the incident photon and the material of the photocathode [35].

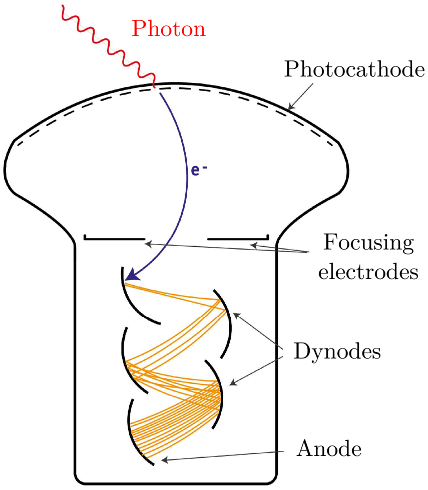

Figure 3.8. Sketch with main features of a photomultiplier tube. Taken from [6].

3.4 LOM: An optical module for IceCube-Gen2

Deploying strings in the deep ice is not an easy task. For constructing the current configuration of IceCube, a dedicated team was working from November to February each year from 2004 until 2011. The method to build this structure was melting an ice column with a diameter of 60 centimeters till 2540 m depth. The high-pressure hose and nozzle inject hot water that melts the ice at the speed of 2 meters per minute. Immediately, the water starts to freeze, therefore sensors should be deployed quickly inside the hole [36].

As depicted in previous chapters, IceCube-Gen2 will consist of 120 new strings, and and the drilling cost and time rises with the diameter of the hole it is very expensive. For this reason, the mDOM is being redesigned, reducing its diameter in order to drill smaller holes in a shorter time span. This new module is called the Long Optical Module (LOM) and its design is still open to modifications.

The main LOM design consists of 16 photomultiplier distributed in 4 rows. The position and orientation of the PMTs is different than the mDOM as well. In this case, the orientation of the PMTs is not aligned with the direction which joins its position with the center of the module and they are not perpendicular to the surfaces of the pressure vessel[14].

The design of the LOM is very similar to that of the mDOM. In fact, the goal of this design is to reduce the size without missing too much efficiency compared to

---

[14] With the mDOM, PMTs was aligned with direction to the center of the glass sphere and they were perpendicular to the surface of the pressure vessel.

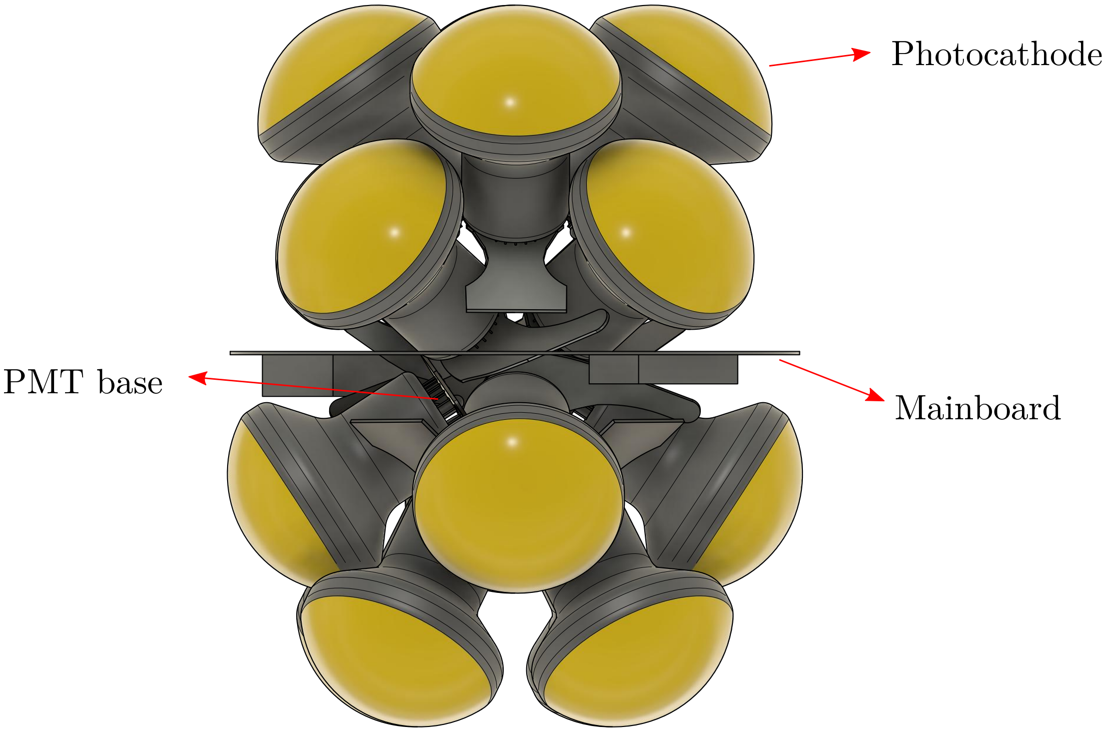

(a) Sketch of the position and orientation of the PMTs implemented in the LOM.

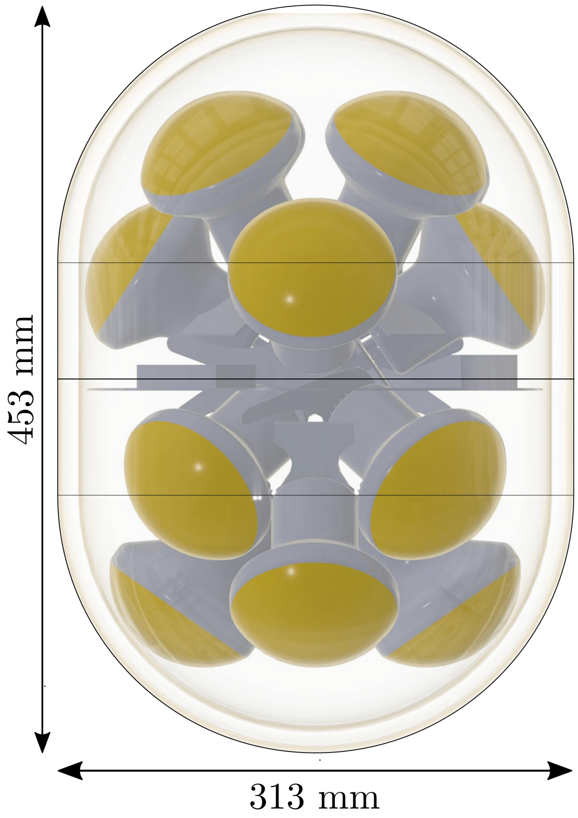

(b) LOM with the reflector surfaces and the glass covering all system.

Figure 3.9. Distribution of the elements of the digital optical module LOM. Pictures taken from a CAD model of the module courtesy of the IceCube Collaboration.

the mDOM. The main difference between both modules is in their size. Whereas the mDOM has 356 mm of diameter and 411 mm of the length (as shown in Figure 3.7(a)), the LOM has 313 mm of diameter and 453 mm of length. All PMTs are inside a glass pressure vessel. This distribution and the size of the LOM are presented in Figure 3.9.

Another important point in the design of the new module is the reflective components that surround the photocathode area. The characterization of these reflective components is an important topic of this thesis. There are two different models of the LOM depending of the design of these reflective components. They are presented in the next sections.

3.4.1 Model with reflectors

With this model, the LOM have implemented a holding structure, which is built through a 3D-printer, to hold in place the PMTs and the reflectors. Surrounding the holding structure there is a the pressure vessel of glass. Between the glass and the holding structure there is a thin layer of gel. the reflective structures with this model are metallic reflectors surrounding the photocathode.

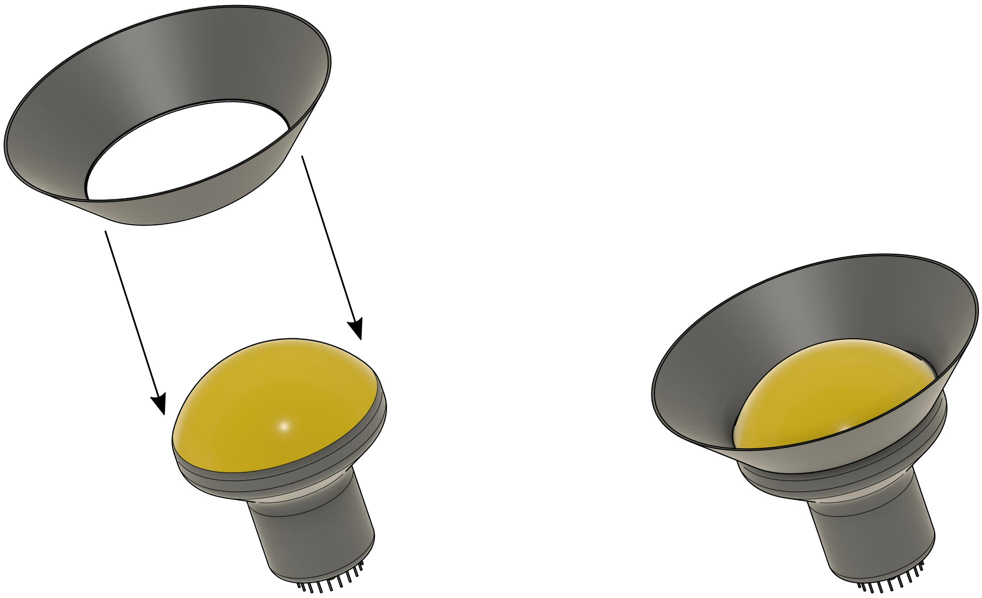

Figure 3.10. An example of reflectors surfaces implemented in the PMTs.

As in the case of the mDOM, the reflectors aim to increase the photocathode area of each PMT. Without the reflectors, if one photon is traveling forward the photocathode from a large angle with respect to the symmetry axis of the PMT, it would be missed because it would hit the holding structure and its material is absorbent. However, if there is a reflector surrounding the photocathode, photons that do not point to the photocathode are reflected forward it, raising the effective area. It can be understood as if the reflectors redistributes the sensibilities. In Figure 3.10, it is shown an example of such an element.

In the mDOM, these reflective components have a conical shape but in the case of the LOM, this has not been decided yet. The study of the different possible shapes and its impact in the module geometry and its performance is the most important topic of this thesis. Since the reflectors should increase the effective area, the best design of the reflectors for the LOM module will be the one that has higher efficiency and it can detect a major number of photons. In this way, the average sensitivity for photons from all directions will be optimized in order to choose the best reflector shape.

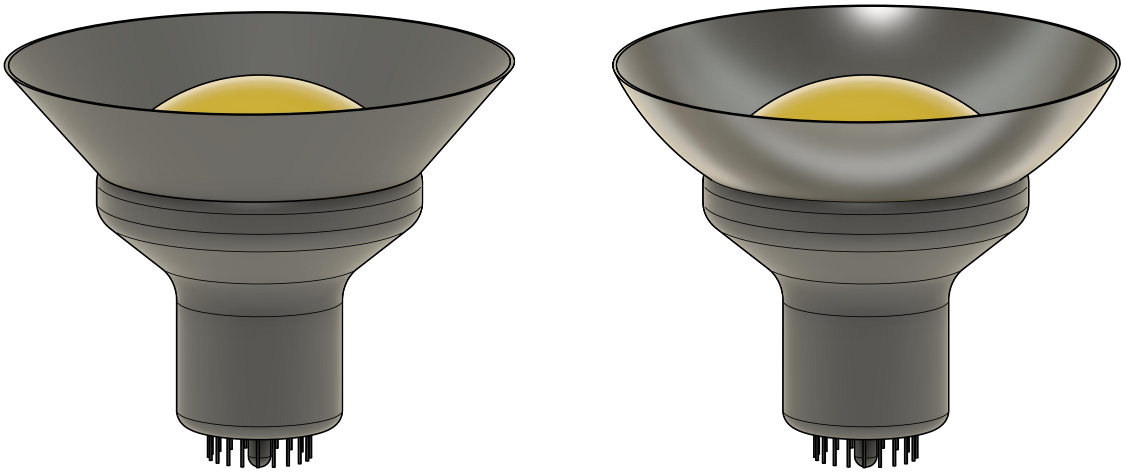

(a) Conical reflective surface.

(b) Ellipsoidal reflective surface.

Figure 3.11. Different possible designs for the reflective surface in the module LOM.

During the study of the reflectors, there are two possible designs. One of them is same than the design of the mDOM, that is to say, conical shape reflectors.

And another options is building the reflector from an ellipsoid instead of a cone. This design is based on the Winston cone, an parabola of revolution which maximize the collection of incoming rays [37]. The first model corresponds to Figure 3.11(a) and the second one to Figure 3.11(b).

3.4.2 Gel pads model

In order to decrease the cost of each digital optical module, another design for the LOM is considered. When one module is built, one of the most expensive part is the holding structure. Therefore, removing the holding structure would be a great advantage regarding the budget of the module. The idea is to change it for the so-called “gel pads”. A gel pad is a solid piece of gel that couples the PMT to the glass optically, but the shape at its edges has the same curvature as the reflectors. An illustration is shown in Figure 3.12.

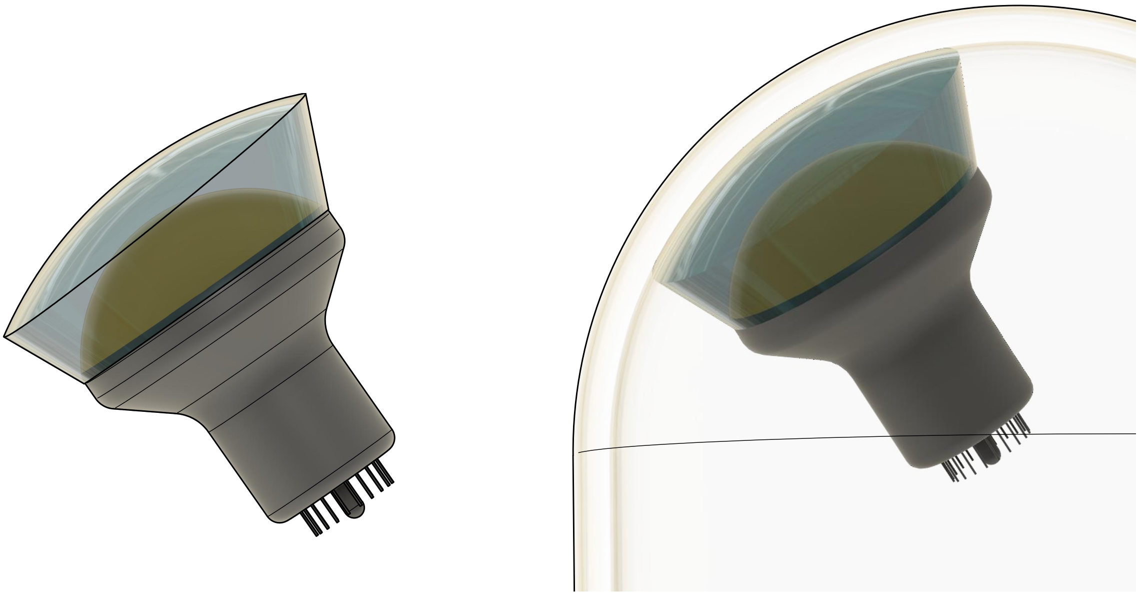

(a) Shape of the gel pads.

(b) Gel pads implemented with the glass of the pressure vessel.

Figure 3.12. Schedule of the gel pads of the LOM.

The different refractive index between air and gel would allow to reflect the photons which hit this gel pad and it directs them forward to the photocathode. This depends on the partial and total reflection of photons at the gel-air interface.

Another advantage is that if the holding structure is removed, photons do not have this obstacles to reach the photocathode from almost all directions. However, it is not clear if this system can have the same yield as the metallic reflector.

With the gel pads there are the same two possible designs as with the reflectors, having conical and ellipsoidal gel pads.

4 LOM geometry and simulations with Geant4

Geant4 is a software toolkit developed and maintained by the international Geant4 Collaboration [38]. This software aims to simulate different particles going through the matter using the Monte-Carlo method. It is freely available from the project web site [38]. Currently, it is used in several research fields like high energy particles, medical physics, or nuclear and accelerator physics.

Geant4 allows implementing several parameters from the geometry of the setup up to the physic processes which take place, or the models governing the interactions [39].

In this chapter, it is explained how to build the LOM using Geant4. It is a very important step for the simulations because here one has to define both the geometrical figures which will appear and their materials and properties.

Last, the primary particles and the physical processes considered are presented. Furthermore, a brief definition of the parameters to be optimized in the data analysis and several needed tools are provided.

4.1 General geometry

Creating a volume in Geant4 has three steps with three different classes. First, defining geometrically the solid. Second, adding the properties to the volume, i.e. defining its material, optical properties, etc. Finally, the object will be placed with a concrete position and orientation inside of a *world*.

The code of the LOM was created based on the Geant4 code of the mDOM, which was developed by Lew Classen and Björn Herold [31, 40].

The selection of the materials are the result from diverse studies with the mDOM [31]. For example, the pressure vessel is made of borosilicate glass from Vitrovex [41], the optical gel is Shin-Etsu [42], the reflective components will be built with Almeco V95 [43], etc.

The pressure vessel in Geant4 is modeled as a combination of two half-spheres with a cylinder tube. The cylinder tube is implemented at the center and the two half-spheres, one on each side. The cylindrical part for the LOM is larger than this part in the mDOM, making the module larger too. The holding structure is built with the same method. The optical gel fill up the slot space between the pressure glass vessel and the holding structure. The thickness of the pressure glass vessel is 14 mm while the thickness of the gel layer 4.5 mm.

This gel layer aims to provide optical coupling of the PMTs to the inner surface of the glass, because the refractive indexes of the ice ($n = 1.3475$), the glass ($n = 1.477$)

and the gel (n = 1.404) are similar [31, 41, 42].

The model of the PMT used in the LOM is not clear yet, however, the geometry and distribution of them are being optimized to try to fit PMTs as big as possible. The PMT considered for the LOM is a 4” Hamamatsu in development phase and its dimensions are shown in Figure 4.1.

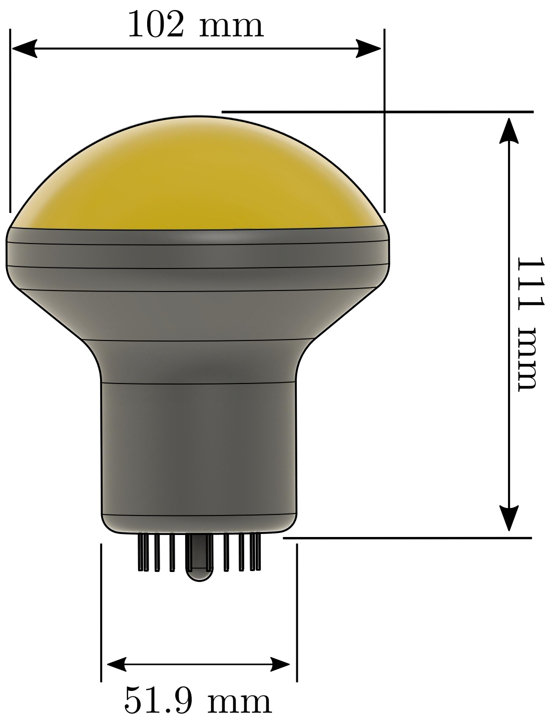

Figure 4.1. Dimensions of the 4” photomultiplier Hamamatsu which is in development phase.

The photocathode is not perfectly spherical. To build it, one approach is fit the shape to an ellipse and a circle joining them together in order to recreate the surface. The parameters of the ellipsoid and the sphere are obtained from a fit of the photocathode profile. The real profile view of the photocathode, and the ellipse and the circle used to fit it are shown in Figure 4.2.

Besides, the photocathode have a glass covering and the shape of this glass is defined by the same parameters as the photocathode. The lower part of the PMT is made of an absorbent material.

Notice that the PMTs are modeling without including its internal structure or a simulation of its response. This approach was justified by tests with the mDOM [31].

In total, there are 16 PMTs distributed in 4 rows where the position of the PMTs in each row is intercalated with the PMTs of its neighboring row. This can be observed in Figures 3.9(a) and 3.9(b). Regard the symmetry of the LOM, both halves are identical but with an angular offset.

Besides this, as mentioned, the PMTs are not aligned related to the center of the module either the center of the spherical glass. The position and orientation of the PMTs can be found in Appendix A. Figures 4.3 and 4.4 displays the whole module with the Geant4 visualization.

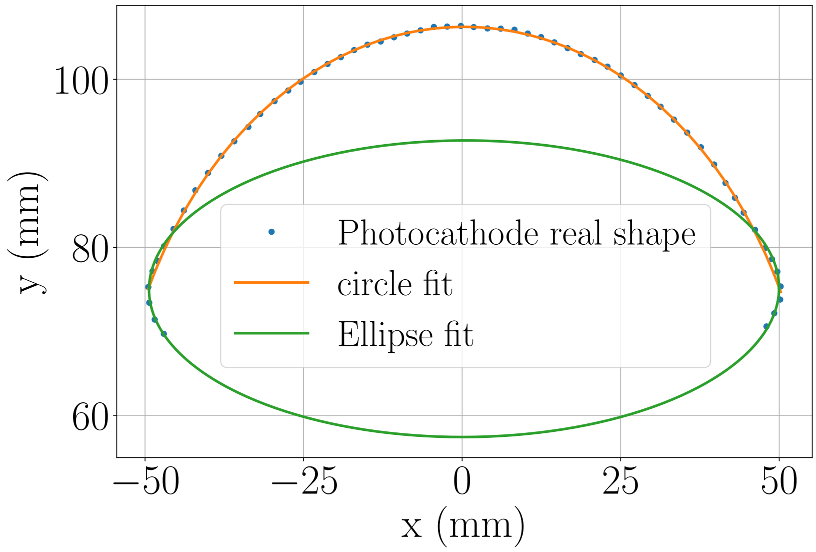

Figure 4.2. Fit of the photocathode surface.

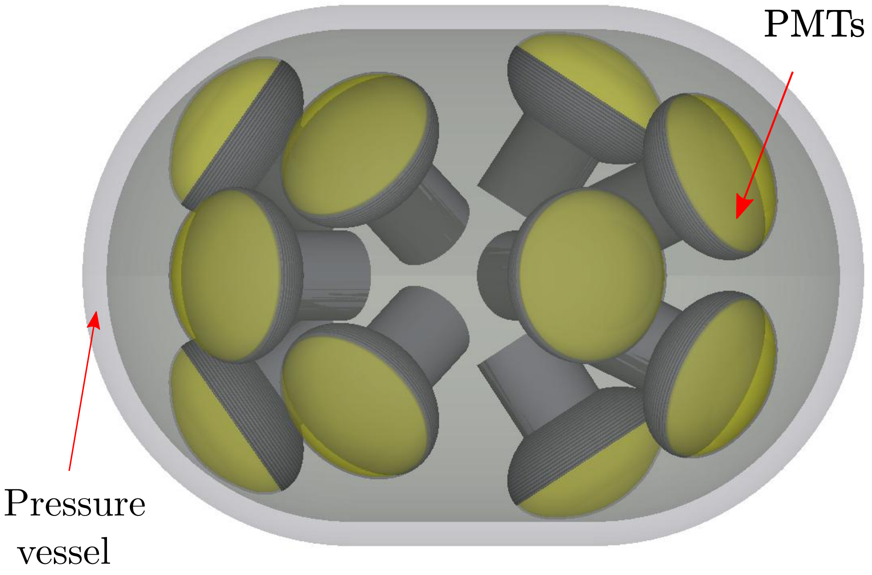

Figure 4.3. Module LOM built in Geant4 without the holding structure.

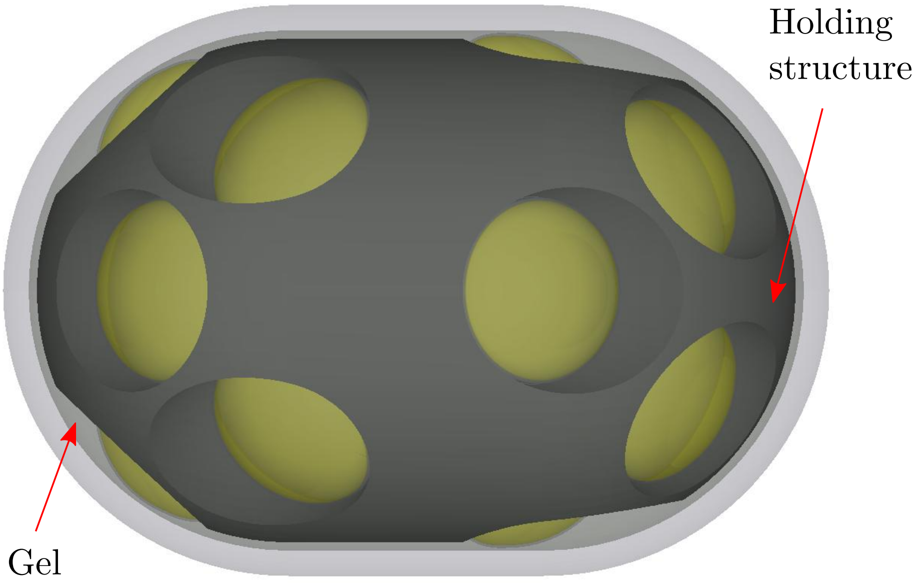

Figure 4.4. The LOM without reflectors built in Geant4.

4.2 Reflective components modeling

The reflective components redistribute the sensitivity across the solid angle and allow to gain effective area for each PMT, reflecting the photons forward the photocathode. Based on the mDOM, an option for the material of the reflector Alemco V95. The features of this material are included when the properties of the material are defined.

The explanation of the reflective structures modeling is developed for reflectors because it clarifies the process better. Also, the extension of the metallic reflectors to the gel pads model is fairly intuitive.

4.2.1 Conical reflectors

The reflectors with a conical design was used in the optical module developed for KM3NeT and the mDOM for IceCube.

This reflector is modeled as a cone matching the diameter of the photocathode with the minor radius of the cone. Thus, it is only necessary to cut the cone with the desired length, which correspond to the distance where the cone radius meet the photocathode radius. The cone is always cut off to go from the photocathode boundary till the limit of the holding structure. The thickness of the reflector is 0.5 mm. The process is shown in Figure 4.5.

The opening angle β shown in Figure 4.5(a) is the only free parameter to build the conical reflectors. Some examples with different angles are shown in Figure 4.6.

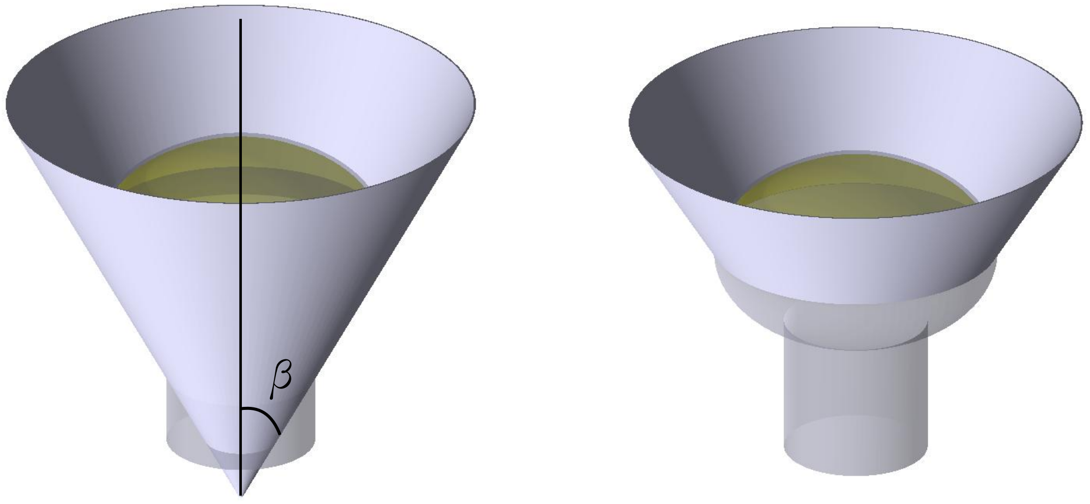

(a) Reflective cone without cutting off. (b) Reflective cone cut off.

Figure 4.5. The building of the reflective cone with Geant4. β angle is the opening angle of the cone used to build the conical reflector.

4.2.2 Ellipsoidal reflectors

To build this type of reflectors, an ellipsoid is used. The thickness is 0.5 mm and Figure 4.7 shows the adaptation process of the reflector to the PMT.

The ellipsoid used in this case presents symmetry over two axis hence there are two variables to modify the curvature and the design. They are called semi-axis a and semi-axis b and they are shown in Figure 4.7(a). The semi-axis b determines the opening of the reflector, this means, the reflector will be wider when the semi-axis b is increased. The influence of this parameter on the final result is similar to the influence of the opening angle for conical reflectors. For obvious reasons, this semi-axis can not be smaller than the photocathode radius.

On the other hand, the semi-axis a, modify mainly the curvature of the reflector. For high values of the semi-axis a, the reflector looks similar to a sphere, and for low values, it gets similar to the conical case. The value of this semi-axis is also constrained.

Some examples with different semi-axis $a$re shown in Figures 4.8 and 4.9.

4.3 LOM with holding structure and reflectors

In this section, the reflectors are implemented in the holding structure. As stated, the holding structure has the objective of giving support to the PMTs and for this purpose, it has 16 slots (holes) where they are fitted. Therefore, the support structure is modeled as solid object with openings fitting the form of the PMT and the reflector. A layer of gel of 4.5 mm is deployed between the pressure vessel and the holding structure,.

The reflectors are not supported on the holding structure, but there is a space

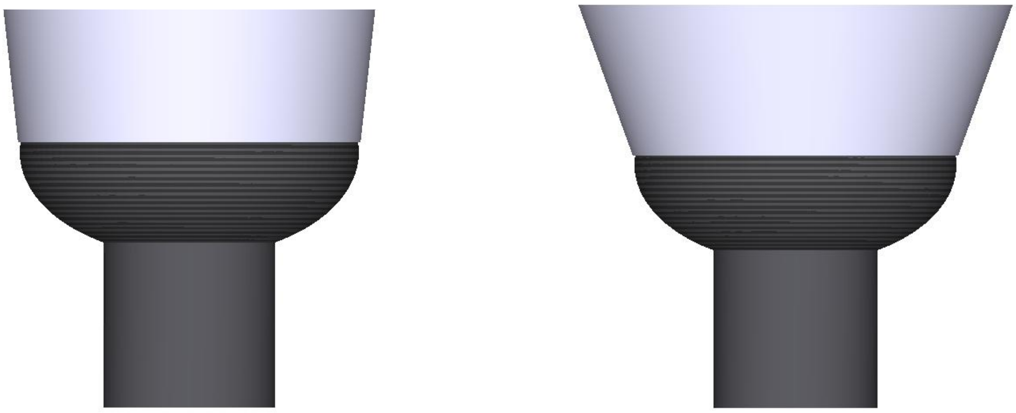

(a) Conical reflector with $\beta = 10$ degrees. (b) Conical reflector with $\beta = 30$ degrees.

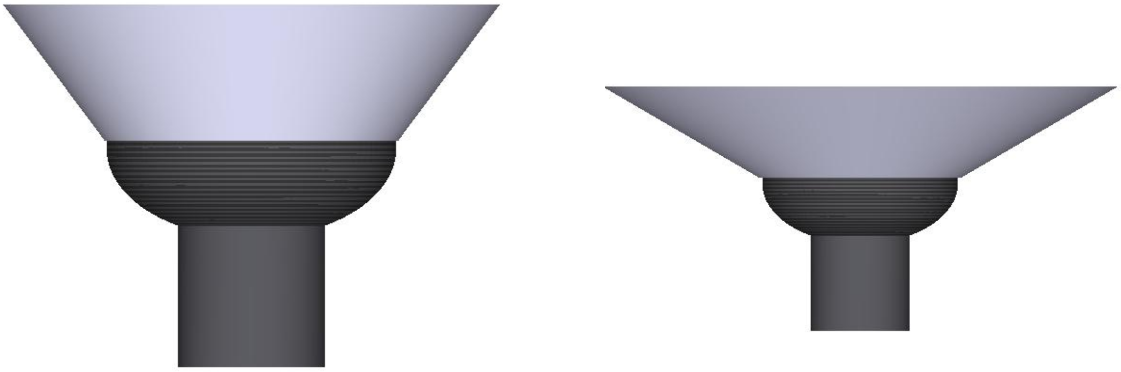

(c) Conical reflector with $\beta = 50$ degrees. (d) Conical reflector with $\beta = 70$ degrees.

Figure 4.6. The conical reflectors for different opening angles β.

between the reflectors and the holding structure. The gel fill this margin and the air is not trapped inside the slot. Also, in Geant4, building two surfaces perfectly overlapped can can be a source of errors. This margin is established at 0.25 mm and it is small enough to do not have any influence on the simulations.

Figure 4.10 shows the complete module using the holding structure and with conical reflectors.

4.4 LOM with gel pads

In this section, the building in Geant4 of the LOM with the gel pads implemented is shown. The idea is to remove the holding structure and to build solid “reflectors” of gel which hold the PMT and at the same time, reflect the incoming photons to the photocathode without losing too much efficiency compared with the metallic reflectors.

The gel pads should cover the photocathode and they touch the inner surface of

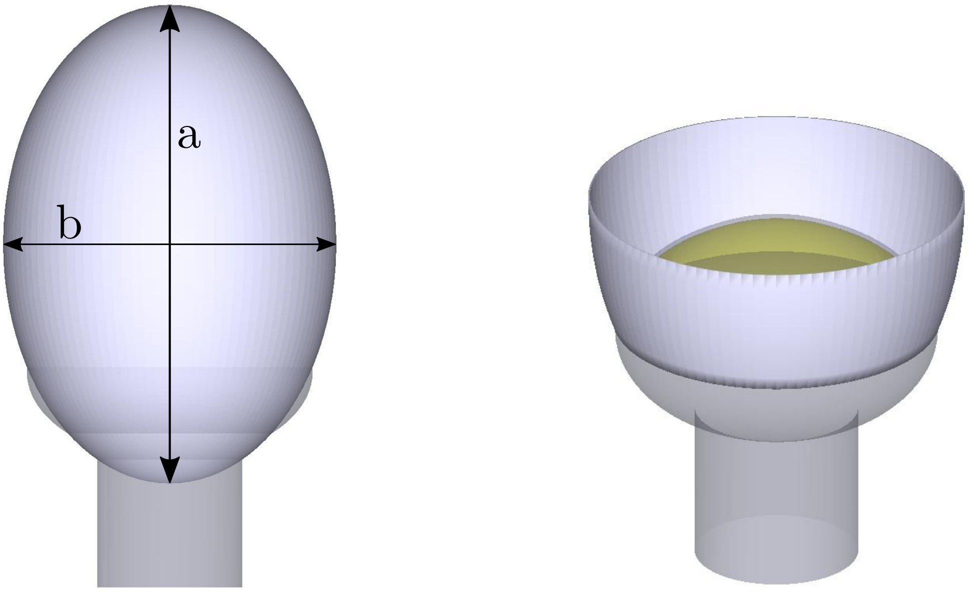

(a) Ellipsoidal reflectors without cutting off.

(b) Ellipsoidal reflector cut off.

Figure 4.7. The building of the ellipsoidal reflectors with Geant4.

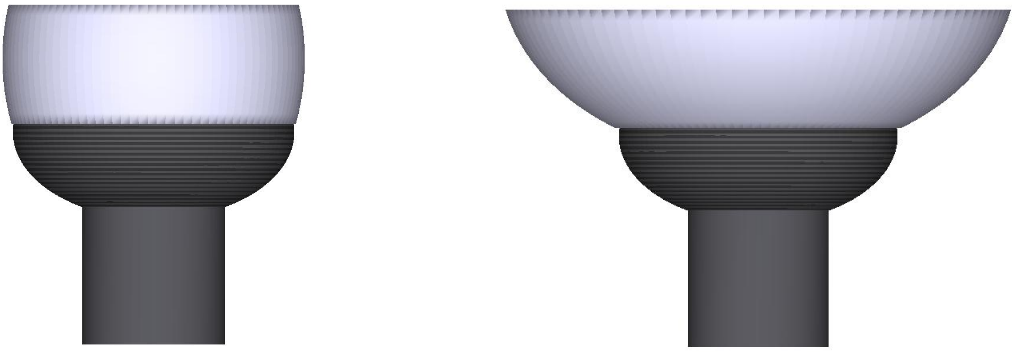

(a) Ellipsoidal reflector with a = 70 mm and b = 55 mm.

(b) Ellipsoidal reflector with a = 70 mm and b = 95 mm.

Figure 4.8. The behavior of the ellipsoidal reflectors when semi-axis b varies.

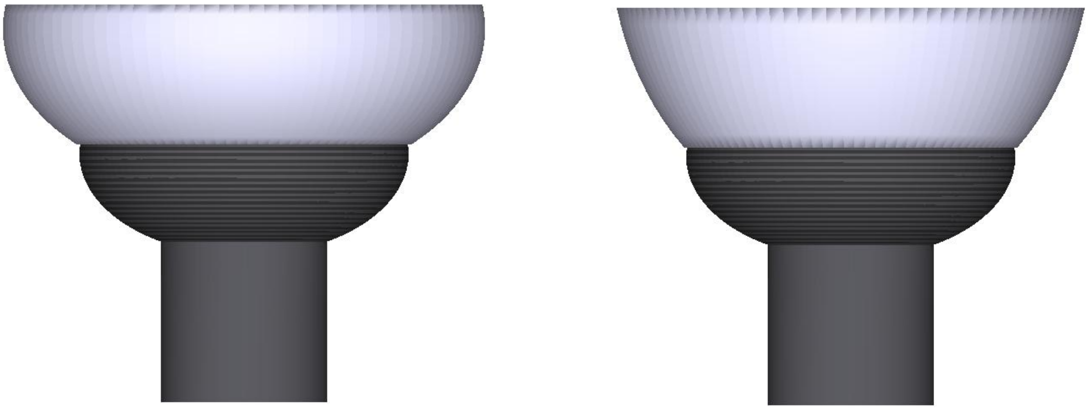

(a) Ellipsoidal reflector with a = 50 mm and b = 75 mm.

(b) Ellipsoidal reflector with a = 90 mm and b = 75 mm.

Figure 4.9. The ellipsoidal reflectors when semi-axis a varies.

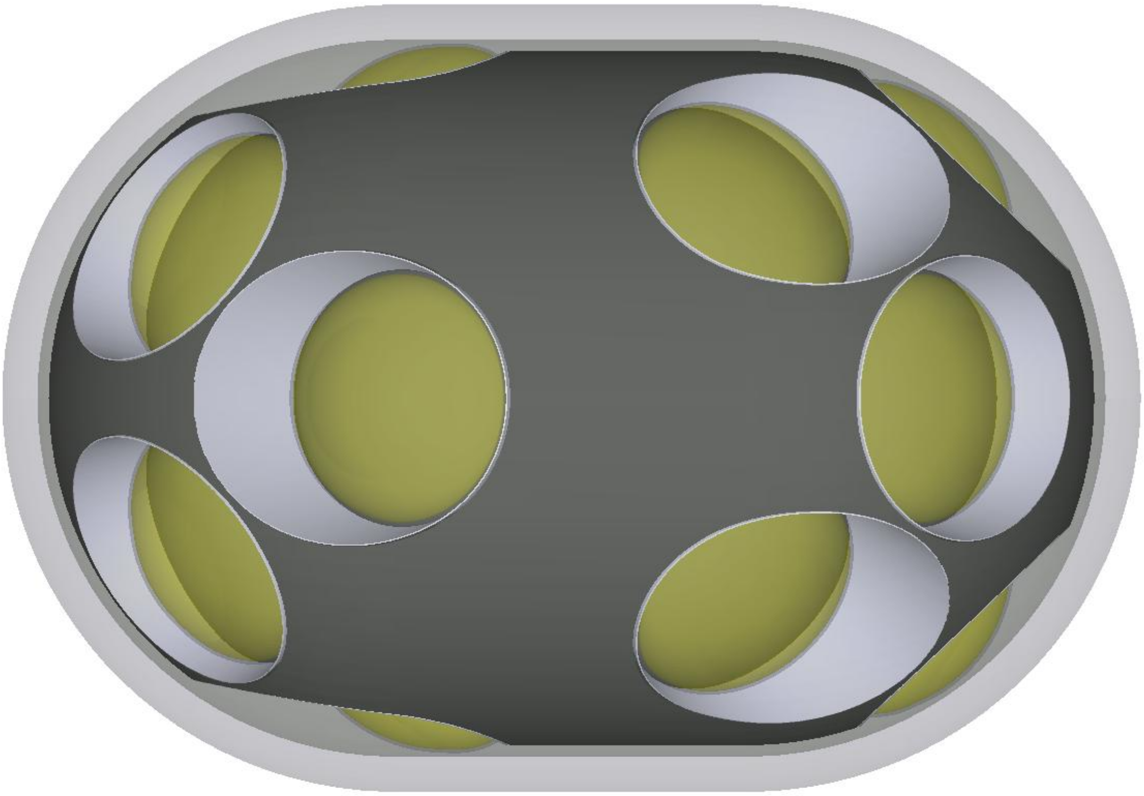

Figure 4.10. Complete module LOM with holding structure model using conical reflectors.

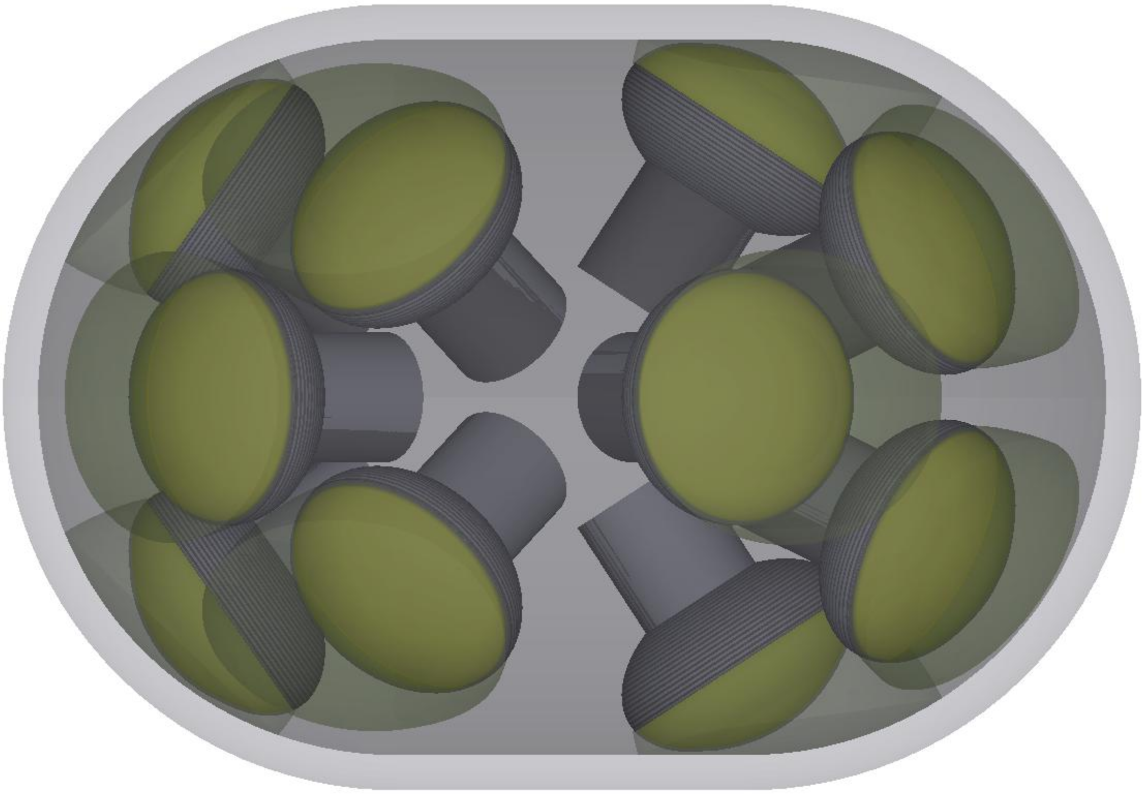

Figure 4.11. Complete module LOM with gel pads model using ellipsoidal gel pads.

the glass vessel hence the reflectors are cropped doing the intersection of the gel pads with the vessel.

Figure 4.11 shows the complete module using the ellipsoidal gel pads.

4.5 Physics and primary particles

As mentioned in previous sections, to get information about the neutrinos, the module will detect the Cherenkov radiation, produced by the charged particles, which in its turn, was produced by the neutrinos interacting with the South Pole ice. Hence, to get the capacity of the module to detect Cherenkov radiation and to study its optical properties, the primary particle for all the simulations is the photon directly.

The particle and processes used for our case is shown in Section 4.5.

Table 4.1. Particles and processes taken into account during all simulations.

Particle	**Geant4 class**	**Description**
Photon	G4OpAbsorption	Absorption of optical photons in Different materials
	G4OpBoundaryProcess	Boundary interactions when optical Photons changes medium

4.6 Simulation tools

In Section 2.3 it was stated that the charged particles emit Cherenkov photons when they are traveling through a dielectric medium. At a distance far enough from the particle, these Cherenkov photons reach as a plane wave and they are used to obtain information about the incoming neutrino.

With the objective of emulating these plane waves, the photons are generated in a disc shape emitting mono-energetic photons perpendicular to its surface with a constant density profile across the plane. The radius of the disc and the number of photons emitted depends on the simulations.

The simulations do not consider the quantum efficiency, that is to say, when a photon reaches the photocathode, it is registered as a detection. Then, it sums one to the number of hits and the process of this photon is over. As mentioned in Section 3.3, the quantum efficiency depends on the wavelength of the incoming photon but, in this case, the simulations are performed with a constant wavelength, so it is always possible to add this factor during the data analysis, applying the proper QE. The holding structure is considered as a perfect absorbent material.

There are four LOM designs: the module using the holding structure and conical reflectors, the module using the holding structure and ellipsoidal reflector, the module with conical gel pads and, the module with ellipsoidal gel pads. Furthermore, the shapes of the conical or ellipsoidal reflectors/gel pads depend on one or two variables, respectively.

The goal is to compare all these configurations, testing their capability to detect photons and studying their behaviors. To do that, the idea is to generate a plane wave of photons from different angles against the module and to measure how many of them the module can detect. The number of detected photons is denoted by $\mathrm{N}_{\mathrm{det}}$.

This way, $\mathrm{N}_{\mathrm{det}}(\theta, \phi)$ is an estimation of the angular acceptance of the module for a plane wave from a direction defined by the direction (θ, ϕ), . Through this magnitude the number of detections for each angle of incidence is known.

However, $\mathrm{N}_{\mathrm{det}}(\theta, \phi)$ depends on the number of photons, shape and size of the plane wave. Nevertheless, it makes sense that the tools which are used to compare, depend only on the design of the module. Achieving that it is possible using the *effective area.*

The *effective area* $\mathrm{A}_{\mathrm{eff}}$ compensates these effect of the external parameters by normalizing the number of detected photons with the area of the plane wave and the number of emitted photons:

$$\mathrm{A}_{\mathrm{eff}}(\theta, \phi) = \frac{\mathrm{N}_{\mathrm{det}}(\theta, \phi)}{\mathrm{N}_{\mathrm{emit}}} \cdot \mathrm{A}_{\mathrm{beam}}, \tag{4.1}$$

where $\mathrm{N}_{\mathrm{emit}}$ is the number of photons emitted, $\mathrm{A}_{\mathrm{beam}}$ is the area of the beam.

So far, the effective area is defined for a particular direction and its distribution across the solid angle provides some information, e.g. concerning the response homogeneity. For a more global comparison, the mean effective area is the figure of merit. This will be symbolized by $\mathrm{A}_{\mathrm{mean}}$ and it avaraged over the solid angle. With this magnitude, the different designs can be compared easily. It is given by

$$\mathrm{A}_{\mathrm{mean}} = \frac{1}{\mathrm{A}_{\mathrm{total}}} \iint \mathrm{A}_{\mathrm{eff}}(\theta, \phi) \cdot \sin(\theta)\, d\theta\, d\phi, \qquad \mathrm{A}_{\mathrm{total}} = \iint \sin(\theta)\, d\theta\, d\phi. \tag{4.2}$$

In the real simulations, the variables θ and ϕ are discrete hence the mean effective area is calculated as

$$\mathrm{A}_{\mathrm{mean}} = \frac{1}{\mathrm{A}_{total}} \sum_{\theta,\phi} \mathrm{A}_{\mathrm{eff}}(\theta, \phi) \cdot \sin(\theta)\, \Delta\theta\, \Delta\phi, \qquad \mathrm{A}_{total} = \sum_{\theta,\phi} \sin(\theta)\, \Delta\theta\, \Delta\phi. \tag{4.3}$$

Another important aspect in the simulations is the distributions of the angles θ and ϕ around the module. At the beginning, one could think of to sample linearly in theta and phi, however this would not distribute the angles uniformly across the sphere. To achieve it, a python package *healpy* is used. This package is a pixelization algorithm devised by Krzysztof M. Górski based on *HEALPix*[15] [44].

healpy distributes the intervals of angles uniformly from the number of pixels that one wants to have in the sphere. The different distributions obtained as the number of pixels increases are shown in Figure 4.12. As a result of this tool, the area of each pixel in the sphere is the same hence the calculation of the mean effective area is simplified as

$$\mathrm{A}_{\mathrm{mean}} = \frac{1}{\mathrm{A}_{total}} \sum_{\theta,\, \phi} \mathrm{A}_{\mathrm{eff}}(\theta, \phi) \cdot \mathrm{A}_{\mathrm{pixel}} = \frac{\mathrm{A}_{\mathrm{pixel}}}{\mathrm{A}_{total}} \sum_{\theta,\, \phi} \mathrm{A}_{\mathrm{eff}}(\theta, \phi), \tag{4.4}$$

$$\mathrm{A}_{total} = \sum_{\theta,\, \phi} \mathrm{A}_{\mathrm{pixel}} = \mathrm{N}_{\mathrm{pixels}} \cdot \mathrm{A}_{\mathrm{pixel}}, \tag{4.5}$$

where $\mathrm{A}_{\mathrm{pixel}}$ is the area of one pixel and $\mathrm{N}_{\mathrm{pixels}}$ is the number of pixels in the sphere. Along this thesis, the *healpy* tool is used or not depending of the goal of each simulation.

The statistical uncertainty of the variables is treated using the quadratic propagation of errors. The number of hits corresponds to a Poisson distribution, hence the uncertainty of the number of detection and therefore the uncertainty of the effective

---

[15] An acronym for Hierarchical Equal Area isoLatitude Pixelization.

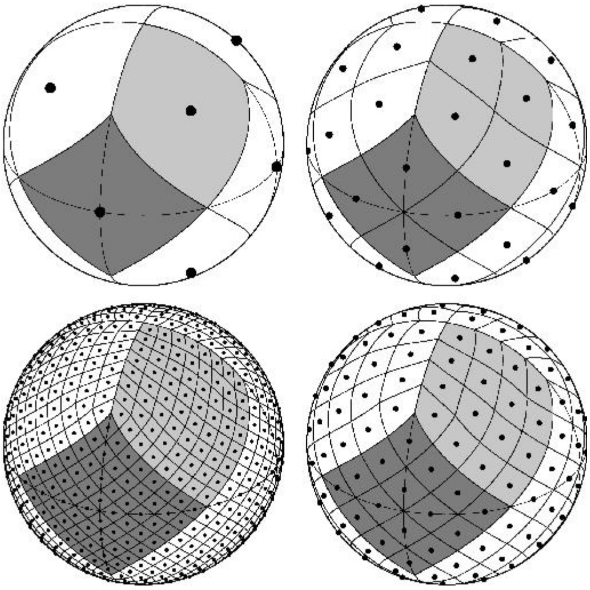

Figure 4.12. Distributions of pixels of HEALPix. Taken from [44].

area is defined by

$$\sigma_{\mathrm{N_{det}}}(\theta,\phi)=\sqrt{\mathrm{N_{det}}(\theta,\,\phi)},\qquad \sigma_{\mathrm{A_{effec}}}=\frac{\sigma_{\mathrm{N_{det}}(\theta,\phi)}}{\mathrm{N_{emit}}}\cdot\mathrm{A_{beam}}. \tag{4.6}$$

For the uncertainty of the mean effective area, if the whole sphere is simulated it is not possible to apply the formula of the quadratic propagation directly because the symmetry of the module should be taken into account. Simulating the whole sphere is the same that if an octant of the sphere was simulated eight times because for a value of theta θ and a value of phi ϕ, there are eight equivalent simulations along the sphere.

For this reason, along the simulations of this thesis, only the octant is simulated. If one octant is simulated, the statistics is affected, but it was already compensated when the number of photons in each simulation was decided.

The uncertainty of the mean effective area is calculated as

$$\sigma_{\mathrm{mean}}=\sqrt{\left(\frac{\mathrm{A_{pixel}}}{\mathrm{A_{total}}}\right)^{2}\sum_{\theta,\,\phi}^{\pi/2}\sigma^{2}_{\mathrm{A_{effec}}(\theta,\,\phi)}}. \tag{4.7}$$

5 Reflective components for single PMT

Before the optimization of the whole module, the effects of the variation of the different parameters describing the shape of the reflective components are investigated. For this, in this chapter the efficiency for a single PMT with its reflective structure is simulated. The variables for the two types of reflectors are different hence to compare them, they are separated into conical reflective components, studied in Section 5.2, and ellipsoidal reflective components, in Section 5.3.

5.1 Setup of the simulations

In Figure 5.1(a) the simulation of one PMT with reflectors (in this case a conical reflector but it is the same for ellipsoidal reflectors.) is depicted. The geometry presents rotational symmetry so for each value of zenith angle, the results are equivalent for any given azimuth angle. Therefore, the simulations have only one directional variable, zenith angle (θ), ranging from 0 to 180 degrees. The diameter of the beam is 200 mm and the number of photons is one million.

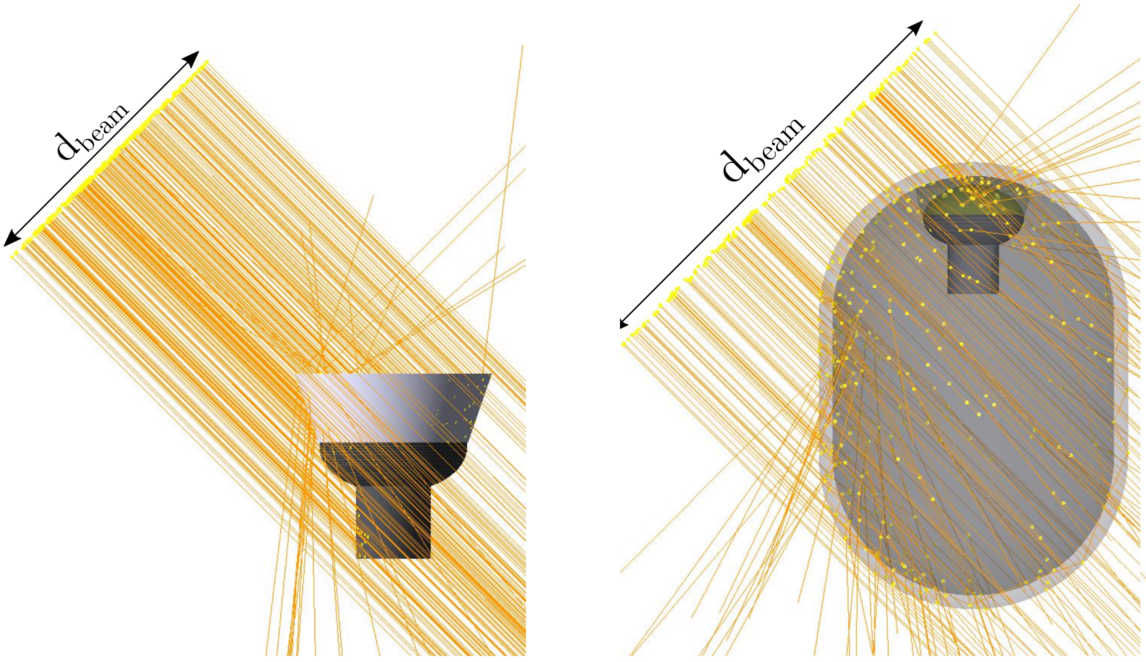

(a) Simulations with one PMT with conical reflector. d_{beam} in this case is 200 mm.

(b) Simulations with one PMT with ellipsoidal gel pad. d_{beam} in this case is 460 mm.

Figure 5.1. Simulations with only one PMT. d_{beam} is the diameter of the beam.

Figure 5.1(b) shows the simulations of one PMT with gel pads (in this case, is for ellipsoidal gel pads but it is also for conical gel pads). It would not make sense to simulate the gel pads without the glass of the pressure vessel because an important factor in this model is the change of the medium between the gel and the glass, therefore it is included. Also in this case, the geometry has rotational symmetry so the directional variable is the zenith angle θ. However, it is necessary to increase the diameter of the beam up to 460 mm to cover the whole module and to increase the number of photons up to three million to get a reasonable statistics for the number of detection.

The environment of all simulations is ice. It could be thought that this is not a valid situation for the case of the simulations of the only one PMT with reflectors because inside of the module, the reflector will be in contact with gel instead of ice. However, the refractive indexes of both mediums are not too much different and these simulations aim to establish the general behavior of the reflectors hence it is also a valid situation in this case.

For these type of simulations with only one PMT, the definition of the mean effective area is different, since there is only one directional variable, and is calculated as

$$\mathrm{A}^{\mathrm{one}}_{\mathrm{mean}} = \frac{1}{\mathrm{A}_{total}} \sum_{\theta} \mathrm{A}_{\mathrm{eff}}(\theta)\, \Delta\theta, \qquad \mathrm{A}_{total} = \sum_{\theta} \Delta\theta = 180 \text{ degrees}. \tag{5.1}$$

5.2 Conical reflective structures for a single PMT

The variable to modify the conical reflective structures is the opening angle of the cone used to build them, therefore, this is the main parameter to take into account. The effective area for the conical reflector and the conical gel pads are shown in Figures 5.2 and 5.3 respectively.

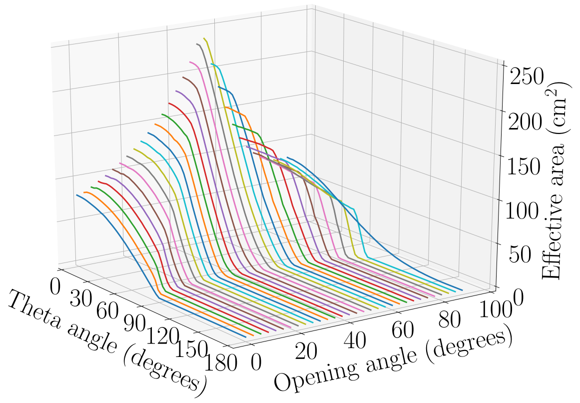

Figure 5.2. Effective area for one PMT with reflectors as a function of the angle theta and of the opening angle.

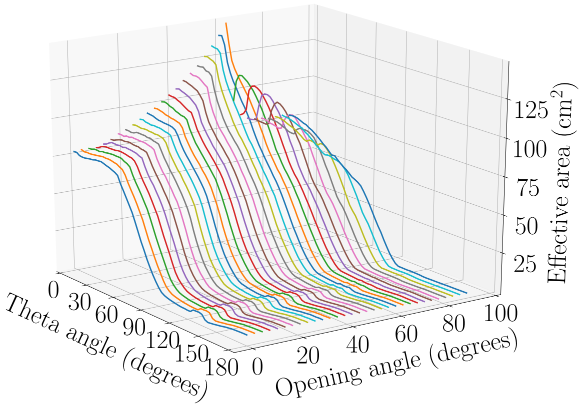

Figure 5.3. Effective area for one PMT with gel pads as a function of the angle theta and of the opening angle.

In Figure 5.2, the dependence of the effective area with the opening angle shows a maximum around 50 degrees. This peak does not mean that this angle corresponds to the best value for the mean effective area, since this maximum is only valid for $\theta = 0$.

If the dependence with theta angle is analyze it is found that the value for the effective area is major when the photon reaches the PMT from $\theta = 0°$. Also, starting from a certain angle, the effective area drops to zero. It makes sense because the reflector is surrounding the photocathode and it makes it impossible to detect a photon incoming from behind of the reflector.

Comparing all opening angles, the behavior for the opening angle 90 degrees is different because it reaches zero at a much larger value of theta. This should not be surprising because this geometry corresponds with a flat disc surrounding the PMT.

The results for the gel pad, presented in Figure 5.3, show a different behavior. It also has a peak, but after its maximum, the effective area falls abruptly.

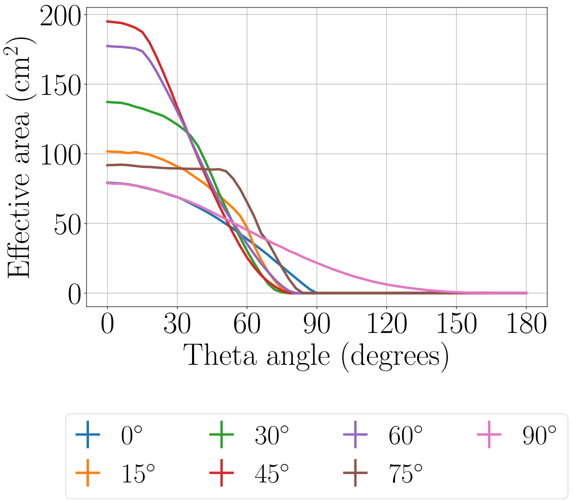

Figure 5.4. Effective area for one PMT with reflectors as a function of the angle theta. The colors represent the different opening angles in degrees.

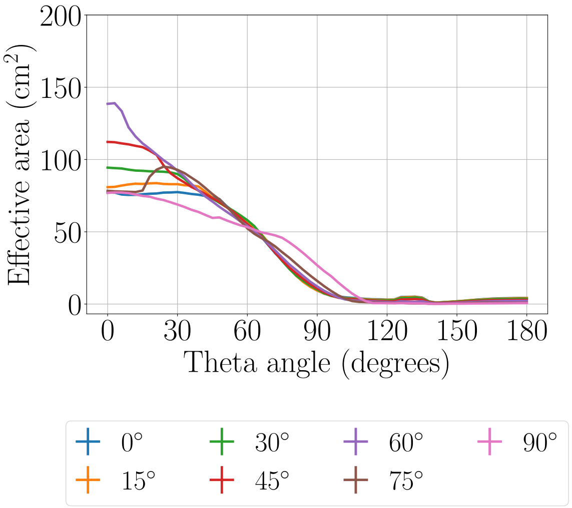

Figure 5.5. Effective area for one PMT with gel pads as a function of the angle theta. The colors represent the different opening angles in degrees.

One of the most important differences compared with the reflectors is that one can find detection for any angle theta, i.e. there is not a value of theta from so which the effective area falls to zero. That means that it is possible to detect photons incoming from behind of the photomultiplier. This is due to the fact that photons can go through the gel pads, reaching the photocathode even when they are going incoming from the contrary side of it.

Figures 5.4 and 5.5 help to compare this aspect better because they show the dependence of the effective area against the theta angle for different values of the opening angles. Here it is clear that for the case with reflectors, the effective area falls to zero while with gel pads there are detections for almost all theta angles.

In Figure 5.5, the line corresponding to the opening angle 90 degrees also drops to zero and it follow the same feature of the reflector lines. It makes sense because it is also a ”flat” gel pad and it produces that all the upper part of the pressure vessel is filled with gel, and thus photons are barely deviated from the gel pads.

Besides this, the mean effective for both cases is calculated and presented in Figure 5.6. Looking at this figure, one could think that the reflectors have better efficiency than the gel pads, nevertheless, it is not reliable to compare the values of both lines because they have been originated from two simulations with different configurations. The simulations with the gel pad have the pressure vessel and this produces absorption and reflections which do not happen in the simulation with the reflector.

The case with reflectors shows a very hard dependence with a well-defined peak around 50 degrees. The dependence of the effective area of the gel pads with the opening angle is flatter. The peak maximum is around 60°, quickly falling for larger angles.

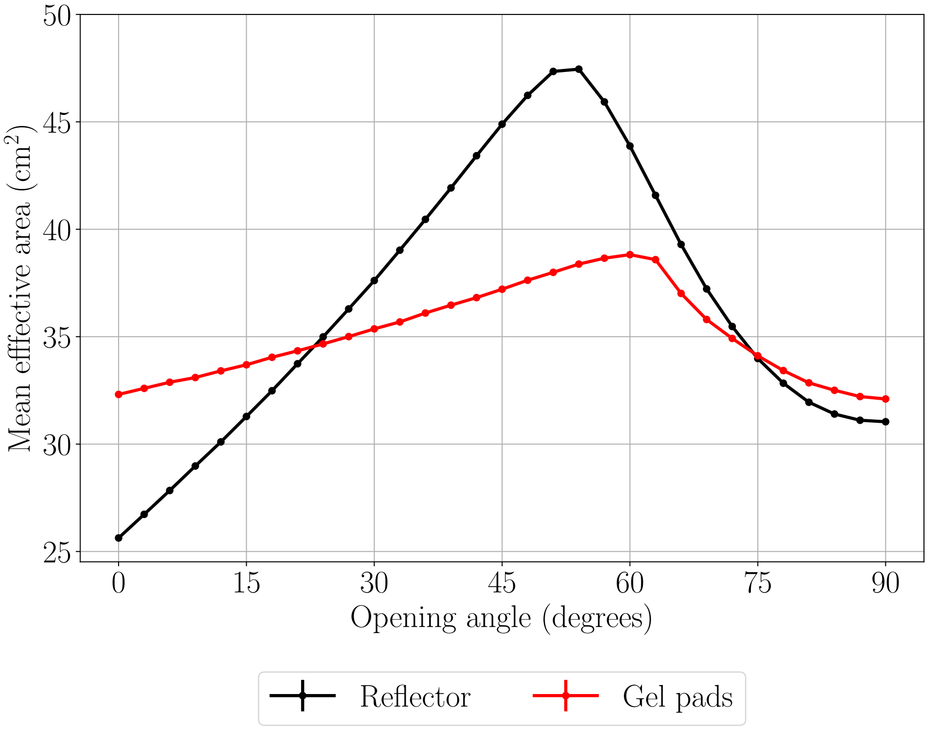

Figure 5.6. Mean effective area as a function of the opening angle for reflectors and for gel pads. The error bar are smaller than the marker size.

5.3 Ellipsoidal reflective structures for a single PMT

The ellipsoidal reflectors and gel pads can be modified by two variables, the semi-axis a and the semi-axis b used to build them. As there are two parameters, it is not possible to plot the effective area as with the conical reflector so the mean effective area is studied first.

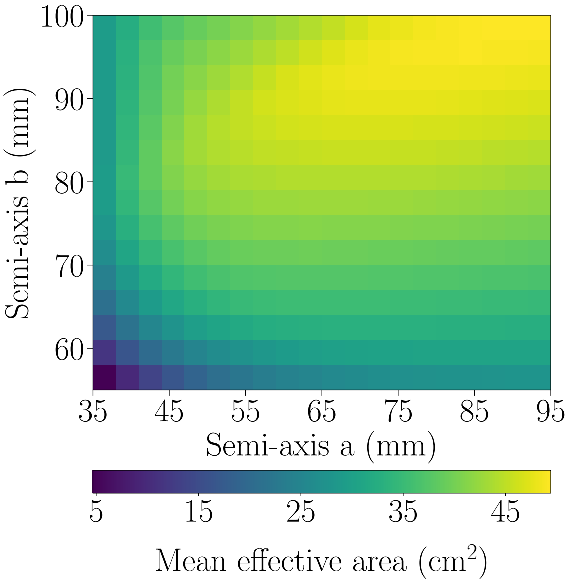

Figure 5.7. Mean effective area for reflectors as a function of both semi-axes.

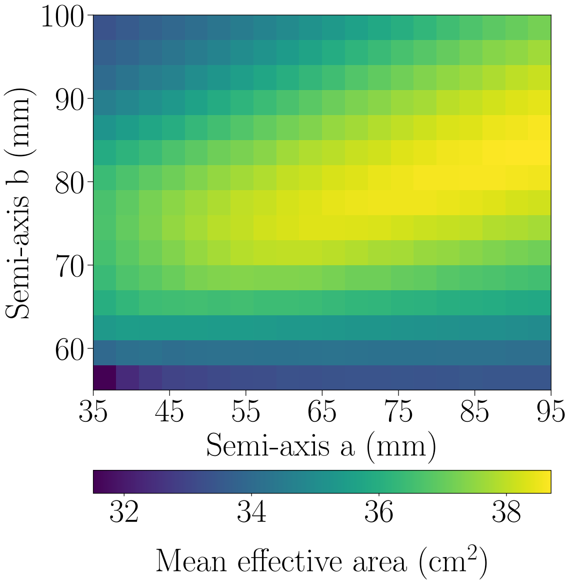

Figure 5.8. Mean effective area for gel pads as a function of both semi-axes.

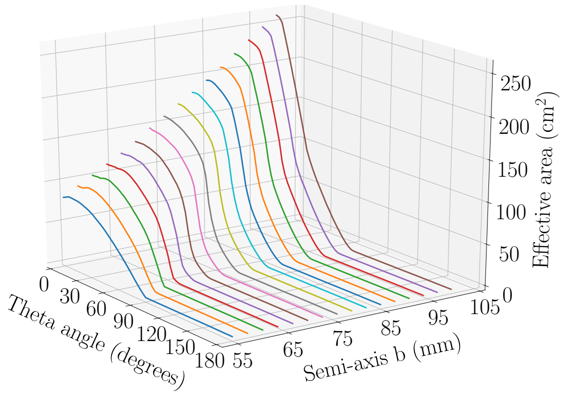

Figure 5.9. Effective area for reflector as a function of the semi-axis b and the theta angle. Semi-axis a fixed at 86 mm.

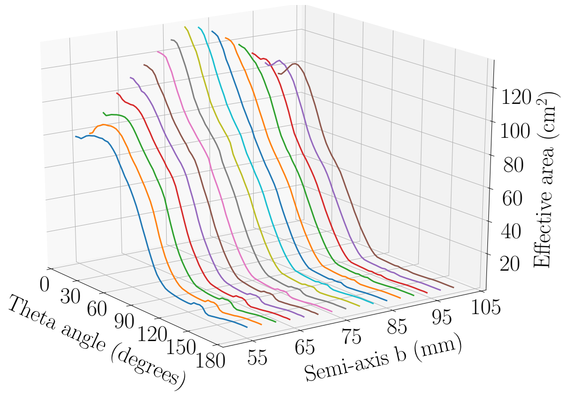

Figure 5.10. Effective area for gel pads as a function of the semi-axis b and the theta angle. Semi-axis a fixed at 86 mm.

The mean effective area for the simulations with a single PMT for ellipsoidal reflector and gel pads are shown in Figures 5.7 and 5.8 respectively.

Looking at Figure 5.7, the dependence with both semi-axes is similar. The value of the semi-axis b for which the mean effective area has a maximum, increases as the semi-axis a increases too.

In Figure 5.8 the mean effective area with gel pad is shown. In this case, the dependence with the semi-axis a is very similar to the case with the reflector. Nevertheless, if the dependence with the semi-axis b is analyzed, a peak is found around 70 - 90 mm depending on the value of the semi-axis a.

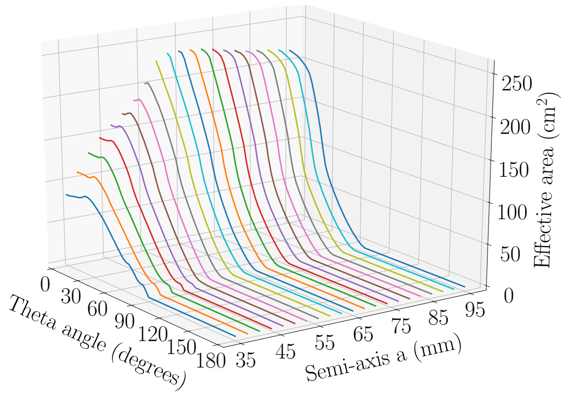

Figure 5.11. Effective area for reflector as a function of the semi-axis a and the theta angle. Semi-axis minor in 91 mm.

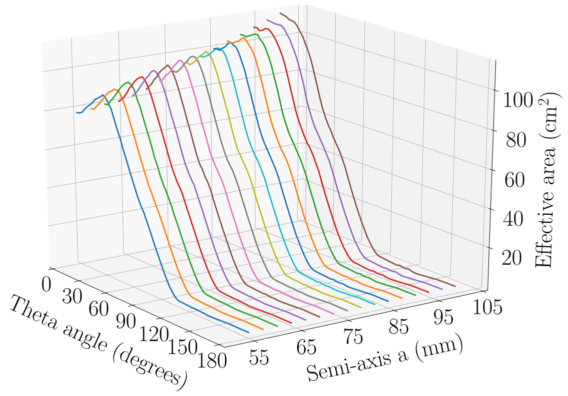

Figure 5.12. Effective area for gel pads as a function of the semi-axis a and the theta angle. Semi-axis b in 91 mm.

In both cases, the mean effective area reaches its minimum values for values of the semi-axis a around 35-45 mm, and above all in Figure 5.7, where it falls up to 5-15 cm^2. It makes sense because for these values, the semi-axis a is shorter than the semi-axis b. This configuration results in the reflector covering a region of the photocathode reducing the number of detections. With gel pads, this happens too but since the photon can go through the gel pads, the drop in effective area is not as large.

In order to show better these behaviors, it is fixed first the semi-axis b and later the semi-axis a, and plot them as a function of the other one and the theta angle. The semi-axis b is fixed at 91 mm and the semi-axis a at 86 mm.

Figures 5.9 and 5.10 shows the different dependence with the semi-axis b for reflector and gel pads. As mentioned, for gel pads a peak appears (around 74 mm in this case) while for reflector the tend remains upward.

In Figures 5.11 and 5.12, the dependence of the mean effective area with the semi-axis a is shown. This dependence is more similar for both cases. In the case of the reflectors, the effective area starts to drop when the semi-axis a is less than 55 mm, while with the gel pads this is not the case. Here it is reflected very well what happens when the reflector covers the photocathode partially.

6 Optimization of the reflective components

In this section, the optimization of the reflective components is carried out, simulating the whole module with all components.

First of all, the Geant4 code is cross-checked in Section 6.2 to make sure it works properly. To do that, the result of a testing simulation obtained with the LOM are compared with the result for the mDOM and it is studied if the data makes sense and the model works.

Afterwards, the parameters which define the reflectors and gel pads are studied optimizing the mean effective area. Again, the simulations are separated in two parts: first with conical reflective components, in Section 6.3 and then with ellipsoidal reflective components, in Section 6.4.

6.1 Setup of the simulations

The simulations of the whole module are very similar to the simulations of one PMT with gel pads but the target is the complete structure with the 16 PMTs. The diameter of the beam is also 460 mm and 1.5 x 10^6 photons are emitted. In Figure 6.1, an example of the simulation with the whole module is depicted.

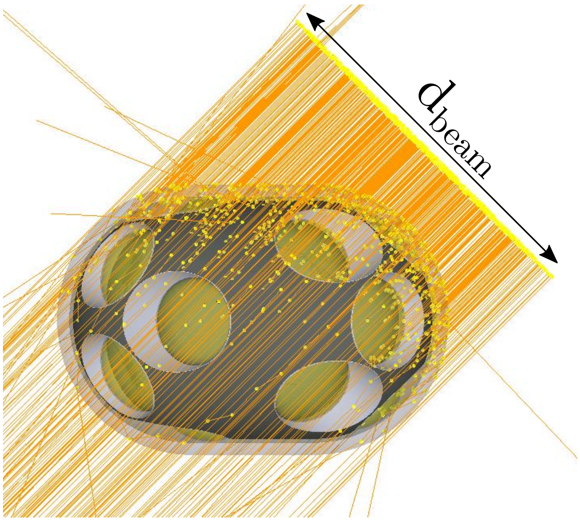

Figure 6.1. Example of a simulations with the whole module.

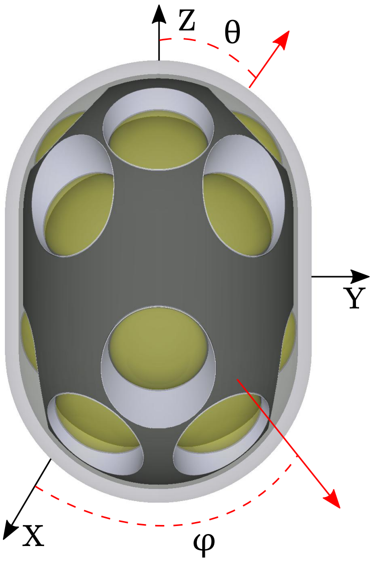

Figure 6.2. Frame of references used for the LOM.

Also, the spherical coordinates are used to define the angles, where θ and ϕ refer to zenith and azimuth angles respectively. The range for θ is from -90 to 90 degrees and for ϕ from -180 to 180 degrees. The angles θ and ϕ are shown in Figure 6.2.

6.2 mDOM cross-check

In order to get a sanity check of the model built of the LOM, a testing result is compared with the result obtained with the mDOM. The model with holding structure and reflectors is used for this purpose.

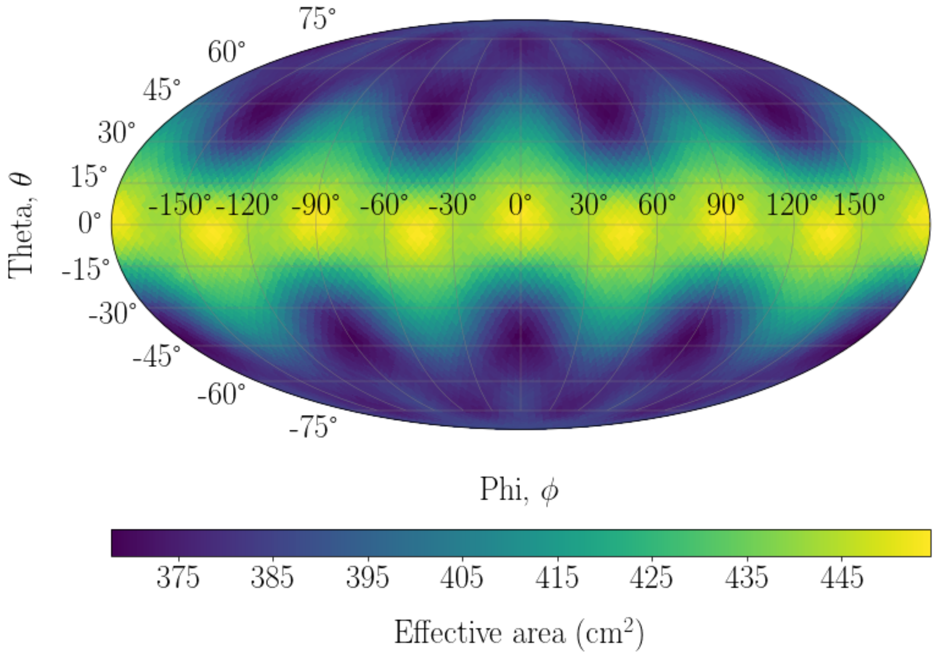

Figure 6.3. Effective area for the LOM with reflectors with an opening angle of 30°.

Concerning the opening angle of the reflectors, in the mDOM it was set to 52° [31]. Due to issues that will be discussed later, the maximum value of the opening angle which is possible to implement in the LOM is 30 degrees.

The number of photomultipliers in the mDOM is larger than for LOM, however, the area of each photocathode is larger for the LOM. Taking these factors into account when the results are analyzed, both should be reasonably close.

In Figure 6.3 is shown the projection of the effective area for the LOM. The color bar determines the effective area when 1.5 x 10^6 photons were simulated against the module in the direction defined by the angle theta and phi.

This Figure 6.3 is shown with the name of the angles and the ticks with their values to make the sense of the plots clear. In the following sections , it will be without all these labels with the goal of observing better the patterns.

Actually, to compare this simulations with the simulations from the mDOM, the mean effective area is calculated. Also, it is necessary to extrapolate the value obtained with respect to the number of photomultipliers and the area of the photocathode.

The value obtained for the mean effective area is $\mathbf{(404.24 \pm 0.67)\,cm^2}$ and the value obtained for the mDOM with the same conditions (wavelength, ice as medium, etc) during the simulation is **380.85 cm²** [31].

As mentioned, the radius of the photocathode used in LOM is 51.2 mm and the photocathode implemented in the mDOM is 40.17 mm. Also, the LOM has 16 PMTs while the mDOM has 24. In this way, the needed calculation to compare them is given by

$$(404.24 \pm 0.67)\,\mathrm{cm}^2 \cdot \frac{24}{16} \cdot \frac{\pi \cdot 40.17^2}{\pi \cdot 51.2^2} = (373.02 \pm 0.62)\,\mathrm{cm}^2. \tag{6.1}$$

If this result is compared with the result for the mDOM, it is found that they agree reasonably well and that indicates that the model works properly.

Furthermore, the relative uncertainty of the result is lower than 1 %, which shows that the number of simulated photon is enough for the purposes of this work.

6.3 Conical reflective structures

In this section, the module equipped with the conical reflectors and gel pads is studied.

The parameter involves in the shape of the conical reflective components is the opening angle of the cone used to build them. In order to compare all possibilities, the whole module is simulated with different opening angles and for that, it is important to know the range of this variable in each case.

First, for the case with the holding structure, from Figure 4.6 it is known that the reflector is larger as the opening angle increases. The model with the holding structure presents metallic reflectors hence they are not allowed to overlap each other. For this reason, the range of the opening angle is limited by 0 - 30 degrees. For a larger opening angle, it is not possible to implement them.

For the model with gel pads, there is no this limitation. It is supposed that the gel pads can touch each other. A discussion of the feasibility of this construction is outside of the scope of this thesis. It means that the range of the opening angle is from 0 to 90 degrees.

In Figures 6.4 and 6.5 the mean effective area is shown for the module with reflectors and gel pads, respectively, as a function of the opening angle. Figure 6.4 shows the case with reflectors. The mean effective area increases as the opening angle increases and the curve follows a clear linear trend. Also, the maximum correspond to the maximum value possible for the opening angle.

In Figure 6.5 the mean effective area for conical gel pads is shown. At the beginning, for low values of the opening angle, the curve increases slowly up to reach its maximum value. It corresponds to an opening angle around 60 degrees. After this peak, the mean effective area falls quickly reaching its minimum value at 90 degrees.

Comparing Figures 6.4 and 6.5, the trend for both curves are similar in the range

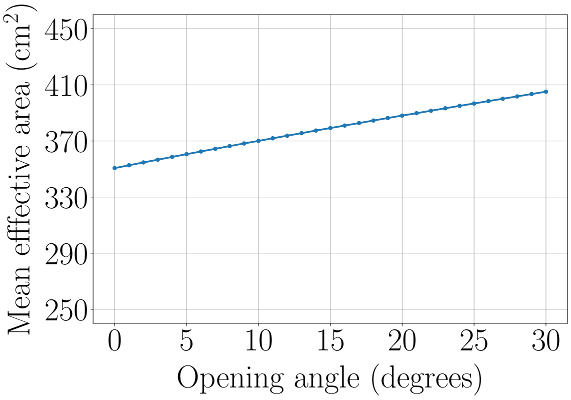

Figure 6.4. Mean effective area as a function of the opening angle with the module with the holding structure. The error bars are smaller than the data markers.

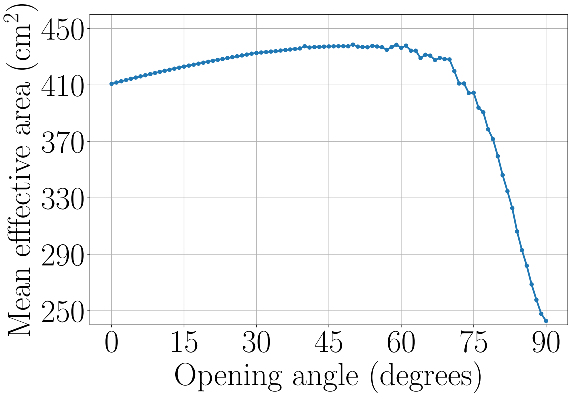

Figure 6.5. Mean effective area as a function of the opening angle with the module with the gel pads. The error bars are smaller than the data markers.

where it it possible to compare them (0 - 30 degrees).

The range of the mean effective area is the same for both plots hence they can be compared directly. It is easy to see as in the range where is possible to compare them, the model with gel pads presents better results with a mean effective area 7% larger.

The reason for that, stems from the capability of the gel pads to detect photons originate from behind themselves. The model with gel pads has no holding structure and this allows the photons to travel through the module. Also even if the photons do not travel through the module, the holding structure does not shadow the photocathode. These factors make that the number of detections rises.

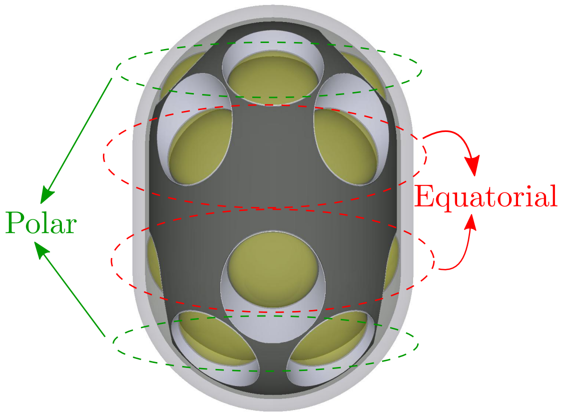

Figure 6.6. Sketch of the LOM showing the equatorial and polar PMTs.

To check if this is true the effective area is analyzed in both cases, but only one PMT is considered. It is not the same as in the last chapter, because now the photons are detected by one PMT but implemented inside a module with other PMTs, which can introduce absorption and reflections of photons.

Inside the module, there are two different position for the PMT and the remaining positions are symmetrical, so it makes sense to analyze what happens for these two positions. The 8 (4 on each side) PMTs placed in the poles are called polar PMTs and the 8 (4 on each side) PMTs placed in the central rows are called equatorial PMTs. Figure 6.6 shows a sketch of these two positions.

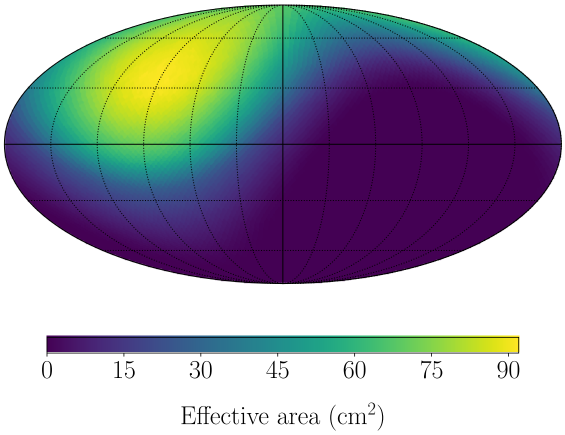

Figure 6.7. Effective area for reflector in the polar position. Opening angle 20°.

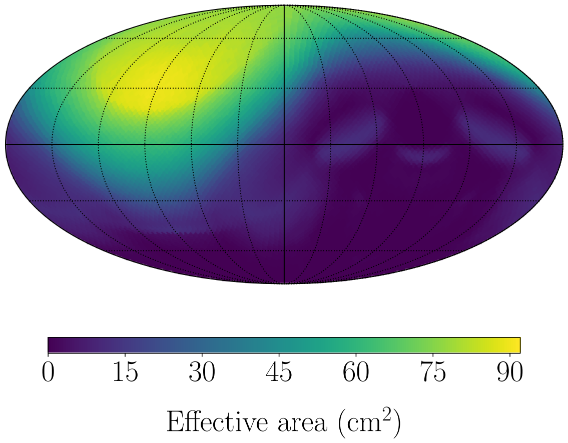

Figure 6.8. Effective area for gel pad in the polar position. Opening angle 20°.

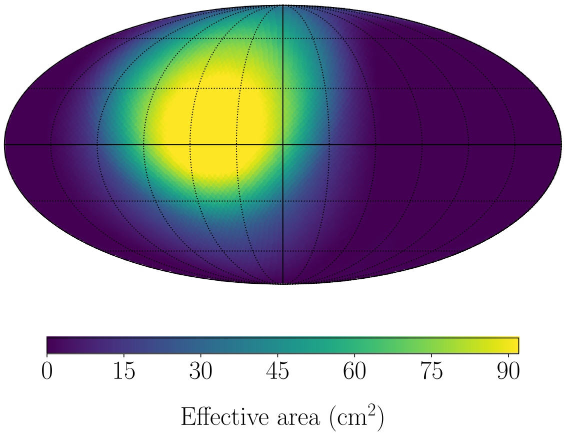

Figure 6.9. Effective area for reflector in the equatorial position. Opening angle 20°.

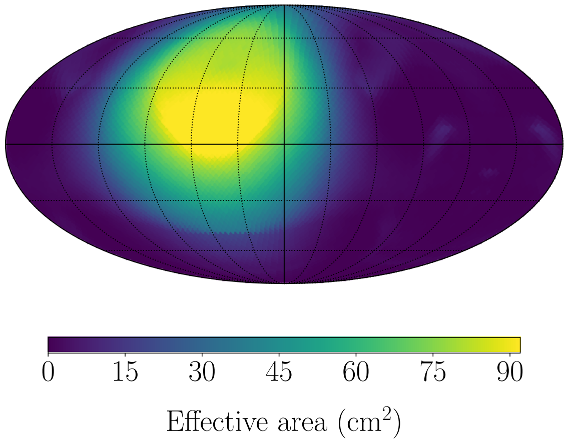

Figure 6.10. Effective area for gel pad in the equatorial position. Opening angle 20°.

The results for one polar PMT are shown in Figures 6.7 and 6.8 and for one equatorial PMTs are shown in Figures 6.9 and 6.10, both for the model with the holding structure and with gel pads respectively. These simulations correspond to an opening angle of 20 degrees.

For the PMTs in the polar position and the case with the holding structure, the zone behind the PMT has a number of detections close to zero. When a photon is thrown, this photon can not reach a photomultiplier placed on the opposite side of the module because there are reflectors and the holding structure is in the way.

However, for the module with the gel pads implemented, there is a pattern of detections on the opposite side of the PMT. It means that the photons can travel through the module and reach the contrary photomultiplier. Furthermore, in the figure, the patterns determines the optimal angles for this to happen.

The equatorial PMTs have the same behavior. The model with gel pads has a

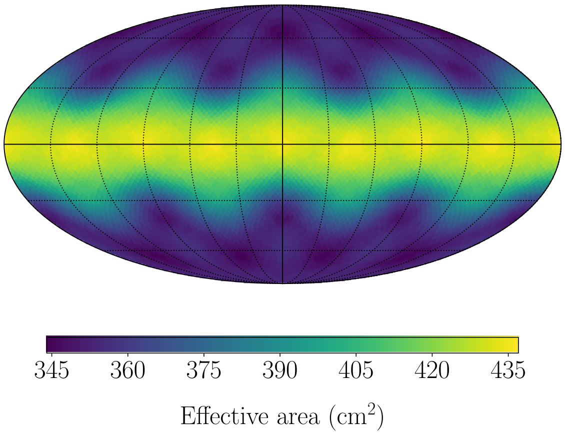

Figure 6.11. Effective area for the whole module with reflectors. Opening angle 20 degrees.

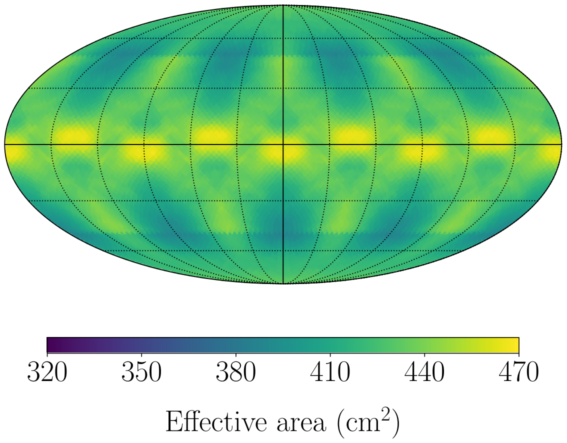

Figure 6.12. Effective area for the whole module with gel pads. Opening angle 20 degrees.

pattern on the opposite side of the photomultiplier which is not the case for the results with holding structure.

Another important difference is in the close zone to the PMTs. With reflectors, the boundary of the PMT is better defined and for gel pads, the pattern is softer. For both polar and equatorial PMTs, the diameter of the shadow of the detections is larger for gel pads than for reflectors. It is produced because the photocathode covers the boundary of the photocathode from some directions.

In Figures 6.11 and 6.12, the effective area for the whole module and for the two models respectively is depicted. It is apparent that the pattern for the whole module is the sum the effective area of the single PMTs positioned along the module.

Besides this, taking into account the scales in Figures 6.11 and 6.12, these plots show that both are fairly uniform. The standard deviation is 12% for the case with reflectors and at 19% for the case with gel pads.

To calculate the mean effective area, the effective area is integrated over theta and phi as Equations (4.2) and (4.3) indicate. However, it could be interesting to integrate only over one of these angles and showing the results as a function of the other one.

Integrating over theta and plotting the “mean effective area”[16] as a function of phi does not make too much sense due to the symmetry of the module. However, the integration over phi helps to have more information about the region with more detections and how they work.

To study this type of plots, the simulations can not be made using *healpy* because with *healpy*, the step of the theta angle is not the same for every value of phi and contrarily, i.e. integrate numerically over phi is not possible. Thus, for these plots the

---

[16] From now on, it will be called mean effective area even knowing that it is not exactly true because the integration is only over one angle.

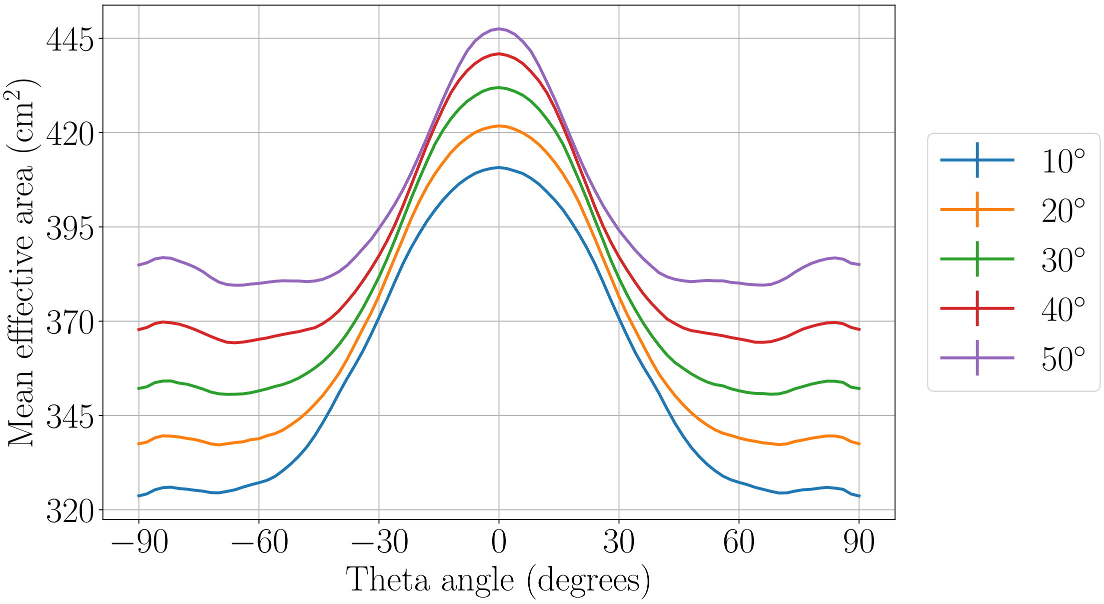

Figure 6.13. Integration over phi of the effective area with reflectors for several opening angles. The error bars are smaller than the width of the line.

simulations are run again but this time simulating linearly over theta instead of using *healpy*.

In Figure 6.13 the mean effective area integrating over phi is shown for the case with reflectors and for several opening angles. The module with the reflectors has more efficiency when the photons reach the module laterally, i.e. with the theta angle close to 0 degrees. Also, the mean effective area for any theta angle increases as the opening angle increases. This behavior is in line with Figure 6.4.

In Figure 6.14 the integration over phi is shown for gel pads. As a general feature, the mean effective area is larger for gel pads, which is in line with the earlier results. Furthermore, in this case, the trend of the curve is very different. For the lower values of the opening angles, (top plot in Figure 6.14) there is more efficiency in the equatorial zone. This means that when the photons come laterally, low values of the opening angles work better. However, in bottom plot in Figure 6.14, the behavior is totally different and there is more efficiency for the photons that originated in the polar positions.

With the model with gel pads, if there is a photon coming from a polar position, it does not mean that this photon will be detected by a PMT in the polar position because it could travel through the module. However, it is most likely that this does not happen.

Following this argument, Figure 6.14 shows that it could be a good idea to set up a different configuration for the polar PMTs and for the equatorial PMTs, i.e. to implement a different opening angle for equatorial and for polar reflectors. Doing that, the number of degrees of freedom in the simulations is duplicated.

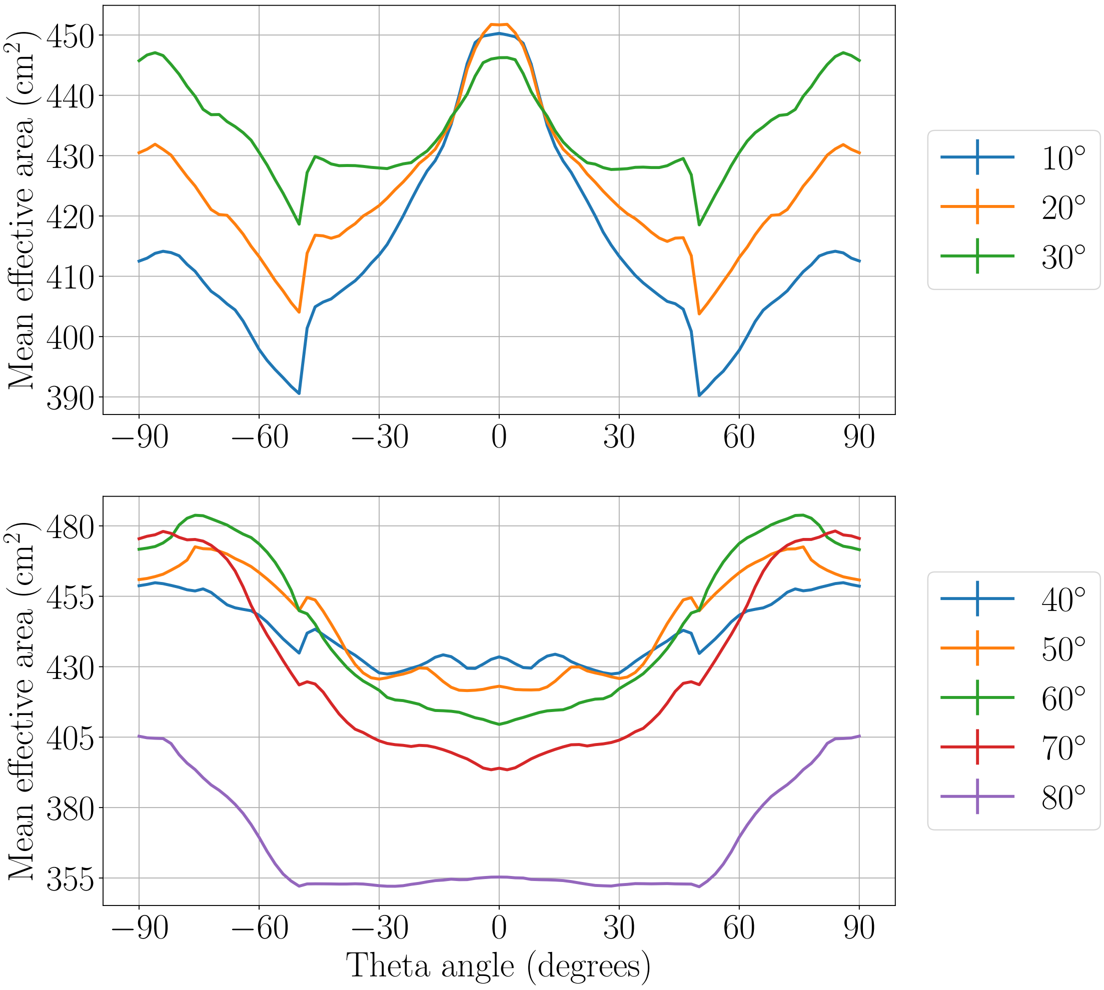

Figure 6.14. Integration over phi of the effective area with gel pads for several opening angles. Top plot shows the lower values of the opening angle and the mean effective area is larger for the equatorial PMTs. The bottom plot shows the larger values of the opening angle and the mean effective area is larger for the polar PMTs. The error bars are smaller than the width of the line.

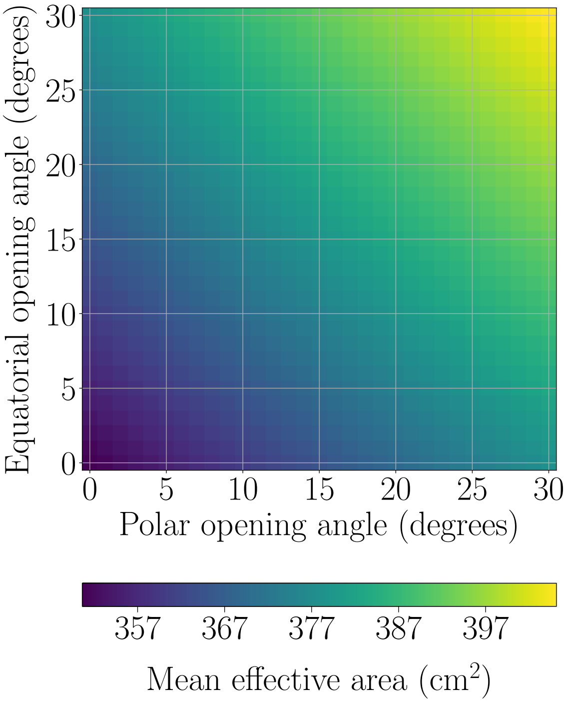

Figure 6.15. Mean effective area for the module with reflectors and different parameters for equatorial and polar PMTs.

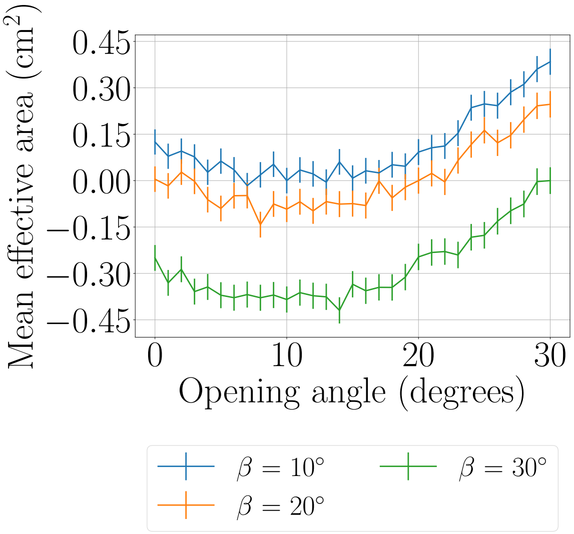

Figure 6.16. Difference between the mean effective area fixing the polar opening angle and sampling the equatorial opening angle, and fixing the equatorial opening angle and sampling the polar opening angle. The colors represent the value of the fixed opening angle.

From Figure 6.13, the case with reflectors does not lead to this rationale and it seems that the opening angles work similarly in any position. However, the optimization with independent angles for the polar and equatorial reflectors is also done for the reflectors, in order to ensure the best effective area.

Figure 6.15 shows the mean effective area for the case with holding structure and setting a different opening angle for polar PMTs and equatorial PMTs. It is not difficult to see that the behavior of both variables is basically the same. The mean effective area increases as both opening angle increase.

Figure 6.16 shows the difference between the mean effective area fixing the polar opening angle cycling the equatorial opening angle and fixing the equatorial opening angle and cycling the polar opening angle. The curves are so close to zero hence the opening angle polar and equatorial for the case with reflectors have the same influence over the mean effective area. This shows that for the module with the holding structure implemented, it does not make sense to set different opening angles for polar and equatorial PMTs. This result was expected looking at Figure 6.13.

The mean effective area for the case with gel pads is shown in Figure 6.17. The mean effective area falls quickly when opening angle for the equatorial PMTs overcomes

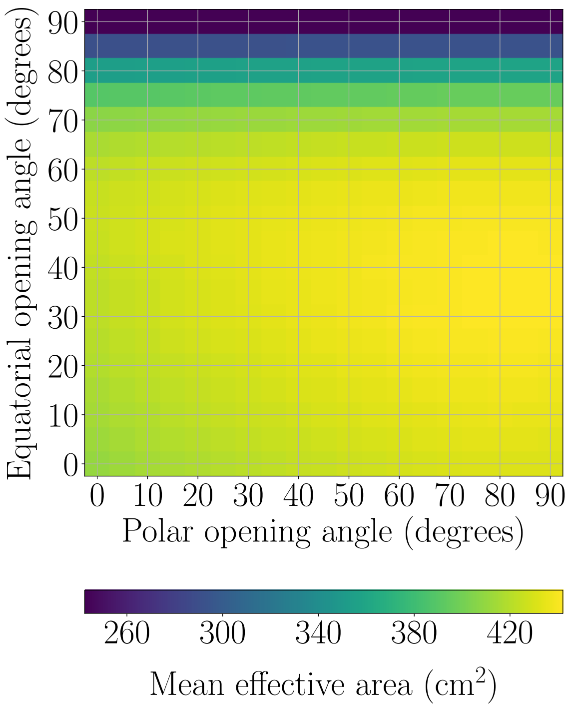

Figure 6.17. Mean effective area for the module with gel pads and different parameters for equatorial and polar PMTs.

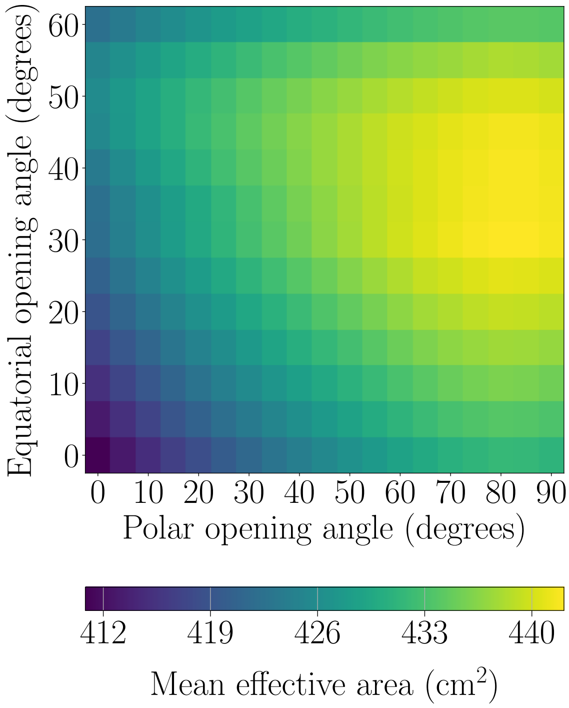

Figure 6.18. Zoom of the mean effective area for the module with gel pads and different parameters for equatorial and polar PMTs.

60-70 degrees.

In order to look better what is the best options for this model, Figure 6.18 shows the mean effective area for the module with gel pads with a zoom on the region of interest. The mean effective area increases with the opening angle for the polar PMTs. However, the mean effective area as a function of the equatorial opening angle features a maximum around 35-45 degrees. This result is also expected from Figure 6.14.

From these results, the values of the opening angles which optimize the mean effective area can be obtained. The uncertainty of these optimal opening angles stems from the size of the step used during the simulation, i.e. if the opening angle is sampled two by two degrees, the uncertainty is one degree. Thus, the uncertainty of the opening angle for the case with gel pads is larger than this uncertainty for the case with reflectors. This is because the case with gel pads has two variables while the case with reflector has just one, hence the simulations were run with a coarser step to keep a feasible simulation time.

In order to have a better resolution for the maximum, the simulation of the module with gel pads is run again but in a smaller parameter space with smaller steps. The results are shown in Figure 6.19.

Based on these simulations, the values of the opening angles which optimized the mean effective area for both models are shown in Table 6.1.

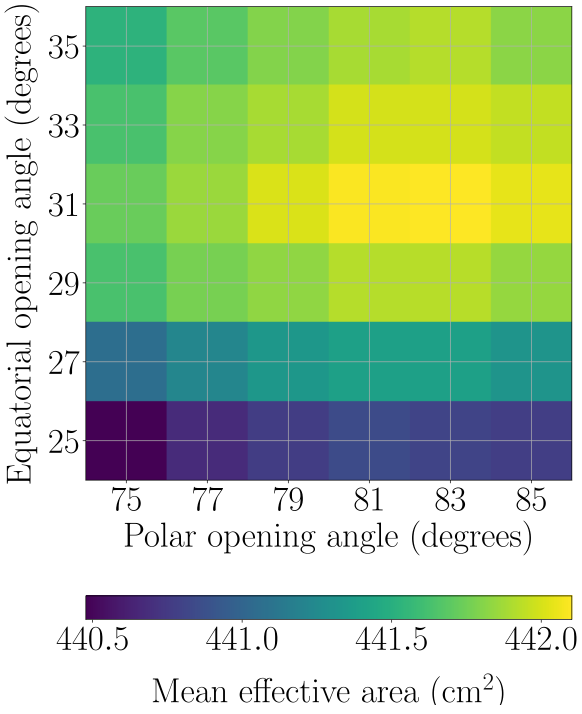

Figure 6.19. Mean effective area with the module with gel pads and different parameters for equatorial and polar PMTs with a better accuracy.

In principle, more simulation could be run to get a better accuracy for the maximum. However, the number of photons should be increased too with the goal of decreasing the uncertainty of the mean effective area because it is not possible to compare two values when the uncertainty is larger than the difference between them. This involves simulations with a much longer running time. For the framework of this thesis, this uncertainty is enough.

Table 6.1. The best parameters possible for the conical reflectors/gel pads.

	Reflectors	**Gel pads**
Equatorial opening angle (°)	30.0 ± 0.5	31 ± 1
Polar opening angle (°)	30.0 ± 0.5	83 ± 1
Mean effective area (cm^2)	405.14 ± 0.02	442.10 ± 0.02

From this results it is clear, that the model with gel pads provides around 10% more effective area than the design with reflectors.

6.4 Ellipsoidal reflective structures

In this section the optimization of the parameters relating to the ellipsoidal reflectors and gel pads is studied. In this case, there are two variables that define the shape of the ellipsoidal reflectors, the semi-axis a and b, hence the mean effective area is plotted as a function of both.

The range of both semi-axes for the case of the reflectors is limited by the maximum value that they can take without overlapping each others. The range of the semi-axis b is 53 - 58 mm and for the semi-axis a is 70 - 94 mm. For the gel pads there is no limitations, so the range of the semi-axis b is 55 - 150 mm and for the semi-axis a is 50 - 120 mm.

Figures 6.20 and 6.21 show the mean effective area for the cases with ellipsoidal reflectors and with ellipsoidal gel pads respectively.

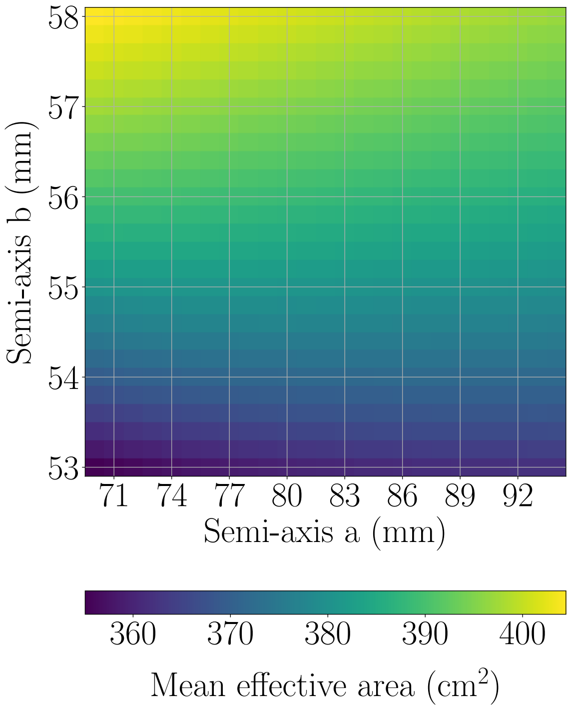

Figure 6.20. Mean effective area for reflectors as a function of both semi-axes.

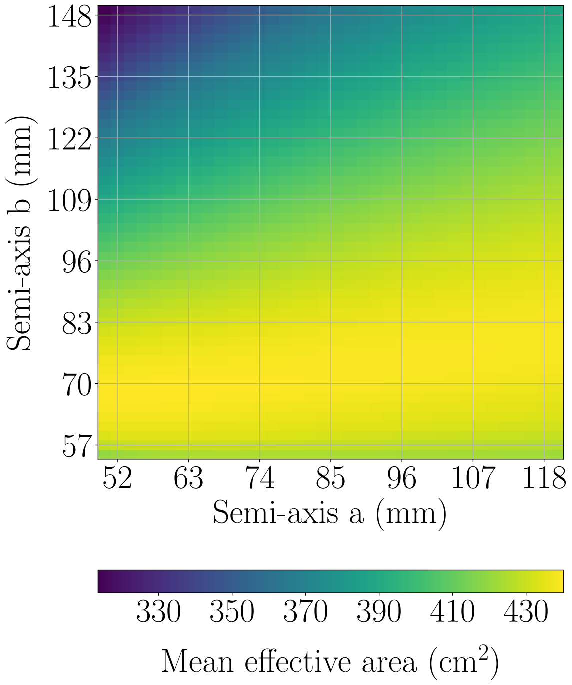

Figure 6.21. Mean effective area for gel pads as a function of both semi-axes.

In Figure 6.20, the mean effective area increases as the semi-axis b increases. However, the behavior related to the semi-axis a is different. For small semi-axis b the mean effective area increases with a and for large semi-axis b it falls with increasing a. In the zone for higher values for the mean effective area, low value of the semi-axis a provides better results. Actually, it makes sense because low values of the semi-axis b mean that the shape of the reflector is more “spherical” and it helps to reflect the photons towards the photocathode. A better representation of the trend of both semi-axes is shown in Figures 6.22 and 6.23, fixing the semi-axis a and b respectively.

Figure 6.21 shows the mean effective area as a function of both semi-axes for the case with gel pads. In this plot, the mean effective area gets very low when the semi-axis b increases and best results are provided for low values of this parameter. For the semi-axis a, the trend depends on the value of the semi-axis b, with a trend upward for high values of the semi-axis b and practically constant for low values of the semi-axis b.

Figures 6.24 and 6.25 show the trend of the mean effective area for the case with ellipsoidal gel pads as a function of the semi-axis a and b respectively. From these figures, the trend with respect to the semi-axis b is determined by the value of the semi-axis a, however, this semi-axis a affects less the mean effective area when the semi-axis b is fixed.

The simulations with the gel pads show a larger effective are than the case with reflectors. This can be observed in all the figures of this section so far, looking the scale of Figures 6.20 to 6.25. As happened with the conical reflective components, this difference seems to be determined by the capability of the photomultipliers with the gel pads implemented to detect a photon incoming from the contrary side of its position. To illustrate this phenomenon, the effective area for both cases and with different PMTs are compared, with a semi-axis b of 55 mm and a semi-axis a of 85 mm.

Figures 6.26 and 6.27 show the effective area of one PMT placed in the polar position with reflector and with gel pads, respectively. While the case with reflector only has detections on the side of the PMT for the PMT with ellipsoidal gel pads there are detections of photons from the contrary side of it. There is a pattern indicating the most favorable angles from which the photon go in to the module.

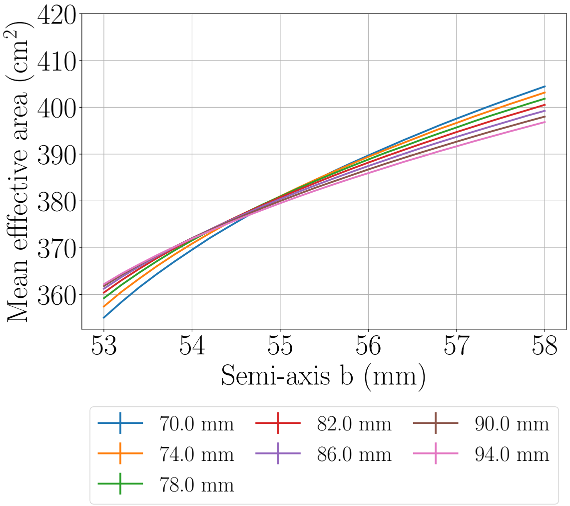

Figure 6.22. Mean effective area for ellipsoidal reflectors fixing the semi-axis a at different values shown in the legend.

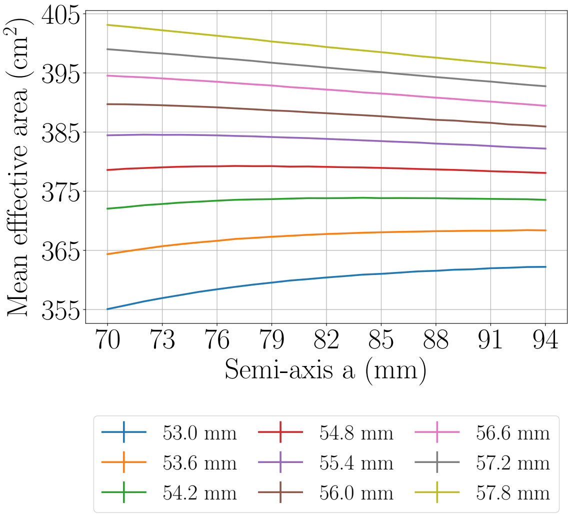

Figure 6.23. Mean effective area for ellipsoidal reflectors fixing the semi-axis b at different values shown in the legend.

In Figures 6.28 and 6.29, the effective area is shown but for one PMT placed in a equatorial position. These figures show the same phenomenon, having a pattern of detections in the contrary side of the PMT in the case with gel pads, which does not appear with holding structure. In this case, the pattern is not so intense as for the polar PMT. This can be because in the equatorial zone the spacing between PMT is smaller than for the polar PMTs. This fact makes difficult to the photons travel through the module.

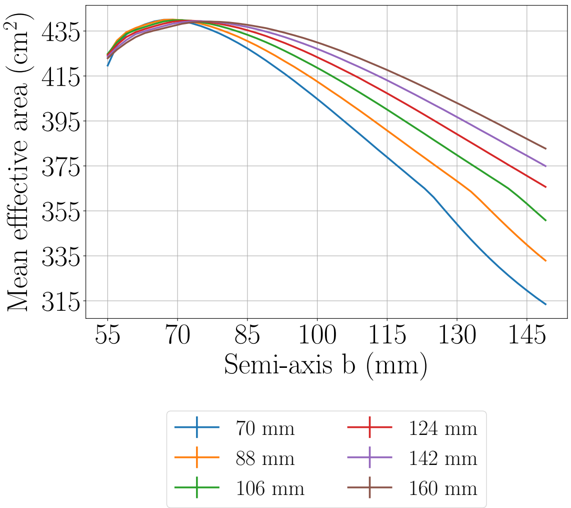

Figure 6.24. Mean effective area for ellipsoidal gel pads fixing the semi-axis a at different values shown in the legend.

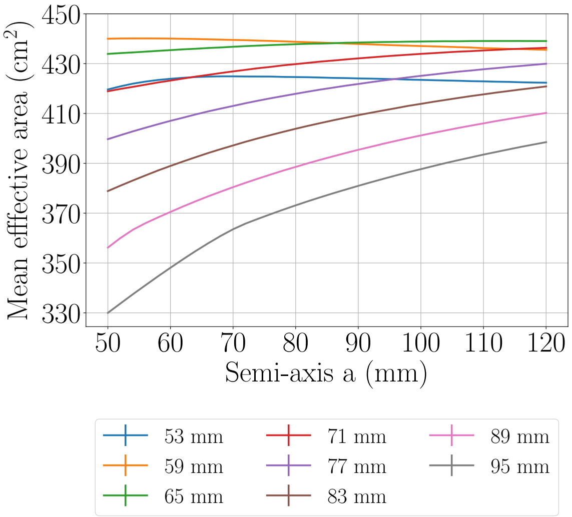

Figure 6.25. Mean effective area for ellipsoidal gel pads fixing the semi-axis b at different values shown in the legend.

As in the conical reflective components, the close zone to the PMT provides an important difference between reflectors and gel pads. The pattern of detections surrounding the PMT is larger for gel pads than for reflectors owing to the holding structure covering the boundary of the photocathode.

The effective area for the whole module is shown in Figures 6.30 and 6.31. It is very clear that the pattern shown for the polar PMT and to a lesser extend in the equatorial position, determine considerably the pattern of the whole module with gel pads.

Also, with the same scale in Figures 6.30 and 6.31 there is an huge difference, having the model with gel pads much better results. Although it is obvious that the model with gel pads offers larger benefits, this result are subject to the parameters chosen for the semi-axes. For another parameters, the difference does not have to be so abruptly.

In order to understand better the differences between both models, the mean effective is studied integrating over phi. For the conical reflective components, these plots can be shown for different opening angles but for the case with ellipsoidal ones, there are two variables to cycle. To solve this problem, the semi-axis a is fixed at 70 mm and the plots are shown varying the semi-axis b. The behavior for another values of the semi-axis a is the same and their plots can be found in Appendix B.

In Figure 6.32, the integration over phi for the case of the module with reflectors is shown. There is a larger efficiency when the photon reaches the module from the lateral side than when it reaches it from the poles. The behavior is similar for every semi-axis b and for every semi-axis a. Also, in general the mean effective area increases as the semi-axis b increases.

Figure 6.33 shows the same plot but for gel pads. In this case, it is better to separate

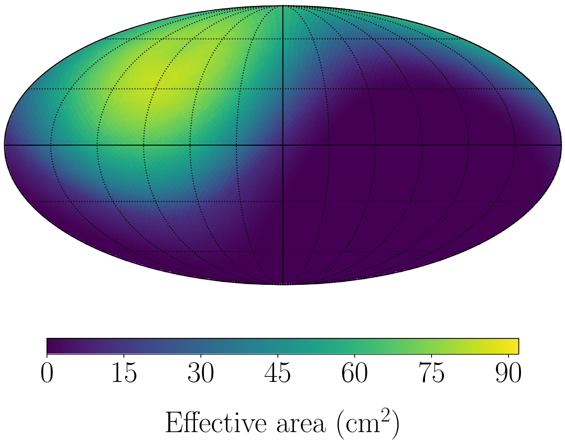

Figure 6.26. Effective area for reflector in the polar position. Semi-axis b 55 mm and semi-axis a 85 mm.

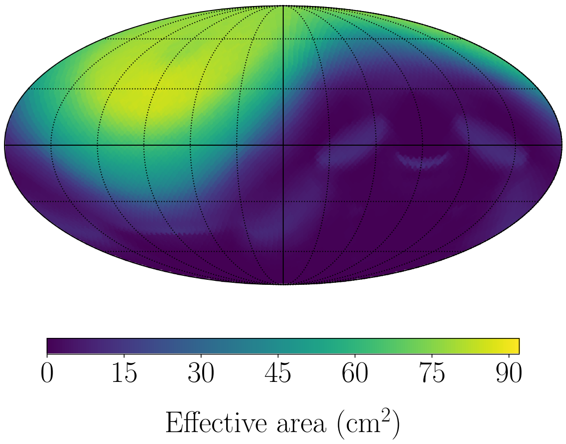

Figure 6.27. Effective area for gel pad in the polar position. Semi-axis b 55 mm and semi-axis a 85 mm.

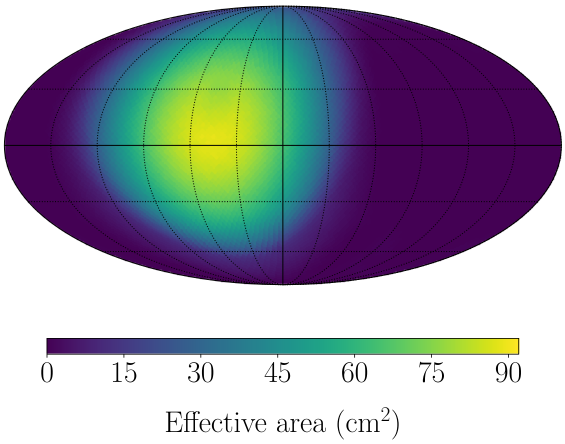

Figure 6.28. Effective area for reflector in the equatorial position. Semi-axis b 55 mm and semi-axis a 85 mm.

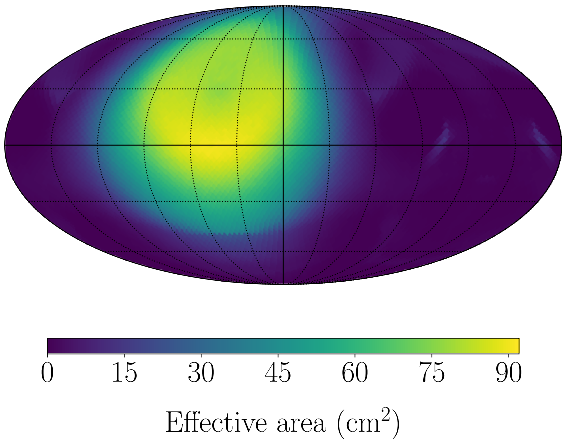

Figure 6.29. Effective area for gel pad in the equatorial position. Semi-axis b 55 mm and semi-axis a 85 mm.

the different semi-axis b in two behaviors. First, the low values of the semi-axis b works better when the photons area originated in the equatorial zone, while the large values for the semi-axis b make the PMTs placed in the polar positions more efficient.

As mentioned, if one photon has been detected by one PMT placed in the polar position, with the gel pads, this does not mean that the photons incoming from the polar position because it can travel through the module. Even so, the analysis from the two last paragraph makes sense because it is more likely that the photons do not travel through the module.

Following these results, it is obtained that to set up a different semi-axes for the polar and equatorial PMTs is a good idea in order to optimize the mean effective area. In principle, according to Figure 6.32, the model with reflectors and the holding structure presents the same behavior for polar and equatorial PMTs and it does not

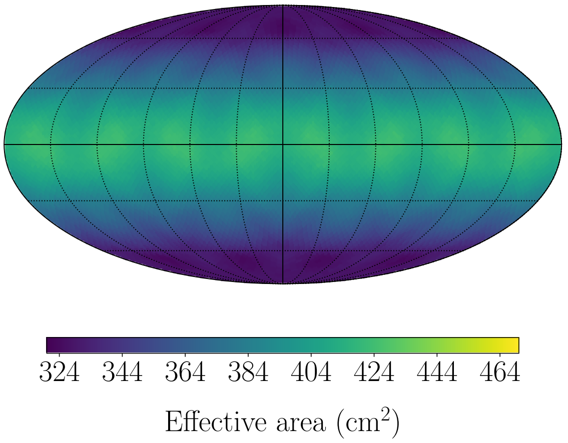

Figure 6.30. Effective area for the whole module with reflectors. Semi-axis b 55 mm and semi-axis a 85 mm.

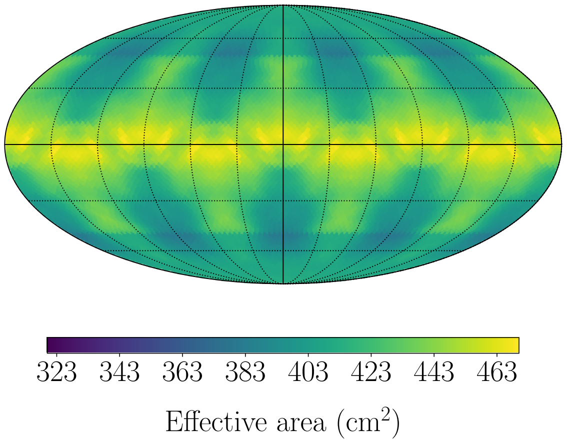

Figure 6.31. Effective area for the whole module with gel pads. Semi-axis b 55 mm and semi-axis a 85 mm.

need to implement different semi-axes for polar and equatorial PMTs. Nevertheless, the simulations are run to ensure the largest effective area.

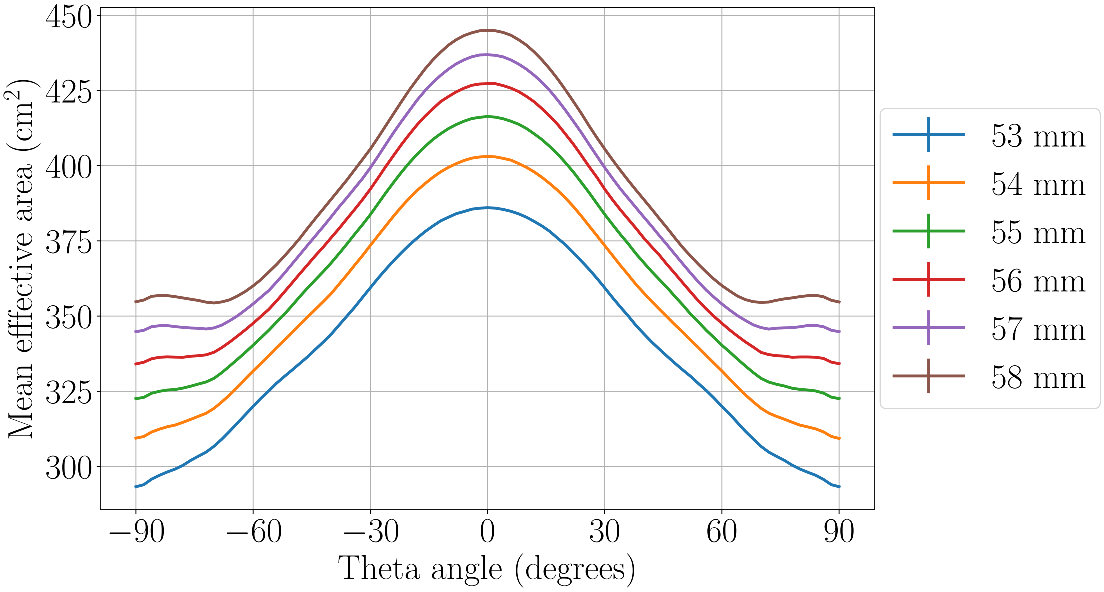

Figure 6.32. Integration over phi of the effective area with reflectors for several semi-axes minor, fixing the semi-axis a at 70 mm. The error bars are smaller than the width of the line.

If the different polar and equatorial semi-axes are deployed in the module, the simulations have four variables. For this reason, it is not possible to visualize the results in a plot. To solve this problem, on the one hand Figure 6.34 shows the mean effective area with ellipsoidal reflectors and the semi-axis a and b of the equatorial PMTs fixed at 80 mm and 85 mm respectively and Figure 6.35 shows the mean effective area with ellipsoidal reflectors and the semi-axis a and b of the polar PMTs fixed at 80 mm and 85 mm respectively. As it is known from Figure 6.30, the mean effective area increases

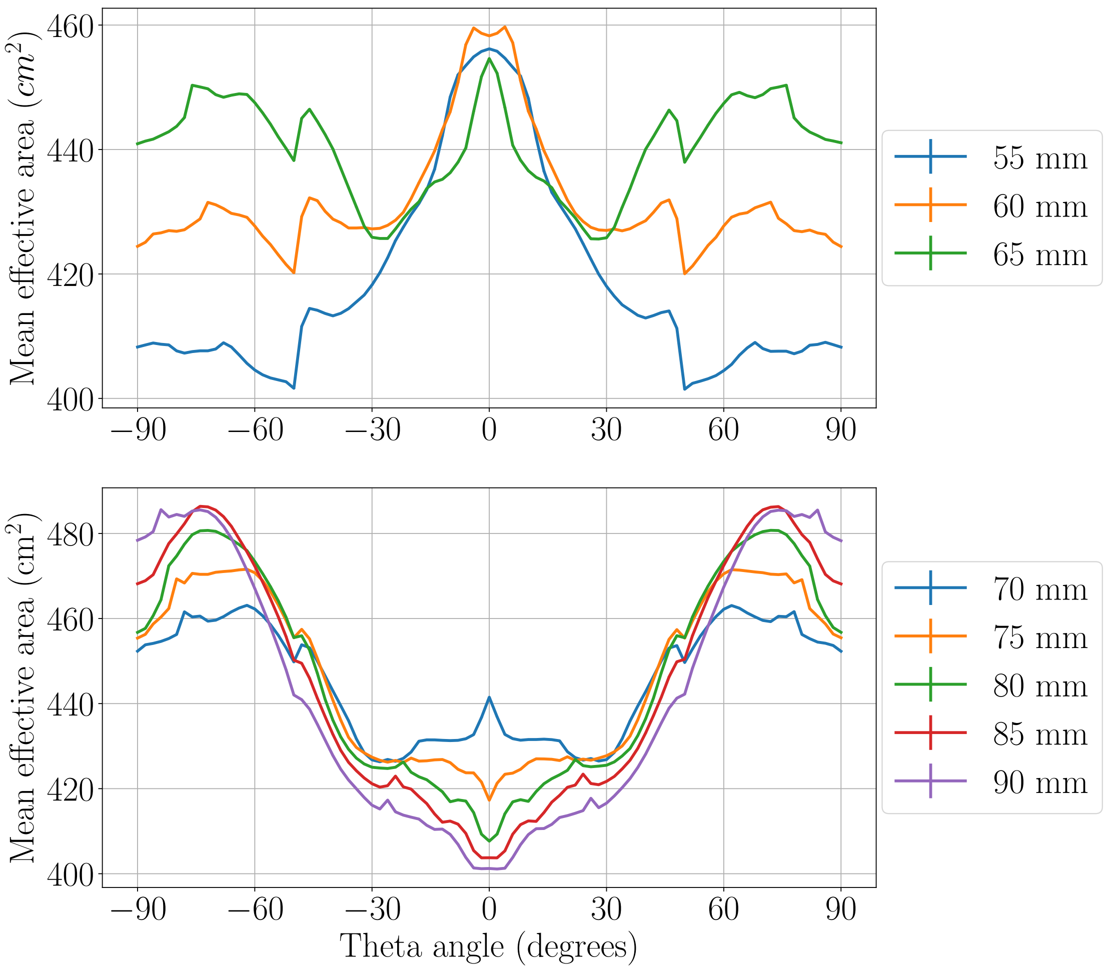

Figure 6.33. Integration over phi of the effective area with gel pads for several semi-axes minor fixing the semi-axis a at 70 mm. Top plot shows the lower values of the semi-axis b and the mean effective area is larger for the equatorial PMTs. The bottom plot shows the larger values of the semi-axis b and the mean effective area is larger for the polar PMTs. The error bars are smaller than the width of the line.

for large value of the semi-axis b and for low values of the semi-axis a in both cases. Also, the behavior for the polar PMTs and for the equatorial PMTs is the same, above all for high values of the mean effective area. In the Figure 6.36 is shown the difference between the mean effective area with reflectors and with gel pads and the values are close to zero. This means that it does not make sense to implement different semi-axes for polar and equatorial PMTs for the model with reflectors.

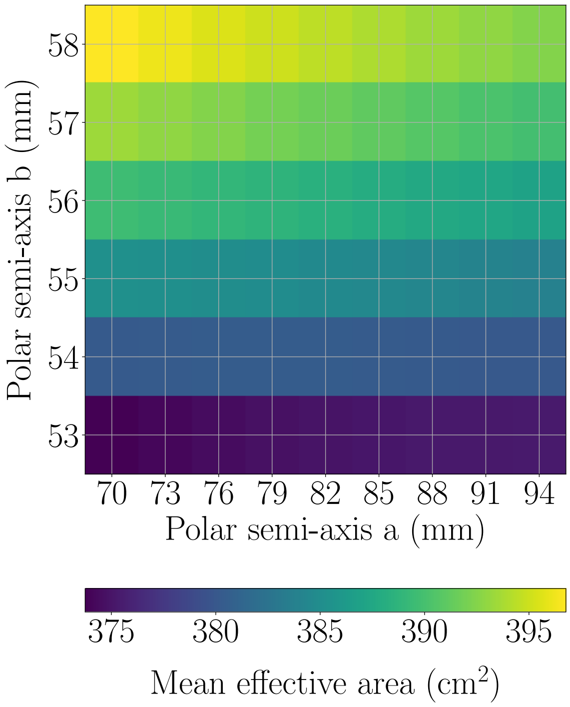

Figure 6.34. Mean effective area for ellipsoidal reflectors as a functions of the semi-axis b polar and semi-axis a polar. The semi-axis b equatorial fixed ar 85 mm and the semi-axis a equatorial at 80 mm.

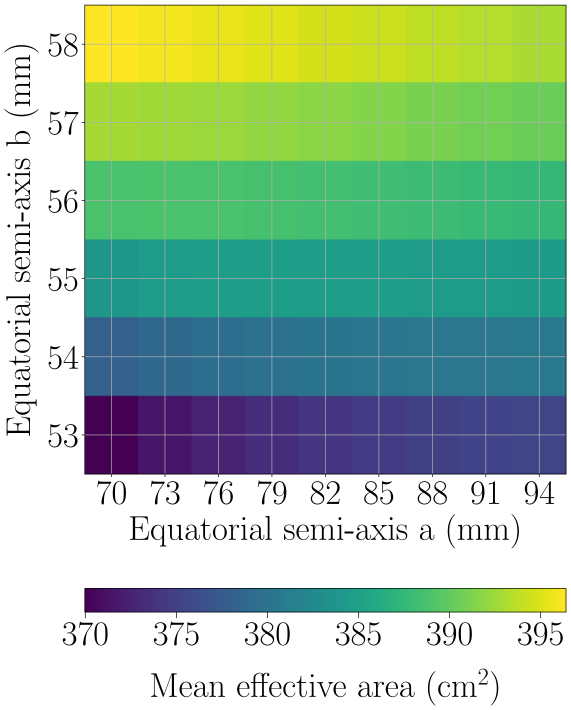

Figure 6.35. Mean effective area for ellipsoidal reflectors as a functions of the semi-axis b equatorial and semi-axis a equatorial. The semi-axis b polar fixed at 85 mm and the semi-axis a polar at 80 mm.

On the other hand, Figure 6.37 shows the mean effective area with ellipsoidal gel pads and the semi-axis a and b of the equatorial PMTs fixed at 80 mm and 85 mm respectively and Figure 6.38 shows the mean effective area with ellipsoidal gel pads and the semi-axis a and b of the polar PMTs fixed at 80 mm and 85 mm respectively. For the model with gel pads, the behavior of the semi-axes for polar and equatorial positions have a different trend. First, Figure 6.37 shows as the mean effective area increases as the semi-axis b increases and the semi-axis a decreases. This result is surprising because is totally opposite to the behavior found in Figure 6.31 when the same semi-axes were implemented for all PMTs. Furthermore, in Figure 6.38 the mean effective area increases as both semi-axes decrease.

With the goal of improving the uncertainty of the optimal parameters, two simulations with smaller stepping were done. Here, it will only be shown the result of the

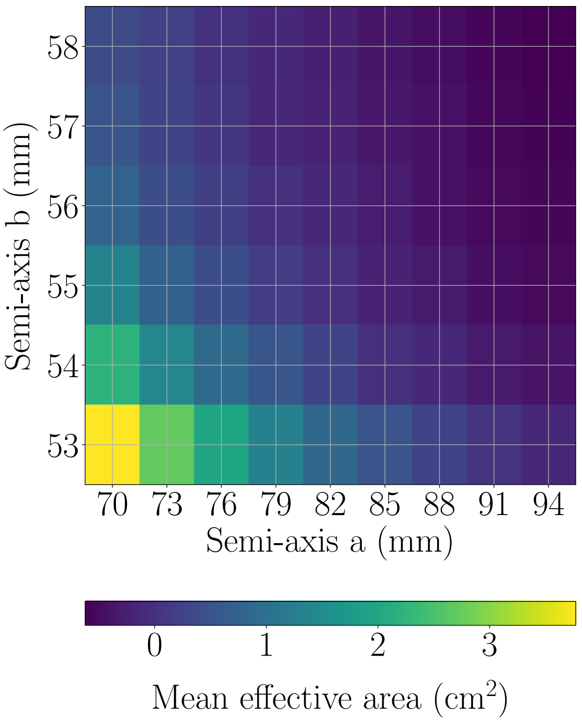

Figure 6.36. Difference between the mean effective area fixing the polar semi-axes a and b and fixing the equatorial semi-axes a and b at 80 mm and 85 mm respectively.

last simulations hence the intermediate one is the same but with a larger range and step.

Figures 6.39 and 6.40 show the result for the last simulation of the module with ellipsoidal gel pads, and with the range reduced to improve the accuracy of the optimal parameters.

In Figure 6.39 the mean effective area as a function of the polar semi-axis a and the polar semi-axis b is shown with the equatorial semi-axis a and b are fixed at their optimal parameters. Figure 6.40 shows the mean effective area as a function of the equatorial semi-axis a and the equatorial semi-axis b fixing the polar semi-axis a and the polar semi-axis b at their optimal parameters.

The best configuration of semi-axes corresponds to gel pads more wide in the polar position and gel pads more reduced in the equatorial position. This phenomena is related with the density of PMTs in each case. The density of PMTs in the polar region is smaller than in the equatorial zone, resulting in better results with wider gel pads at the polar position.

The final results for the optimal semi-axes both for the model with the holding structure and for the model with gel pads are shown in Table 6.2. The uncertainty of the variables stems from the size of the step used during the simulations.

As summary of the whole chapter, Figures 6.41 to 6.44 show the effective area for

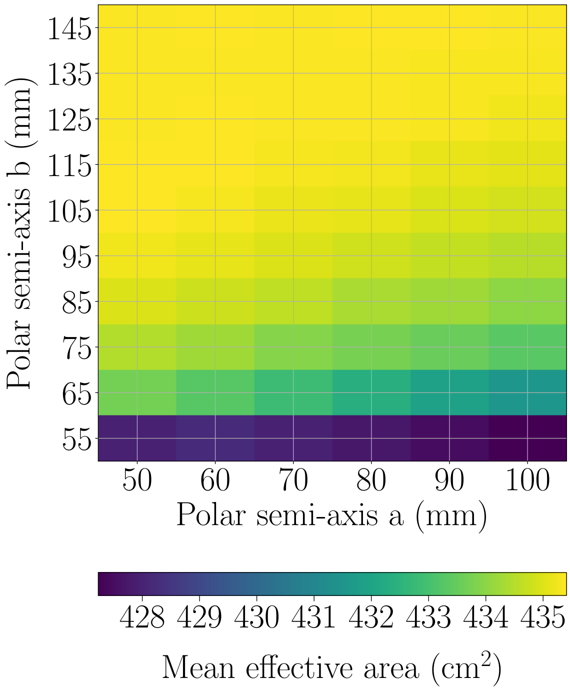

Figure 6.37. Mean effective area for ellipsoidal gel pads as a functions of the semi-axis b polar and semi-axis a polar. The semi-axis b equatorial fixed ar 85 mm and the semi-axis a equatorial at 80 mm.

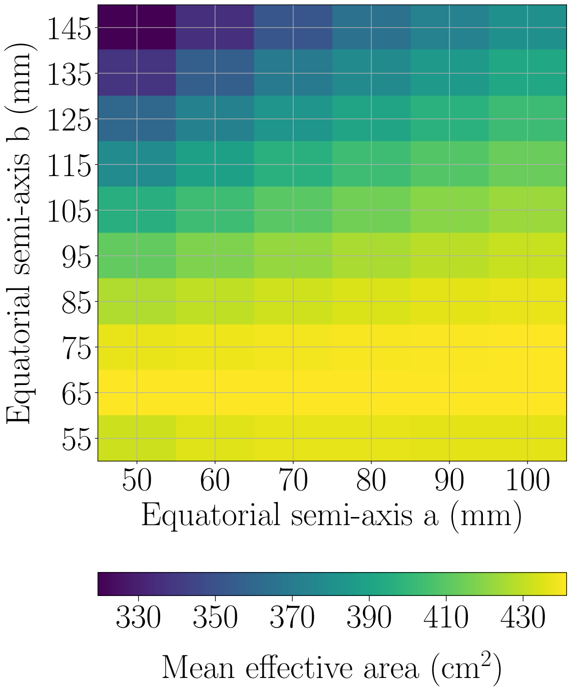

Figure 6.38. Mean effective area for ellipsoidal gel pads as a functions of the semi-axis b equatorial and semi-axis a equatorial. The semi-axis b polar fixed ar 85 mm and the semi-axis a polar at 80 mm.

Table 6.2. The optimal parameters for the ellipsoidal reflectors/gel pads.

	Reflectors	**Gel pads**
Equatorial emi-axis b (mm)	58.0 ± 0.5	61 ± 1
Equatorial semi-axis a (mm)	70.0 ± 1.5	64 ± 1
Polar semi-axis b (mm)	58.0 ± 0.5	135 ± 1
Polar semi-axis a (mm)	70.0 ± 1.5	54 ± 1
Mean effective area (cm^2)	404.43 ± 0.02	443.00 ± 0.02

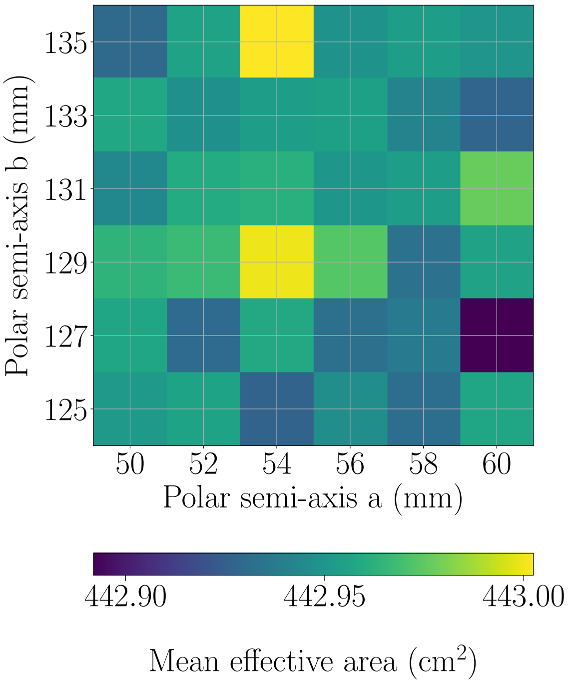

Figure 6.39. Mean effective area for ellipsoidal gel pads as a functions of the semi-axis b polar and semi-axis a polar with the range reduced. The semi-axis b equatorial and the semi-axis a equatorial fixed at their optimal values, 61 mm and 64 mm respectively.

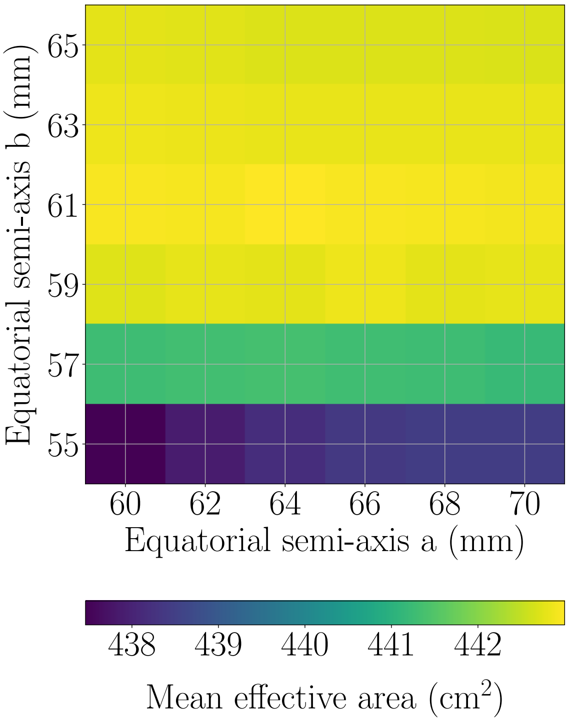

Figure 6.40. Mean effective area for ellipsoidal reflectors as a functions of the semi-axis b equatorial and semi-axis a equatorial with the range reduced. The semi-axis b polar and the semi-axis a polar fixed at their optimal values, 135 mm and 54 mm respectively.

all models with the optimal parameters. These plots allow to look that the ellipsoidal gel pads and the conical gel pads are really close in efficiency.

Concerning the reflectors, the model with conical reflectors has a larger effective area around the equatorial PMTs than the ellipsoidal reflectors model. However, the ellipsoidal reflectors provide an effective area more uniform across the solid angle.

In any case, in general the gel pads provide better results compared with the model with reflectors. Furthermore, the main difference between gel pads and reflectors are in the poles. This makes sense because, in the equatorial positions, the distance between the PMTs is shorter than for the PMTs in the polar position and there is more freedom to set up wider reflective structures. This behavior is in line with the general results obtained in this chapter, where the parameters of the PMTs placed in the polar position have more influence over the mean effective area than the parameters of the PMTs placed in the equatorial positions.

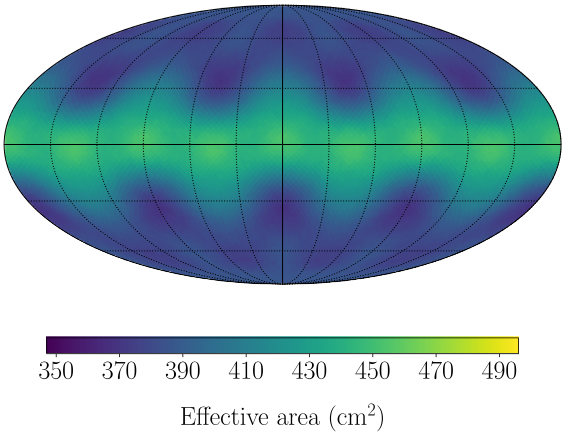

Figure 6.41. Effective area for the whole module with conical reflectors. Opening angle equatorial 30° and opening angle polar 30°.

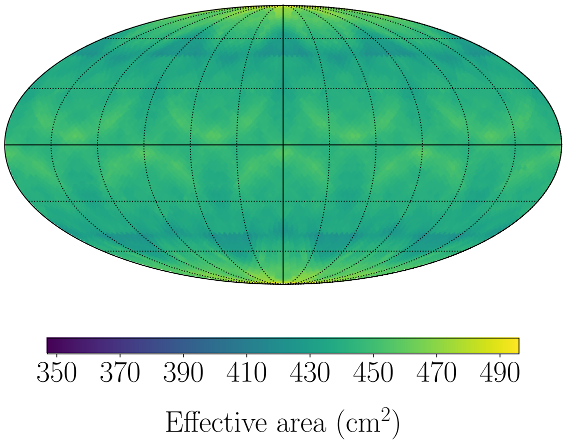

Figure 6.42. Effective area for the whole module with conical gel pads. Opening angle equatorial 31° and opening angle polar 83°.

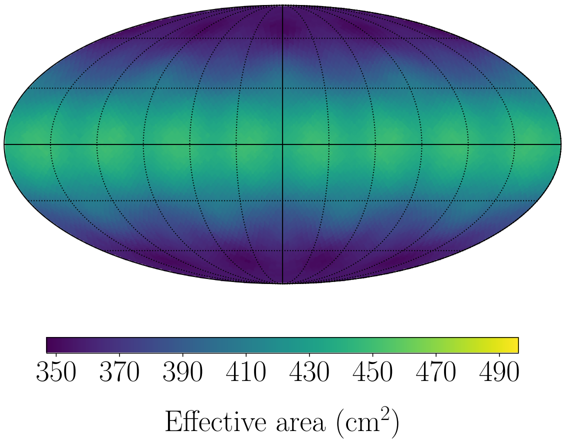

Figure 6.43. Effective area for the whole module with ellipsoidal reflectors. Semi-axis b equatorial 58 mm, semi-axis b polar 58 mm, semi-axis a equatorial 70 mm and semi-axis a polar 70 mm.

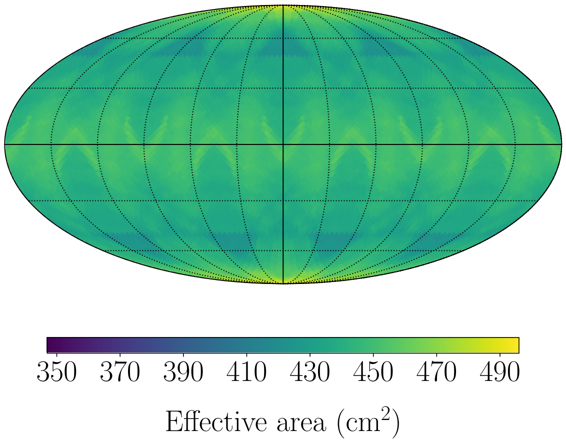

Figure 6.44. Effective area for the whole module with ellipsoidal gel pads. Semi-axis b equatorial 61 mm, semi-axis b polar 135 mm, semi-axis a equatorial 64 mm and semi-axis a polar 54 mm.

7 Summary and outlook

In this thesis, the optimization of the reflective components which will be implemented in the module LOM has been discussed using Geant4 simulations. For this purpose, there are two different kind of reflective components: reflectors or gel pads. In this thesis two shapes for this surfaces were studied, a conical shape, parameterized by one variable, and a elliptical shape, parameterized by two variables.

In Chapter 5, the behavior of the four designs was tested simulating a single PMT with the respective reflective structure implemented. This helped to understand how the parameters of each design affect the efficiency of the reflector and gel pads.

The mean effective area for the conical reflector has a maximum around 50 degrees while the mean effective area with conical gel pads has another maximum around 60 degrees and it drops abruptly after the peak. Also, the best value for the conical gel pads is 21% larger than the best value for the conical reflector.

On the other hand, the mean effective area for ellipsoidal gel pads presents a maximum for the semi-axis b around 80 mm but the dependence with the semi-axis a does not present a well-defined peak. The mean effective area with ellipsoidal reflector increases as both semi-axes increase. For ellipsoidal reflective components, the larger mean effective area for the best case of the ellipsoidal gel pads is 22% larger than for the ellipsoidal reflector.

These simulations allowed to constraint the parameter space for the detailed simulation with the complete module.

Secondly, to optimize the efficiency of the whole module with the different reflectors and gel pads, the designs was implemented in the module. From these simulations, a set of optimal parameters for the shape of the reflective components was found for the LOM.

Table 7.1 shows a summary of the optimal parameters for each design and its respective mean effective area. Besides to provide the optimal parameters, this table allows to compare all the design from its optimal parameters, i.e. it is possible to get the best options for the module. From the table, it can be extracted that the largest effective area of $(443.00 \pm 0.02)\, cm^2$ is achieved by the LOM with ellipsoidal gel pads.

As mentioned several times, the main advantage of the gel pads over the metallic reflectors is that these devices allow the photons travel through the module and hence some photons which would be missed with the model of reflectors, can be detected. Also, the holding structure shadow the boundary of the photocathode from some directions. These are the most important reasons which, in general, gel pads are better options than the reflectors.

It is important to indicate that in this thesis, the study according to the hardware and the process needed to build the gel pads and reflectors was not discussed. That

Table 7.1. Summary of the optimal parameters for each module and its respective mean effective area.

	Conical		**Ellipsoidal**		
	Reflectors	**Gel pads**	**Reflectors**	**Gel pads**	
Equatorial opening angle (degrees)	30.0 ± 0.5	31 ± 1	58.0 ± 0.5	61 ± 1	**Equatorial semi-axis** b (mm)
			70.0 ± 1.5	64 ± 1	**Equatorial semi-axis** a (mm)
Polar opening angle (degrees)	30.0 ± 0.5	83 ± 1	58.0 ± 0.5	135 ± 1	**Polar semi-axis** b (mm)
			70.0 ± 1.5	54 ± 1	**Polar semi-axis** a (mm)
Mean effective area (±0.02) cm^2	405.14	442.10	404.43	443.00	**Mean effective area** (±0.02) cm^2

is of particular importance, taking into account that it has been assumed that the gel pads can overlap with another gel pads. In any event, the range of values where it does not happen is also provided in this thesis.

The LOM is not studied in detail yet and there are several very exciting studies to be done. First, the simulations of this thesis can be done again using a different parameterization to define the shape of the reflective components, above all for the case of the ellipsoidal reflective components where others Winston cone geometries can be considered [37]. Also, different wavelengths (and hence, the quantum efficiency) could be included in the study to get information about the influence of this parameter in the module.

Secondly, with the model with gel pads, the PMTs can detect photons originated in the opposite direction where they are placed in the module and this affects the intrinsic directional sensitivity of the module. Thus, this intrinsic directional sensitivity should be studied in order to know the difference between reflectors (and holding structure) and gel pads in this aspect.

Thirdly, the module can be simulated taking into account the electronic elements which should be deployed inside it. Along this thesis, the results indicate that there is an improvement of 10% of the mean effective area if the module has the gel pads implemented instead of the reflectors. This is subject to the photons can travel through the module but the electronic elements can affect and reduce the capability of the photons of going through the pressure vessel.

A Distribution of the PMTs

This appendix provides the information about the position and orientation of each PMTs inside the module. Four variables are needed to place them in its exact position. Two of them correspond to its orientation and another two define its position. Table A.1 shows the values used during this thesis.

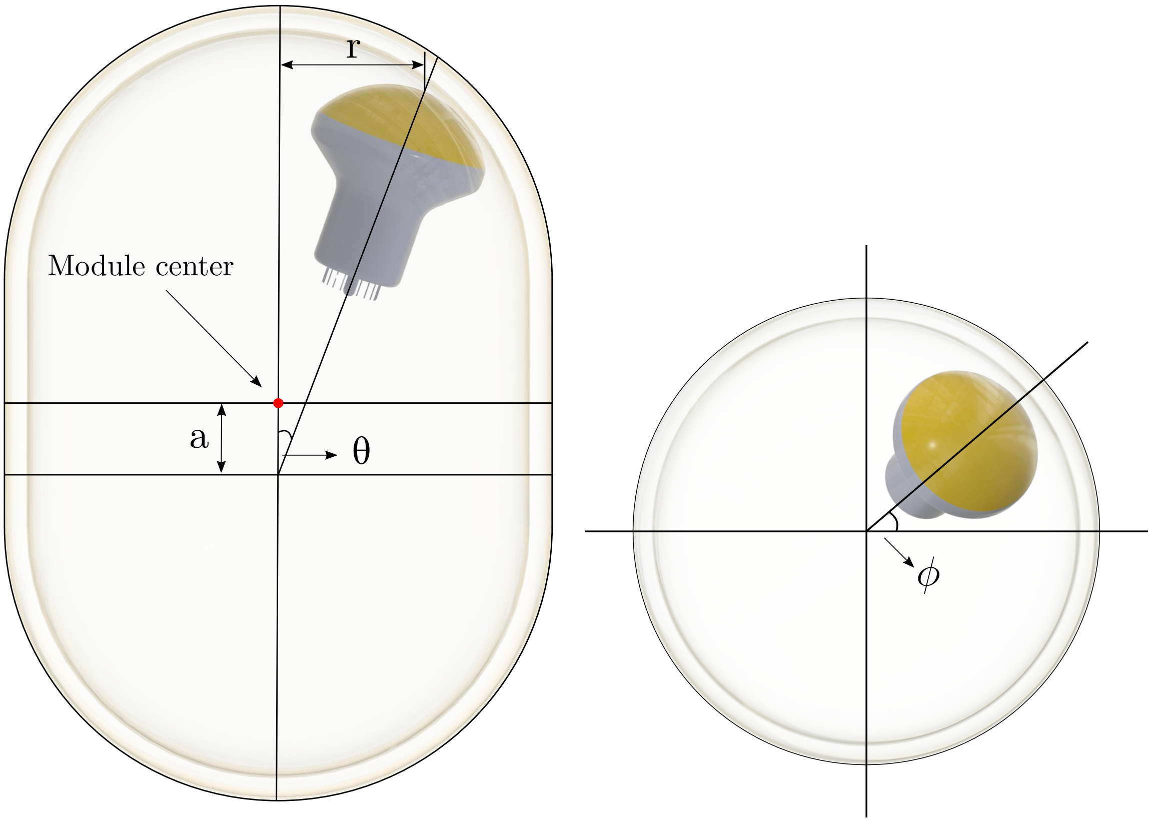

(a) Front view.

(b) Top view.

Figure A.1. Necessary measurements to place the PMTs inside of the module.

PMT	**r**	θ	ϕ	**a**
1	99.23	35	0	21.5
2	99.23	35	90	21.5
3	99.23	35	180	21.5
4	99.23	35	270	21.5
5	129.16	57	0	-0.7
6	129.16	57	90	-0.7
7	129.16	57	180	-0.7
8	129.16	57	270	-0.7
9	99.23	123	0	0.7
10	99.23	123	90	0.7
11	99.23	123	180	0.7
12	99.23	123	270	0.7
13	129.16	145	0	-21.5
14	129.16	145	90	-21.5
15	129.16	145	180	-21.5
16	129.16	145	270	-21.5

Table A.1. Position and orientation of the PMTs for the module LOM. The distances **r** and **a** are given in mm [mm] and the angles θ and ϕ in degrees.

B Extra plots

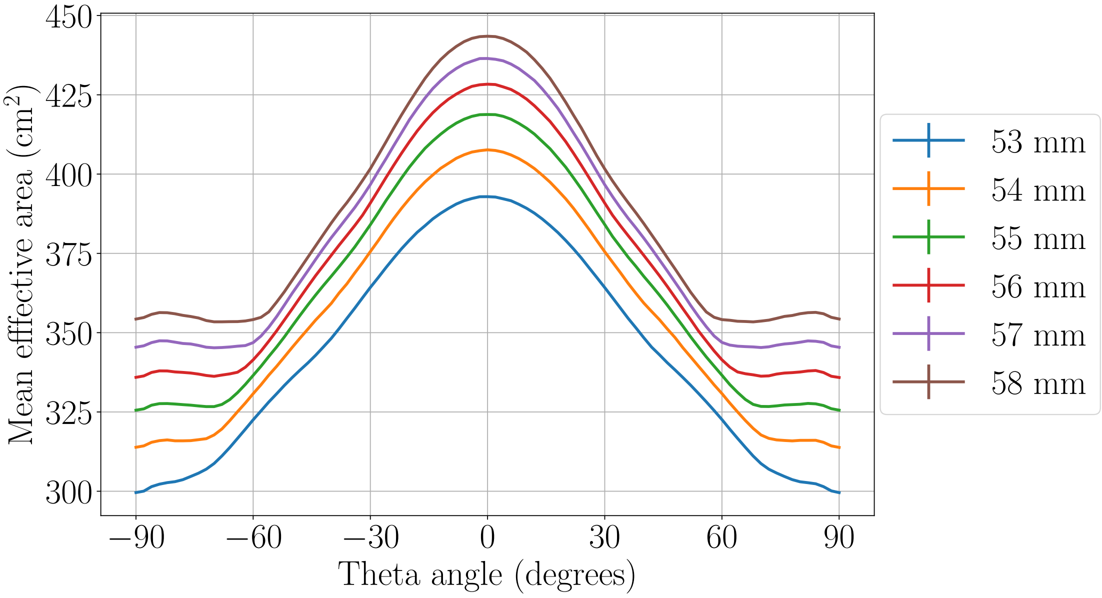

Figure B.1. Integration over phi of the effective area with reflectors for several semi-axes minor, fixing the semi-axis a at 80 mm. The error bars are smaller than the marker size.

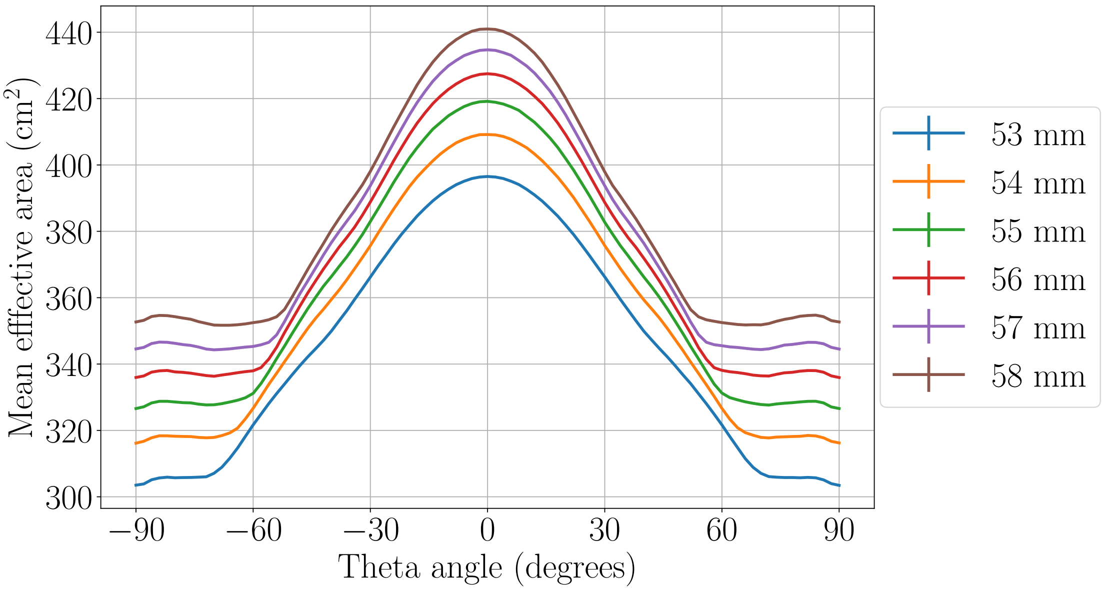

Figure B.2. Integration over phi of the effective area with reflectors for several semi-axes minor, fixing the semi-axis a at 90 mm. The error bars are smaller than the marker size.

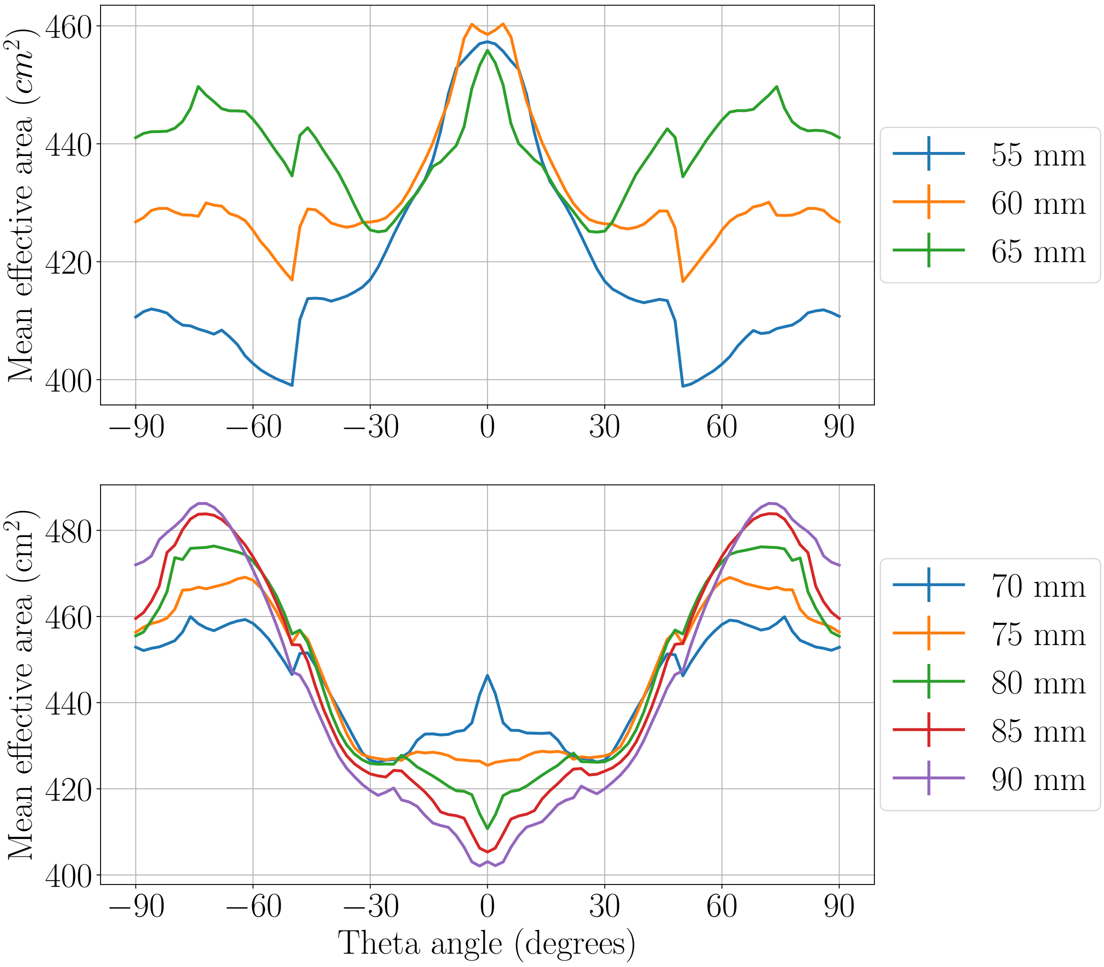

Figure B.3. Integration over phi of the effective area with gel pads for several semi-axes minor fixing the semi-axis a at 80 mm. Two different behaviors are separated in two plots. The error bars are smaller than the marker size.

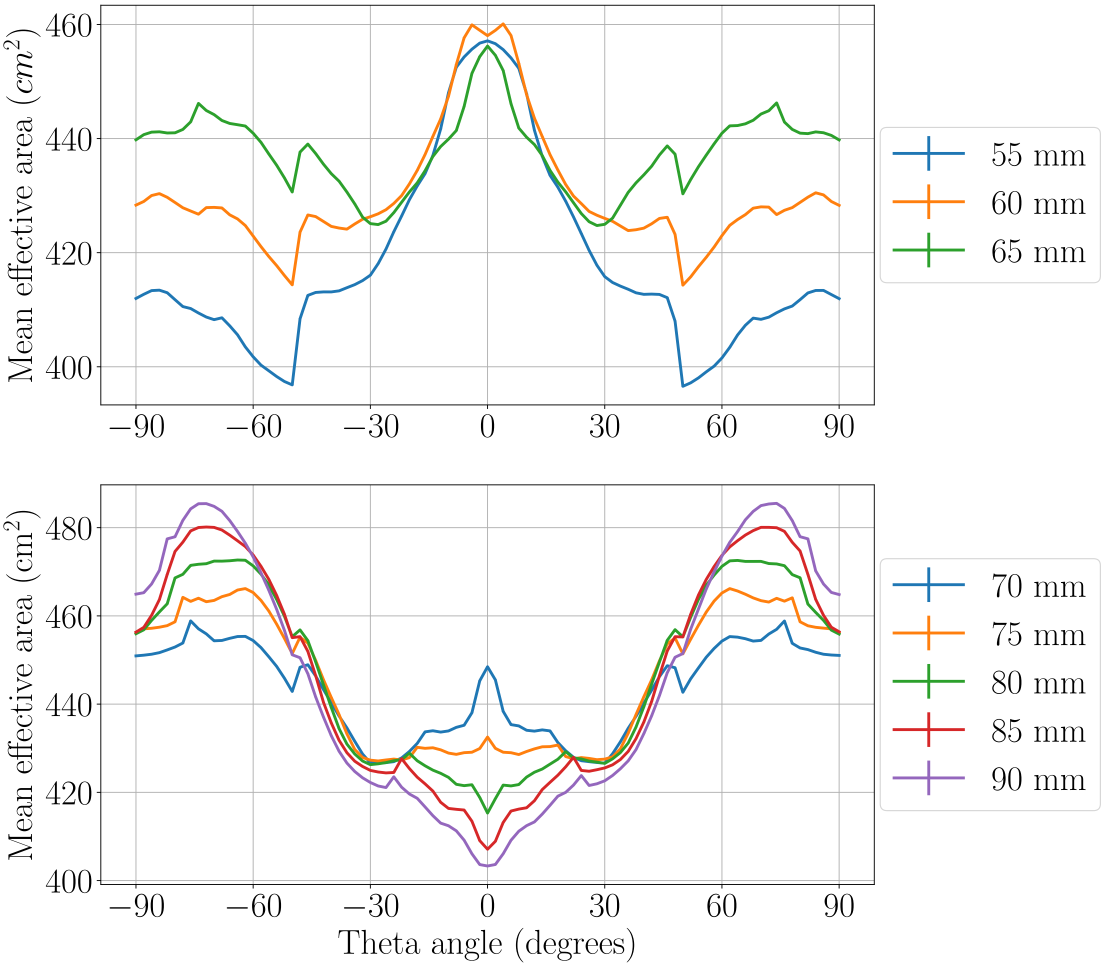

Figure B.4. Integration over phi of the effective area with gel pads for several semi-axes minor fixing the semi-axis a at 90 mm. Two different behaviors are separated in two plots. The error bars are smaller than the marker size.

List of Figures

2.1 Elementary particles of the Standard Model. Colored backgrounds provide information about which particles can be affected by each interaction. 4

2.2 Neutrino fluxes for different sources like the cosmological background radiation, the sun, supernovae and the Earth atmosphere. 5

2.3 Air shower produced when cosmic rays enter the Earth atmosphere. . . 6

2.4 A sketch of an active galactic nuclei (AGN) accelerating particles and producing high energy neutrinos. 7

2.5 Sketch of Cherenkov radiation. 9

3.1 Digital optical module implemented currently in IceCube. 11

3.2 Sketch of IceCube Neutrino Observatory. 12

3.3 Signatures left at the detector by the different flavours neutrinos when they interacts by means of the charged current. 13

3.5 Sketch of the IceCube Upgrade viewed from above. 15

3.4 Dual optical sensor in an Ellipsoid Glass for Gen2 (D-Egg). A digital optical module designed for IceCube Upgrade. 15

3.6 Sketch of IceCube-Gen2. 16

3.7 Sketch with the size, the design, and the components which form the Multi-photomultiplier Digital Optical Module (mDOM). 18

3.8 Sketch with main features of a photomultiplier tube. 19

3.9 Distribution of the elements of the digital optical module LOM. 20

3.10 An example of reflectors surfaces implemented in the PMTs. 21

3.11 Different possible designs for the reflective surface in the module LOM. 22

3.12 Illustration of the shape of the gel pads and its implementation with the pressure vessel. 23

4.1 Dimensions of the 4” photomultiplier Hamamatsu which is in development phase. 26

4.2 Fit of the photocathode surface. 27

4.3 Module LOM built in Geant4 without the holding structure. 27

4.4 The LOM without reflectors built in Geant4. 28

4.5 The building of the reflective cone with Geant4. 29

4.6 The conical reflectors for different opening angles β. 30

4.7 The building of the ellipsoidal reflectors with Geant4. 31

4.8 The behavior of the ellipsoidal reflectors when semi-axis b varies. 31

4.9 The ellipsoidal reflectors when semi-axis a varies. 32

4.10 Complete module LOM with holding structure model using conical reflectors. 32

4.11 Complete module LOM with gel pads model using ellipsoidal gel pads. 33

4.12 Distributions of pixels of HEALPix. 36
5.1 Sketch of the simulations with only one PMT. 37
5.2 Effective area for one PMT with reflectors as a function of the angle theta and of the opening angle. 38
5.3 Effective area for one PMT with gel pads as a function of the angle theta and of the opening angle. 38
5.4 Effective area for one PMT with reflectors as a function of the angle theta. 39
5.5 Effective area for one PMT with gel pads as a function of the angle theta. 39
5.6 Mean effective area as a function of the opening angle for reflectors and for gel pads. The error bar are smaller than the marker size. 40
5.7 Mean effective area for reflectors as a function of both semi-axes. 41
5.8 Mean effective area for gel pads as a function of both semi-axes. 41
5.9 Effective area for reflector as a function of the semi-axis b and the theta angle. Semi-axis a fixed at 86 mm. 41
5.10 Effective area for gel pads as a function of the semi-axis b and the theta angle. Semi-axis a fixed at 86 mm. 41
5.11 Effective area for reflector as a function of the semi-axis a and the theta angle. Semi-axis minor in 91 mm. 42
5.12 Effective area for gel pads as a function of the semi-axis a and the theta angle. Semi-axis b in 91 mm. 42
6.1 Example of a simulations with the whole module. 43
6.2 Frame of references used for the LOM. 43
6.3 Effective area for the LOM with reflectors with an opening angle of 30°. 44
6.4 Mean effective area as a function of the opening angle with the module with the holding structure. 46
6.5 Mean effective area as a function of the opening angle with the module with the gel pads. 46
6.6 Sketch of the LOM showing the equatorial and polar PMTs. 46
6.7 Effective area for reflector in the polar position. Opening angle 20°. . . 47
6.8 Effective area for gel pad in the polar position. Opening angle 20°. . . . 47
6.9 Effective area for reflector in the equatorial position. Opening angle 20°. 47
6.10 Effective area for gel pad in the equatorial position. Opening angle 20°. 47
6.11 Effective area for the whole module with reflectors. Opening angle 20 degrees. 48
6.12 Effective area for the whole module with gel pads. Opening angle 20 degrees. 48
6.13 Integration over phi of the effective area with reflectors for several opening angles. 49

6.14 Integration over phi of the effective area with gel pads for several opening angles. 50
6.15 Mean effective area for the module with reflectors and different parameters for equatorial and polar PMTs. 51
6.16 Difference between the mean effective area fixing the polar opening angle and mean effective area fixing the equatorial opening angle at different values. 51
6.17 Mean effective area for the module with gel pads and different parameters for equatorial and polar PMTs. 52
6.18 Zoom of the mean effective area for the module with gel pads and different parameters for equatorial and polar PMTs. 52
6.19 Mean effective area with the module with gel pads and different parameters for equatorial and polar PMTs with a better accuracy. 53
6.20 Mean effective area for reflectors as a function of both semi-axes. 54
6.21 Mean effective area for gel pads as a function of both semi-axes. 54
6.22 Mean effective area for ellipsoidal reflectors fixing the semi-axis a at different values. 55
6.23 Mean effective area for ellipsoidal reflectors fixing the semi-axis b at different values. 55
6.24 Mean effective area for ellipsoidal gel pads fixing the semi-axis a at different values. 56
6.25 Mean effective area for ellipsoidal gel pads fixing the semi-axis b at different values. 56
6.26 Effective area for reflector in the polar position. Semi-axis b 55 mm and semi-axis a 85 mm. 57
6.27 Effective area for gel pad in the polar position. Semi-axis b 55 mm and semi-axis a 85 mm. 57
6.28 Effective area for reflector in the equatorial position. Semi-axis b 55 mm and semi-axis a 85 mm. 57
6.29 Effective area for gel pad in the equatorial position. Semi-axis b 55 mm and semi-axis a 85 mm. 57
6.30 Effective area for the whole module with reflectors. Semi-axis b 55 mm and semi-axis a 85 mm. 58
6.31 Effective area for the whole module with gel pads. Semi-axis b 55 mm and semi-axis a 85 mm. 58
6.32 Integration over phi of the effective area with reflectors for several semi-axes minor, fixing the semi-axis a at 70 mm. 58
6.33 Integration over phi of the effective area with gel pads for several semi-axes minor fixing the semi-axis a at 70 mm. 59

6.34 Mean effective area for ellipsoidal reflectors as a functions of the semi-axis b polar and semi-axis a polar. The semi-axis b equatorial fixed ar 85 mm and the semi-axis a equatorial at 80 mm. 60

6.35 Mean effective area for ellipsoidal reflectors as a functions of the semi-axis b equatorial and semi-axis a equatorial. The semi-axis b polar fixed at 85 mm and the semi-axis a polar at 80 mm. 60

6.36 Difference between the mean effective area fixing the polar semi-axes a and b and fixing the equatorial semi-axes a and b at 80 mm and 85 mm respectively. 61

6.37 Mean effective area for ellipsoidal gel pads as a functions of the semi-axis b polar and semi-axis a polar. The semi-axis b equatorial fixed ar 85 mm and the semi-axis a equatorial at 80 mm. 62

6.38 Mean effective area for ellipsoidal gel pads as a functions of the semi-axis b equatorial and semi-axis a equatorial. The semi-axis b polar fixed ar 85 mm and the semi-axis a polar at 80 mm. 62

6.39 Mean effective area for ellipsoidal gel pads as a functions of the semi-axis b polar and semi-axis a polar with the range reduced. The semi-axis b equatorial and the semi-axis a equatorial fixed at their optimal values, 61 mm and 64 mm respectively. 63

6.40 Mean effective area for ellipsoidal reflectors as a functions of the semi-axis b equatorial and semi-axis a equatorial with the range reduced. The semi-axis b polar and the semi-axis a polar fixed at their optimal values, 135 mm and 54 mm respectively. 63

6.41 Effective area for the whole module with conical reflectors. Opening angle equatorial 30° and opening angle polar 30°. 64

6.42 Effective area for the whole module with conical gel pads. Opening angle equatorial 31° and opening angle polar 83°. 64

6.43 Effective area for the whole module with ellipsoidal reflectors. Semi-axis b equatorial 58 mm, semi-axis b polar 58 mm, semi-axis a equatorial 70 mm and semi-axis a polar 70 mm. 64

6.44 Effective area for the whole module with ellipsoidal gel pads. Semi-axis b equatorial 61 mm, semi-axis b polar 135 mm, semi-axis a equatorial 64 mm and semi-axis a polar 54 mm. 64

A.1 Necessary measurements to place the PMTs inside of the module. . . . 69

B.1 Integration over phi of the effective area with reflectors for several semi-axes minor, fixing the semi-axis a at 80 mm. 71

B.2 Integration over phi of the effective area with reflectors for several semi-axes minor, fixing the semi-axis a at 90 mm. 71

B.3 Integration over phi of the effective area with gel pads for several semi-axes minor fixing the semi-axis a at 80 mm. 72
B.4 Integration over phi of the effective area with gel pads for several semi-axes minor fixing the semi-axis a at 90 mm. 73

List of Tables

4.1 Particles and processes taken into account during all simulations. . . . 33
6.1 The best parameters possible for the conical reflectors/gel pads. 53
6.2 The optimal parameters for the ellipsoidal reflectors/gel pads. 62
7.1 Summary of the optimal parameters for each module and its respective mean effective area. 66
A.1 Position and orientation of the PMTs for the module LOM. 69

References

[1] K. Winter, “Neutrino physics,” *Neutrino Physics*, 2008.

[2] W. Pauli, “Pauli letter collection: letter to Lise Meitner.” Typed copy.

[3] S. Bilenky, “Neutrino. history of a unique particle,” *The European Physical Journal H*, vol. 38, no. 3, pp. 345–404, 2013.

[4] C. Cowan, F. Reines, F. Harrison, and H. Kruse, “Detection of the free neutrino: a confirmation,,” *Science*, vol. 124, no. 3212, pp. 103–104, 1956.

[5] MissMJ, Nasfarley88, et al. URL `https://commons.wikimedia.org/wiki/File:Standard_Model_of_Elementary_Particles_modified_version.svg`, 2014.

[6] M. U. Elorrieta, “Studies on dark rates induced by radioactive decays of the multi-pmt digital optical module for future icecube extensions.” URL `https://www.uni-muenster.de/imperia/md/content/physik_kp/agkappes/abschlussarbeiten/masterarbeiten/1712-ma_munland.pdf`, 2017.

[7] C. Spiering, “Towards high-energy neutrino astronomy,” in *From Ultra Rays to Astroparticles*, pp. 231–263, Springer, 2012.

[8] T. K. Gaisser, R. Engel, and E. Resconi, *Cosmic rays and particle physics*. Cambridge University Press, 2016.

[9] K. A. Olive, K. Agashe, C. Amsler, M. Antonelli, J.-F. Arguin, D. M. Asner, H. Baer, H. R. Band, R. Barnett, T. Basaglia, *et al.*, “Review of particle physics,” *Chinese physics C*, vol. 38, no. 9, p. 090001, 2014.

[10] F. Halzen, “Astroparticle physics with high energy neutrinos: from amanda to icecube,” *The European Physical Journal C-Particles and Fields*, vol. 46, no. 3, pp. 669–687, 2006.

[11] D. Semikoz, “Constraints on top-down models for the origin of uhecrs from the pierre auger observatory data,” *arXiv preprint arXiv:0706.2960*, 2007.

[12] Lacosmos. URL `https://commons.wikimedia.org/wiki/File:Gerbe.png`, 2007.

[13] P. D. Group, P. Zyla, R. Barnett, J. Beringer, O. Dahl, D. Dwyer, D. Groom, C.-J. Lin, K. Lugovsky, E. Pianori, *et al.*, “Review of particle physics,” *Progress of Theoretical and Experimental Physics*, vol. 2020, no. 8, p. 083C01, 2020.

[14] R. Engel, D. Seckel, and T. Stanev, "Neutrinos from propagation of ultrahigh energy protons," *Physical Review D*, vol. 64, no. 9, p. 093010, 2001.

[15] V. Berezinskii and G. Zatsepin, "Cosmic neutrinos of superhigh energy.," tech. rep., Lebedev Inst. of Physics, Moscow, 1970.

[16] C. Grupen, G. Cowan, S. Eidelman, and T. Stroh, *Astroparticle physics*, vol. 50. Springer, 2005.

[17] E. Fermi, "Galactic magnetic fields and the origin of cosmic radiation.," *The Astrophysical Journal*, vol. 119, p. 1, 1954.

[18] U. F. Katz and C. Spiering, "High-energy neutrino astrophysics: Status and perspectives," *Progress in Particle and Nuclear Physics*, vol. 67, no. 3, pp. 651–704, 2012.

[19] R. Gandhi, C. Quigg, M. H. Reno, and I. Sarcevic, "Neutrino interactions at ultrahigh energies," *Physical Review D*, vol. 58, no. 9, p. 093009, 1998.

[20] I. Belolaptikov, L. Bezrukov, B. Borisovets, N. Budnev, E. Bugaev, A. Chensky, I. Danilchenko, J.-A. Djilkibaev, V. Dobrynin, G. Domogatsky, *et al.*, "The baikal underwater neutrino telescope: Design, performance, and first results," *Astroparticle Physics*, vol. 7, no. 3, pp. 263–282, 1997.

[21] M. Ageron *et al.*, "ANTARES: the first undersea neutrino telescope," *Nucl. Instrum. Meth. A*, vol. 656, pp. 11–38, 2011.

[22] M. G. Aartsen, M. Ackermann, J. Adams, J. Aguilar, M. Ahlers, M. Ahrens, D. Altmann, K. Andeen, T. Anderson, I. Ansseau, *et al.*, "The icecube neutrino observatory: instrumentation and online systems," *Journal of Instrumentation*, vol. 12, no. 03, p. P03012, 2017.

[23] S. Adrián-Martínez, M. Ageron, F. Aharonian, S. Aiello, A. Albert, F. Ameli, E. Anassontzis, M. Andre, G. Androulakis, M. Anghinolfi, and et al., "Letter of intent for km3net 2.0," *Journal of Physics G: Nuclear and Particle Physics*, vol. 43, p. 084001, Jun 2016.

[24] J. Jelley, "Cerenkov radiation and its applications," *British Journal of Applied Physics*, vol. 6, no. 7, p. 227, 1955.

[25] M. G. Aartsen *et al.*, "Neutrino emission from the direction of the blazar TXS 0506+056 prior to the IceCube-170922A alert," *Science*, vol. 361, no. 6398, pp. 147–151, 2018.

[26] R. Abbasi, Y. Abdou, T. Abu-Zayyad, M. Ackermann, J. Adams, J. Aguilar, M. Ahlers, M. Allen, D. Altmann, K. Andeen, *et al.*, "The design and performance of icecube deepcore," *Astroparticle physics*, vol. 35, no. 10, pp. 615–624, 2012.

[27] R. Abbasi, Y. Abdou, M. Ackermann, J. Adams, J. Aguilar, M. Ahlers, D. Altmann, K. Andeen, J. Auffenberg, X. Bai, *et al.*, "Icetop: The surface component of icecube," *Nuclear Instruments and Methods in Physics Research Section A: Accelerators, Spectrometers, Detectors and Associated Equipment*, vol. 700, pp. 188–220, 2013.

[28] F. Halzen and S. R. Klein, "Invited review article: Icecube: an instrument for neutrino astronomy," *Review of Scientific Instruments*, vol. 81, no. 8, p. 081101, 2010.

[29] A. Ishihara, "The icecube upgrade–design and science goals," *arXiv preprint arXiv:1908.09441*, 2019.

[30] Y. Makino, "D-egg: A next-generation optical module for icecube," in *EPJ Web of Conferences*, vol. 207, p. 06005, EDP Sciences, 2019.

[31] L. Classen, *The mDOM – a multi-PMT digital optical module for the IceCube-Gen2 neutrino telescope.* PhD thesis, Erlangen - Nuremberg U., 2017.

[32] A. Kappes, "Multi-pmt optical module designs for icecube-gen2," in *EPJ Web of Conferences*, vol. 116, p. 01001, EDP Sciences, 2016.

[33] M. Aartsen, R. Abbasi, M. Ackermann, J. Adams, J. Aguilar, M. Ahlers, M. Ahrens, C. Alispach, P. Allison, N. Amin, *et al.*, "Icecube-gen2: The window to the extreme universe," *arXiv preprint arXiv:2008.04323*, 2020.

[34] R. Bruijn and D. van Eijk, "The km3net multi-pmt digital optical module," in *The 34th International Cosmic Ray Conference*, vol. 236, p. 1157, SISSA Medialab, 2016.

[35] S. Flyckt and C. Marmonier, "Photonis imaging sensors," *Photomultiplier tubes principles and applications*, 2002.

[36] T. Benson, J. Cherwinka, M. Duvernois, A. Elcheikh, F. Feyzi, L. Greenler, J. Haugen, A. Karle, M. Mulligan, and R. Paulos, "Icecube enhanced hot water drill functional description," *Annals of Glaciology*, vol. 55, no. 68, pp. 105–114, 2014.

[37] R. Winston, J. C. Miñano, P. G. Benitez, *et al.*, *Nonimaging optics.* Elsevier, 2005.

[38] “Geant4 web site.” URL `https://geant4.web.cern.ch/`, accessed December 2020.

[39] S. Agostinelli *et al.*, “GEANT4–a simulation toolkit,” *Nucl. Instrum. Meth. A*, vol. 506, pp. 250–303, 2003.

[40] B. Herold, “Simulation and measurement of optical background in the deep sea using a multi-pmt optical module,” 2017.

[41] “Nautilus marine service gmbh, vitrovex – glass instrumentation housings.” URL `https://www.vitrovex.com/instrumenthousings/`, accessed November 2020.

[42] “Shin-etsu chemical co..” URL `http://www.shinetsusilicone-global.com/index.shtml`, accessed November 2020.

[43] “Almeco s.p.a.” URL `https://www.almecogroup.com/en`, accessed November 2020.

[44] K. M. Gorski, E. Hivon, A. J. Banday, B. D. Wandelt, F. K. Hansen, M. Reinecke, and M. Bartelmann, “Healpix: A framework for high-resolution discretization and fast analysis of data distributed on the sphere,” *The Astrophysical Journal*, vol. 622, no. 2, p. 759, 2005.

Acknowledgments

– Agradecimientos –

First of all, I would like to express my deepest appreciation to my advisor Prof. Alexander Kappes for giving me the opportunity to research this exciting topic and the chance to be part of this amazing group. Your professional and personal support have been essential for getting my goals.

Also, this work would not have been possible without the assistance and the neverending patience of Dr. Lew Classen. I want to thank you for teaching me everything and answering all my (most of the time dumb) questions.

I would like to extend my sincere thanks to Dr. Carlos Guerrero who has kindly offered me his support despite the distance. I really appreciate that.

Many thanks to Markus Dittmer, Daniel Guderian, Berit Schlüter, Fynn Peters, Moritz Schlechtriem, Raffaela Busse and the others all members group who made me feel like part of this team since the beginning. They have always been there to lend me a hand when I need it. Special thanks to Cristian Lozano and Martin Unland for teaching me how everything works and for proofreading most of this thesis. You both have always had an open ear for me.

I also wish to give thanks to everybody I have met here in Münster, despite the pandemic situation we have managed to have a year full of fun. A part of me will stay here forever.

It is hard to finish this without mentioning my friends Fernando, Lucas, and Pablo. They took with me the first step to come to Germany and live this adventure. Now, I know that it has been one of the best experiences of my life. Thanks for all moments we lived together.

A ti, Ana, por estar siempre y apoyarme en todo lo que me propongo. Conoces todas mis caras y has estado ahí en todas y cada una de ellas, siempre que lo necesité. Nada de esto habría sido posible sin ti.

Por último, y no por eso menos importante si no más bien todo lo contrario, gracias a mis padres por su apoyo incondicional. Soy lo que soy por que vosotros me habéis dado los valores que hoy me definen. Siempre fuisteis los primeros en confiar en mi. Nunca podré devolveros tanto. Os quiero.

Un beso mirando al cielo. Se que estas orgulloso.